Development of Terahertz Antennas for 6G Wireless Communication

Muhammad Zubair

Submitted in fulfilment of the requirements for the
Degree of Doctor of Philosophy

School of Engineering
College of Science and Engineering
University of Glasgow

May 2024

Abstract

The world is rapidly advancing towards next-generation wireless communication systems. A significant advancement is a use of millimeter-wave (mmWave) technology in 5G, which addresses the spectrum shortage in current 4G cellular systems operating below 6 GHz. However, the increasing number of emerging applications such as virtual reality (VR), the Internet of Things (IoT), and autonomous vehicles, along with future applications yet to be conceived such as remote surgery, will require even greater data rates and lower latency than what 5G networks currently offer. Consequently, the development of sixth-generation (6G) wireless communication systems becomes crucial to meet these needs for higher bandwidth, increased data rates, ultra-low latency, enhanced throughput, and massive connectivity.

To overcome these challenges, the utilization of the terahertz (THz) band, which lies between the microwave and infrared regions of the electromagnetic spectrum, is being explored. The terahertz frequency range, spanning from 0.1 THz to 10 THz, is considered a viable solution for advancing next-generation wireless communication, THz imaging and sensing applications, as well as for future technologies beyond 5G and sixth-generation (6G). The THz spectrum offers a largely underutilized bandwidth with low spectral congestion. However, its effectiveness is hindered by significant path loss and high signal attenuation due to oxygen absorption, posing additional challenges in developing highly efficient wideband, high-gain, compact, and cost-effective antenna solutions with precise microfabrication techniques.

Traditional antenna design methods, which are based on analytical and numerical techniques, often face limitations in addressing the complexities associated with terahertz frequencies. These methods can be computationally intensive, time-consuming, and may not always yield optimal solutions, especially when dealing with complex geometries and non-conventional materials. This work investigates the feasibility of AI-driven antenna design techniques, specifically the Surrogate Model-assisted Differential Evolution for antenna synthesis (SADEA) series. In this series SADEA-I, and the latest installment of self-adaptive Bayesian neural networks surrogate-model-assisted differential evolution for antenna optimization (SB-SADEA), have been employed for the first time (to the best of our knowledge) to achieve optimal performance.

This thesis encompasses four high-performance THz antenna design solutions offering, aimed at next-generation THz wireless applications and 6G technologies. The first THz antenna de-

sign is a high-gain, compact, wide-bandwidth 4-element planar antenna array based on a hybrid corporate network. The array has dimensions of 1.82 $\lambda_0 \times 1.79\lambda_0 \times 0.044\ \lambda_0$, where λ_0 is the free space wavelength at 105 GHz. It offers a -10 dB impedance bandwidth across the entire 100-110 GHz range, a low side lobe level, total efficiency above 80%, and a peak measured gain of 13.90 dBi with less than 1 dBi gain variation across the whole band (100-110 GHz). This makes it an ideal candidate for radar systems, as a broad 1 dB gain bandwidth antenna can enhance target detection and tracking accuracy, thereby improving situational awareness in surveillance applications. Additionally, the wide frequency coverage provided by the 1 dB gain bandwidth antenna ensures versatility for a variety of applications requiring robust and reliable wireless communication capabilities.

The second antenna design uses a parasitic patch element approach in serial feed to create a compact, cost-effective, planar 5-element array with high gain. The design provides, and enhances co-polarized currents, resulting in an increase in gain from 13.15 dBi to 16.50 dBi and aperture efficiency from 9.18% to 20.47% with the same antenna aperture size. It achieves high directional beams towards the broadside over 10 GHz (100-110 GHz), with a radiation efficiency exceeding 92.4% and a peak realized gain of about 16.50 dBi, with minimal gain variation (less than 0.90 dB) across the entire band. This makes it a suitable candidate for THz wireless access communication scenarios that require large bandwidth and multi-gigabit data rate, such as high-definition video signal transfer. An antenna with a broad 1 dB gain bandwidth can find various applications across different sectors. Notably, it could be particularly effective in THz indoor wireless communication systems where reliable and high-speed data transmission is crucial.

The third and fourth proposed solutions involve a novel THz structure featuring a 64-element array with a hybrid corporate-series feed network, fabricated using advanced microfabrication techniques such as electron beam lithography (E-beam). The integration of microfabricated THz antenna arrays with coplanar waveguide (CPW) feed techniques significantly enhances antenna performance, improving bandwidth, gain, efficiency, and ease of fabrication. This design offers ultra-wideband (UWB) performance with a -10 dB impedance bandwidth across the entire frequency range from 0.75 to 1.1 THz. The proposed arrays exhibit a peak gain of 15.05 dBi, consistent over the entire operating frequency range with a gain variation of less than 1.5 dB. Additionally, the antenna achieves a peak total efficiency of 87.78%. The high performance of these microfabricated THz antenna arrays makes them suitable for various applications, such as THz communication systems, imaging, and spectroscopy. The use of CPW feed techniques also allows for easy integration with other components in THz systems, further enhancing their versatility and practicality.

The primary goal of this study is to design, fabricate and measure novel THz antennas using AI-driven design techniques for 6G wireless communications. By successfully designing, fabricating, and measuring various novel THz antennas with different materials, this research paves the way for future short-range THz wireless communication.

List of Publications

Journals and Conferences

M. Zubair, A. Jabbar, F. A. Tahir, M. A. Imran, B. Liu, and Q. H. Abbasi, **"A High-Performance Sub-THz Planar Antenna Array for THz Sensing and Imaging Applications,"** *Published (Scientific Reports) 2024*.

M. Zubair, A. Jabbar, M. O. Akinsolu, M. A. Imran, B. Liu, and Q. H. Abbasi, **"Design of truncated microstrip square patch antenna for terahertz communication,"** *2022 IEEE International Symposium on Antennas and Propagation and USNC-URSI Radio Science Meeting (AP-S/URSI)*, pp. 1558–1559, 2022.

M. Zubair, M. O. Akinsolu, A. Abohmra, M. A. Imran, B. Liu, Q. H. Abbasi, **"Terahertz Antenna Design Using Machine Learning Assisted Global Optimization Techniques,"** *2023 IEEE International Symposium on Antennas and Propagation and USNC-URSI Radio Science Meeting (USNC-URSI)*, pp. 1007–1008, 2023.

M. Zubair, A. Jabbar, F. A. Tahir, M. Ur-Rehman, M. A. Imran, B. Liu, and Q. H. Abbasi, **"Design of Efficient and High Gain Sub-THz Series-Fed Antenna Array for THz Communication,"** *2024 IEEE International Symposium on Antennas and Propagation and USNC-URSI Radio Science Meeting (USNC-URSI)*, 2023

M. Zubair, M. O. Abohmra, F. A. Tahir, M. A. Imran, B. Liu, and Q. H. Abbasi, **"Design of Micro-fabricated THz Triangular Slot Patch Antenna for Short-Range Wireless Communication,"** *Submitted (Scientific Reports)*, 2024.

M. Zubair, Chan H. See,, M. O. Akinsolu, F. A. Tahir, M. A. Imran, Q. H. Abbasi, and B. Liu, **"Design Methodologies for THz Antennas: A Comparative Analysis Using Machine Learning-Assisted Optimization for 6G Communication,"** *Submitted to be (IEEE AWPL)*, 2024.

List of Acronyms

6G 6th Generation

THz Terahertz

SEM Scanning electron microscope

mm-Wave Millimeter wave

IoT Internet of Things.

S-parameters Scattering Parameters.

SADEA Surrogate Model-assisted Differential Evolution for antenna synthesis

SB-SADEA Self-adaptive Bayesian neural networks surrogate-model-assisted differential evolution for antenna optimization

CPW Coplanar waveguide

UWB Ultra-Wide Band

GSG Ground-Signal-Ground

PMMA Polymethyl Methacrylate

CDL Charge Dissipation Layer

EBL Electron beam lithography

PEC perfect electric conductor

VNA Vector Network Analyser

GA Genetic Algorithm

GP Gaussian Process

MIMO Multiple-input multiple-output

MEMS	Micro-electromechanical systems
TRF	Trust Region Framework
PCB	Printed Circuit Board
OFDM	Orthogonal frequency division multiplexing
PSADEA	Parallel Surrogate Model-assisted Hybrid Differential Evolution for Antenna Optimisation
PSO	Particle Swarm Optimisation
SAEA	Surrogate Model-Assisted Evolutionary Algorithm
PEC	Perfect electrical conductor
PIN	Positive-intrinsic-negative
PSO	Particle swarm optimisation
HPBW	Half-power beamwidth
mGbp	multi-gigabit per second
SLL	Side-lobe level

Contents

List of Tables

List of Figures

Acknowledgments

First and foremost, I would like to express my profound gratitude to my supervisor, Professor Qammer H. Abbasi, for the invaluable opportunity to work in this exhilarating field. His mentorship, motivational support, and the intellectual freedom he granted have been pivotal to my research journey.

I am also indebted to my co-supervisor, Professor. Bo Liu, for his guidance and steadfast support during my initial years, which were crucial in shaping the path of my studies. Additionally, I owe a great deal of thanks to my other co-supervisor, Professor Muhammad Ali Imran, for his expert technical advice and continued encouragement.

My experience at the CSI lab was greatly enhanced by the group's vibrant community. I am sincerely thankful for the unforgettable memories, dinners, parties, and trips we shared, which provided much-needed relaxation and camaraderie.

Special thanks go to the staff of the James Watt Nanofabrication Centre (JWNC), whose assistance was essential for the success of my research. Without their support, the accomplishments documented in this report would not have been possible.

Most importantly, I am forever grateful to my family for their unending love and support. To my parents, who have nurtured me with love and encouragement from the moment I was born, and to my wife, whose patience and understanding were my pillars during the challenging times of my PhD studies.

I am truly grateful to each individual who has been a part of this journey, for your roles have been essential in bringing this chapter of my life to a fruitful conclusion.

Declaration

With the exception of chapters 1 and 2 which contain introductory material, all work in this thesis was carried out by the author unless otherwise explicitly stated.

Chapter 1

Introduction

1.1 Background and Motivation

The exponential growth in data demand, alongside expectations for instant connectivity and the Internet of Things (IoT), has driven the development of next-generation wireless communications systems, notably sixth-generation (6G). Unlike its predecessor, 6G aspire to integrate higher frequencies, specifically the terahertz (THz) band, to surpass the limitations of current technologies in bandwidth and reduce latency significantly. To push for higher data rates, lower latency, and massive connectivity drives the ongoing development of 6G wireless communication technology [13]. 6G is expected to provide data rates of up to 1 terabit per second (Tbps), latency as low as 100 microseconds, and support for up to 10 million devices per square kilometre. Meeting these requirements with current technologies, such as 4G and 5G, is challenging due to the limited available bandwidth and the limitations of the frequency bands used. To overcome these challenges, 6G technology is expected to leverage higher frequency bands, such as the terahertz band, which offers much higher bandwidth and can potentially enable the required performance.

1.1.1 Potential of Terahertz Technology for 6G

The terahertz frequency band is between the millimetre wave and the infrared band in the electromagnetic spectrum, including an extremely wide frequency range from 0.1 to 10 THz as shown in Figure 1.1, and the corresponding wavelength is 30μm to 1mm [14]. The low-frequency part of the THz wave intersects the millimeter wave and the high-frequency part intersects the infrared wave, making THz technology a cutting-edge technology in electronics and photonics.

This band is increasingly appealing for advanced communication technologies due to its largely untapped potential and its vast bandwidth, which are critical for the next generation of wireless communications [15]. The THz band has several substantial advantages for 6G wireless communications. It offers a much higher bandwidth compared to lower frequency bands,

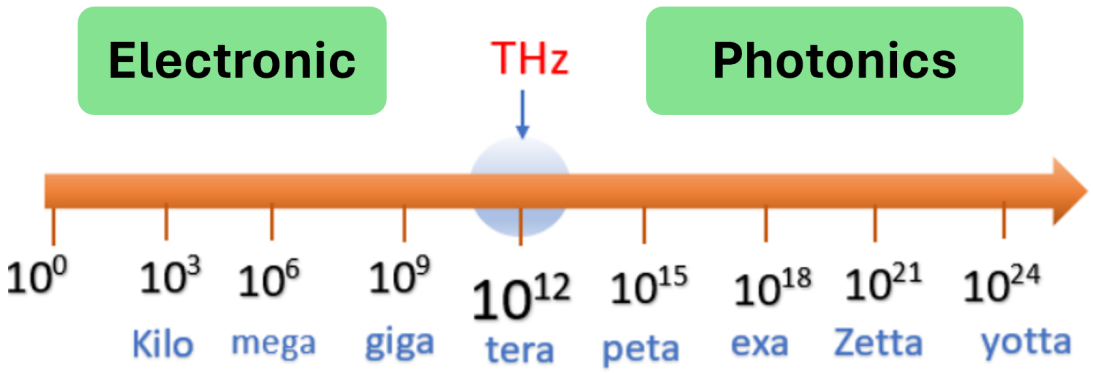

Figure 1.1: Electromagnetic Spectrum with the THz frequency band positioned between radio and infrared spectrums.

which is essential for supporting higher data rates and accommodating more users simultaneously. Additionally, the shorter wavelength associated with THz frequencies can facilitate the development of more compact communication devices, potentially reducing transmission delay and achieving lower latency in network communications. Furthermore, the capability of THz waves to penetrate various non-conductive materials like clothing and paper makes it ideal for high-precision sensing and imaging applications, useful in industrial and security contexts.

1.1.2 Application and Challenges of THz Frequencies

THz frequencies have potential applications across a wide range of scientific domains, including medical diagnosis and security imaging. In medical settings, THz technology could revolutionize noninvasive imaging techniques and cancer detection by providing high-resolution images of tissue and identifying abnormalities without the risks of ionizing radiation. In security, the ability of THz waves to penetrate clothing can be used for the non-invasive detection of concealed weapons and other threats.

Despite its potential, THz communication encounters significant challenges. Propagation losses in the THz band are considerably high due to atmospheric absorption and scattering, limiting the range of communication links. Furthermore, developing THz-compatible hardware components, such as transceivers and antennas, presents considerable technical hurdles.

1.1.3 Role of Antennas in THz Communication Systems

Antennas are the key enabling components for realizing terahertz (THz) communication systems, playing a crucial role in a crucial role in the transmission and reception of electromagnetic waves. Their design is paramount for achieving optimal performance in terms of gain, directivity, and radiation patterns. However, designing antennas for the terahertz frequency range presents significant challenges. At these high frequencies, the behaviour of electromagnetic

waves and the properties of materials deviate significantly from those observed at lower frequencies. This deviation necessitates a revaluation of conventional design paradigms.

Moreover, the required miniaturization of antenna structures, along with the need for precise and advanced fabrication techniques, further complicates the design process. Traditional antenna design methods—primarily analytical and numerical techniques—are often not sufficient to address the complexities inherent in terahertz frequencies. These methods can be computationally intensive and time-consuming, and they may not always provide optimal solutions, especially when dealing with complex geometries or unconventional materials. Therefore, the development of new design strategies and tools that can efficiently handle these high-frequency challenges is critical for the advancement of THz communication technologies. The use of advanced design techniques, such as artificial intelligence (AI) driven optimization, can help overcome these challenges and develop efficient and high-performance THz antennas.

1.2 Problem Statement

Despite the promising capabilities of Terahertz (THz) frequencies to revolutionize 6G wireless communications by providing unprecedented data rates and connectivity, the practical application of this technology in antenna design is severely hindered by significant propagation losses and the absence of effective design methodologies suitable for such high-frequency ranges. Additionally, the requirements for antennas to not only overcome these losses, but also to integrate features such as high gain, ultra-wideband/multiband functionality, compact size, and conformal designs significantly add complexity to the design process. This research aims to address the critical gap in developing efficient high-gain THz antenna designs that are capable of overcoming these propagation challenges while meeting advanced specifications for functionality and form factor. The ultimate goal is to produce cost-effective, easy-to-fabricate, and high-performance THz antennas that fully harness the potential of THz technology in 6G wireless systems.

1.3 Aims and Objectives

The primary aims and objectives of this thesis are as follows.

- **Investigation of THz wireless communication frameworks:**To explore the current state and potential of THz frequency bands for use in next-generation wireless communication systems. This includes identifying suitable frequency bands and understanding the specific requirements for developing high-performance antennas that operate efficiently within these bands.

- **Identification of use cases for THz wireless communication:** Propose tailored THz antenna design solutions that address the specific requirements and challenges of applications such as high data rate communications, ultra-low latency connections, and enhanced connectivity in next-generation wireless systems.

- **Exploration of THz antenna designs and challenges:** Develop low-cost, compact, and reproducible antenna solutions within the THz band for high data rate applications. Design high-gain, wideband, and fixed-beam antenna arrays that can be seamlessly integrated with THz equipment. Focus on achieving broad bandwidth, high efficiency, and low side lobe levels to meet the demands of next-generation wireless communication systems.

- **Application of AI-driven design techniques:** Investigate the feasibility and effectiveness of AI-driven antenna design techniques, specifically focusing on the Surrogate Model-assisted Differential Evolution for Antenna Synthesis (SADEA) series, including SADEA-I and SB-SADEA. Following the design optimization, fabricate the antennas using advanced microfabrication techniques, such as electron beam lithography (e-beam), to ensure precise feature definition and alignment. Finally, evaluate the performance metrics of the fabricated antennas to assess their effectiveness.

1.4 Thesis Organisation

The rest of this thesis is organized as follows.

Chapter 2 presents the literature review of THz antenna design configurations. This chapter reviews material selection challenges, fabrication techniques, and the necessity for high gain and efficiency due to signal path loss at THz frequencies. In addition, advanced AI-driven antenna design techniques are explored, highlighting recent developments and applications in THz antenna design.

Chapter 3 describes the design, analysis, and performance of a single wideband element antenna with quasi-cross slots, and subsequently designed a hybrid 4-element planar THz feed antenna array. The antenna array performance in terms of bandwidth, gain, sidelobes, and beamwidth is presented in detail. Prototype fabrication and complete THz antenna measurements are elucidated. Moreover, it also explores the feasibility of using machine learning-assisted global optimization techniques to enhance antenna performance.

Chapter 4 presents the design, analysis, and performance of the series-fed fixed beam 5-element wideband THz antenna array. To further enhance performance, co-polarized parasitic elements are implemented within the existing array. The performance of the antenna array in terms of bandwidth, gain, sidelobes, and fixed broad-side beam over a wide bandwidth is presented in detail. Additionally, the use of AI-driven design techniques to improve antenna performance is discussed. The prototype fabrication and antenna measurements are also demonstrated.

Chapter 5 comprehensively documents the design, optimization, and fabrication of ultrawideband THz flexible antenna arrays, specifically developed for THz wireless communication. Covers the entire design process of the antenna unit element and the array configuration, utilizing the latest version of the SADEA-I series SB-SADEA optimization techniques to expedite the THz antenna design process and compare it with existing optimizers. The fabrication methods, particularly electron beam lithography, have been extensively discussed, alongside the performance metrics achieved, establishing the novelty and effectiveness of the proposed design.

Chapter 6 concludes the thesis and discusses the implications for THz antennas in 6G communications. It outlines potential areas for future research, suggesting ways to further enhance the design and efficiency of THz antennas to meet the demands of next-generation wireless communication technologies.

Chapter 2

Background and Literature Review

This chapter explores THz antennas within the context of 6G wireless communications, detailing their evolution, design, and the integration of Artificial Intelligence (AI). Starting with a historical overview from 1G to the transformative 6G, it highlights the shift to THz technology, addressing both its potential and challenges. The text examines various THz antenna designs, from traditional models to advanced materials like graphene, and discusses significant advancements in the field. In addition, it outlines the role of AI in optimizing the design of THz antennas to meet the performance specification of future THz wireless communication.

2.1 Evolution of Wireless Communication Technologies

The development of wireless communication technology is characterized by periodic revolutionary changes, reshaping the global connectivity landscape. It began with the advent of the first generation (1G) in the 1980s, which introduced analogue voice communications. Since then, each subsequent generation has brought significant advancements, increasing capabilities along the way.

2.1.1 From 1G to 4G

- **1G (First Generation):** Introduced in the 1980s, 1G networks were analogue, offering voice calls with limited clarity and security [**?**].
- **2G (Second Generation):** Emerging in the early 1990s, 2G networks shifted to digital technology, introducing basic data transmission services such as Short Message Service(SMS), Multimedia Messaging Service(MMS), and General Packet Radio Service(GPRS) [16].
- **3G (Third Generation):** Emerged in the early 2000s, 3G networks significantly increased data speeds, facilitating better internet access, video calling, and mobile internet services

[17].

- **4G (Fourth Generation):** Introduced in the late 2000s, 4G networks significantly improved data speeds and quality, enabling features such as high-definition mobile TV, video conferencing, and high-speed gaming, as well as faster download and upload speeds [18].

2.1.2 The Advent of 5G

Fifth-generation (5G) technology began to be deployed in 2019 and represents a major leap forward from 4G in terms of data speeds, reduced latency and greater flexibility. 5G networks are designed to support massive increases in bandwidth and utility, handle extensive networks of internet of thing (IoT) devices, and provide the backbone for technologies such as smart cities, autonomous driving, and advanced augmented reality applications [**?**] as shown in Figure 2.1.

2.1.3 Transitioning to 6G

As the conceptual and developmental phases of 6G commence, this next generation marks a transformative era in digital connectivity, set to substantially enhance the capabilities established by its predecessor, 5G. This new generation aims to achieve a revolutionary leap in network performance, characterized by extremely high data rates, virtually zero latency, and massive network capacities. The vision for 6G is not just evolutionary but revolutionary, aiming to integrate deeply with emerging technologies such as the Internet of Things IoT, AI, and smart cities, thus reshaping the landscape of digital communication and connectivity [**?**] [19]. Moreover, further detailed comparisons with other technologies are shown in Table 2.1 [20]–[25].

The development of THz antennas is essential to realize the ambitious goals of 6G. THz frequencies are key to achieving the extremely high data rates and low latency required by 6G, especially in dense urban environments. As we transition to these ultra-high frequencies (UHF), new challenges and opportunities in antenna design emerge. These include miniaturization, efficient beamforming, and overcoming propagation losses. Addressing these challenges is critical to ensuring the successful deployment of 6G wireless communication systems.

2.2 THz Technology in Wireless Communications

The exploration of THz frequencies for next-generation wireless communications is one of the most promising advances. THz frequencies, which lie between the microwave and infrared bands of the electromagnetic spectrum, are crucial to the realization of 6G objectives. These frequencies, particularly ranging from 0.1 THz to 10 THz with wavelengths from 0.03mm to 3mm, offer a vast, underutilized bandwidth capable of supporting ultra-high data transfer rates,

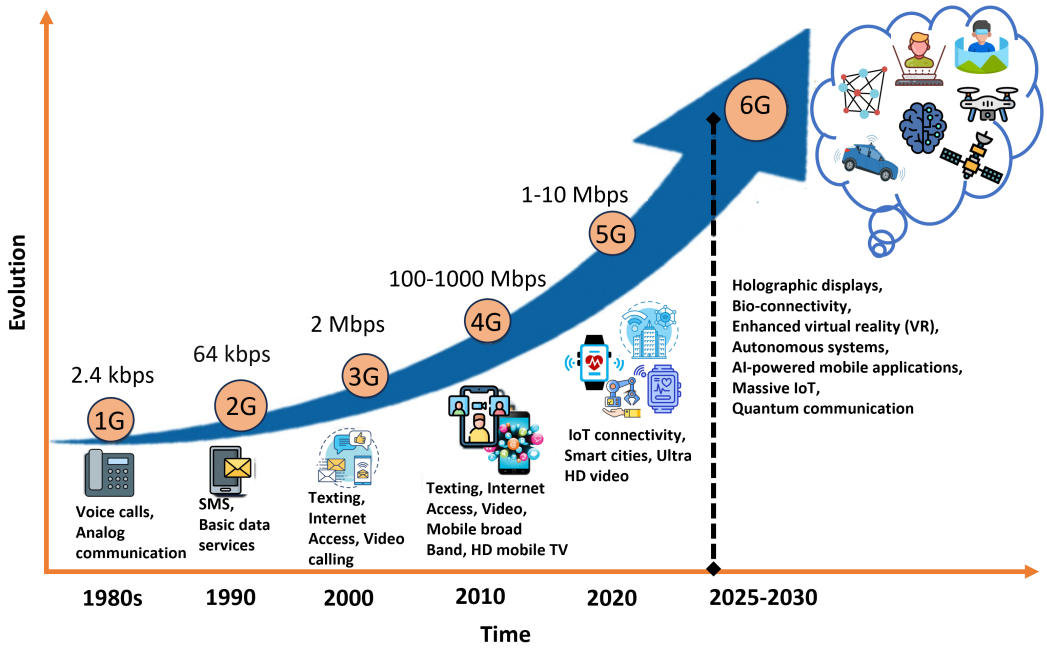

Figure 2.1: The Evolution of Wireless Networks Towards 6G Wireless Communications [1].

from 10 to 160 Gbps [26]. The transmission range of 10 meters is several orders of magnitude greater than current capabilities [**?**] [26].

The choice of the 0.1 THz to 10 THz frequency band is driven by several factors. This frequency range is relatively untapped, providing a wide bandwidth that can support significant improvements in data throughput compared to current communication technologies. The physical properties of these frequencies enable them to support ultra-high data transfer rates and ultralow latency, which are essential for meeting the high-speed demands of 6G. The wide bandwidth available in the THz range allows for substantial increases in data rates, which are crucial for applications requiring ultra-high-speed communication and low latency [19]. Additionally, the ability of THz waves to penetrate materials and provide high-resolution imaging makes them suitable for various advanced applications beyond traditional communication, such as sensing and imaging.

2.2.1 Characteristics of THz Frequency

- **Spectral position and energy:** THz waves harness higher energy than microwaves yet lower than infrared, making them suitable for applications that require moderate energy levels which do not cause ionizing effects, thus ensuring safety in various applications, including communication and imaging.

- **Wavelength characteristics:** The wavelength of THz radiation varies between 30 mi-

Table 2.1: Comparison with other technologies

Parameters	**4G**	**5G**	**6G**
Frequency range	2-8 GHz	3-300 GHz	0.3-3 THz
Max Data Rate	Up to 1 Gbps	Up to 20 Gbps	$\geq$ 1 Tbps
Bandwidth	100 MHz	30 GHz to 300 GHz	
Network capacity	Moderate	High	Very high
Energy Efficiency	Moderate	High Improved through more efficient hardware network	Ultra-high (10-100 times)
Key technologies	LTE LTE-advanced	Massive MIMO Network Slicing Beamforming	AI integration Advanced beamforming, Holographic Radio
Application	Mobile broadband HD video streaming	IoT Smart Cities Ultra-HD and 3D video	Immersive AR/VR Autonomous vehicles Remote surgery
Transmission Range	Several Kilometers	100-500 meters	100 meters to 1 kilometer
Latency	10 ms (millisecond)	Less than 2 ms	expected to be around 10-100 μs
Technologies	OFDM MIMO Turbo Code D2D communication	mm-wave communication massive MIMO Flexible frame structure Cloud/Edge computing	THz-Communication Quantum Communication and Computing AI/Machine learning Laser and VLC
Application	High-Definition Videos Voice Communication Mobile Television Mobile Internet Access Mobile Payment	Ultra High-Definition (UHD) Videos Vehicle-to-Everything (V2X) Communication Internet of Things (IoT) Smart City Wearable Devices	Holographic Verticals and Society Full-Sensory Digital Sensing and Reality Fully Automated Driving Industrial Internet Deep-Sea Sightseeing Internet of Bio-Nano-Things

crons and 3 millimetres. This property enables the development of compact antenna systems that are small enough to be integrated into portable devices while still maintaining significant coverage, suitable for personal device communications and intra-device communications within integrated circuits.

- **Propagation and Attenuation:** THz waves exhibit unique propagation characteristics, including high atmospheric absorption and limited diffraction through obstacles. This

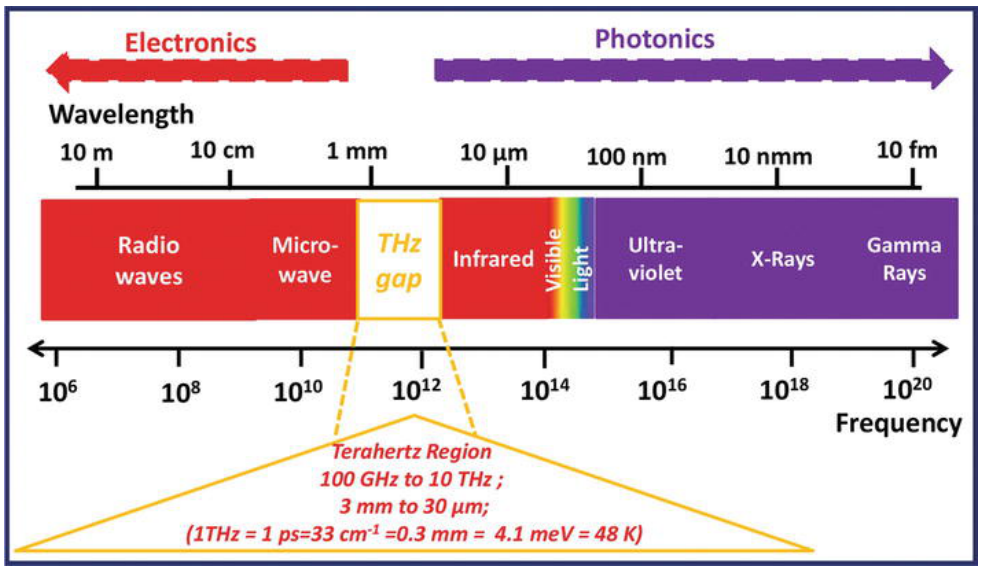

Figure 2.2: The THz frequency band of the electromagnetic spectrum[3].

high attenuation can be viewed as a double-edged sword. Although it limits the range of THz communications, it simultaneously reduces the risk of interference between devices nearby, promoting highly secure and densely deployed communication scenarios.

- **Transmission Clarity:** Despite its high absorption rate, THz frequencies have clear advantages in environments where precision and minimal interference are required. This frequency is capable of carrying high bandwidth without the latency issues associated with lower frequencies, making it ideal for applications that require fast data transfer over short distances.

- **Low damage:** The energy of a single photon in a THz wave is about one millionth that of an X-ray. Therefore, the use of THz waves for biomedical body scanning, specifically to detect skin cancer, could aid treatment without harming the organism [27].

- **Visualisation:** THz waves can penetrate certain non-metallic or non-polar materials due to their short wavelength. These waves can scan objects that are opaque to visible light, allowing for the production of higher-definition images. This property makes THz waves particularly useful in a variety of imaging applications.

- **High bandwidth:** THz frequencies provide exceptionally high bandwidth, which can support data transmission rates several orders of magnitude greater than those currently achievable with 5G. This massive bandwidth is crucial for supporting the growing data demands of modern applications such as immersive augmented and virtual reality, ultra-high definition streaming, and complex IoT ecosystems.

2.3 Applications of THz Frequency

The distinct properties of THz frequencies enable a broad range of applications across multiple sectors, particularly in enhancing 6G wireless communication technologies:

- **High-speed wireless communications:** One of the most promising applications of THz technology lies in its ability to facilitate ultra-high-speed wireless communications. With the emergence of technologies such as the IoT, augmented reality and connected smart devices, there is a growing need for higher data transmission rates, and THz frequencies offer a viable solution. It is particularly suitable for short-range, high-data-rate applications because of its high bandwidth and fast attenuation, which reduces long-range interference [28].

- **Network Densification:** The properties of THz waves make them ideal for network densification, a key strategy for enhancing network capacity in urban areas. Because THz signals have limited propagation and are significantly attenuated when passing through obstacles, they are well-suited for small, dense cells in urban environments. This setup can efficiently handle increased data traffic and user density without the interference issues typically faced by more penetrating waves [29].

- **Secure Communications:** Because THz waves have a limited range and are difficult to intercept without being in a direct transmission path, THz waves provide a higher level of security than lower frequencies. This makes THz-based systems particularly attractive for sensitive communications, including military and government uses where security is critical.

- **Imaging and Sensing:** In addition to telecommunications, THz technology is also making significant progress in imaging and sensing applications. In security inspections, THz waves can detect weapons or other dangerous objects under clothing without the health risks associated with ionizing radiation such as X-rays. Additionally, THz imaging is being explored for its potential in medical diagnostics, where it could provide new non-invasive methods for imaging cancer or monitoring wound healing [30].

- **Spectroscopy and materials characterization:** The ability of THz waves to interact with molecular vibrations makes them suitable for spectroscopic applications in chemistry and biology. This feature is used to analyze the composition of materials, detect impurities, and even observe biochemical processes. For example, in the pharmaceutical field, THz spectroscopy can help ensure drug quality by detecting coating thickness and uniformity [31].

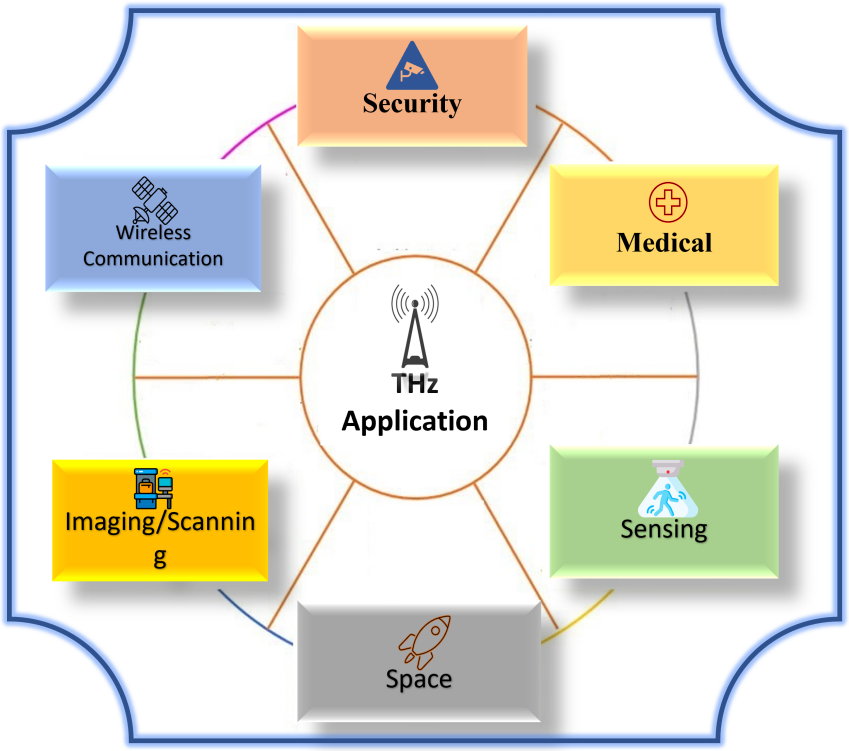

Figure 2.3: Various applications of THz radiation.

2.3.1 Challenges with THz Technology

- **Atmospheric Absorption:**

  This attenuation arises from a meteorological phenomenon called atmospheric absorption, which is the primary factor affecting transmitting signals. The frequency below 1 THz is particularly attractive for wireless communications because, above this threshold, attenuation becomes severe, significantly limiting the communication propagation distance. When the wavelength of THz waves approaches the size of oxygen and water vapour molecules present in the atmosphere, resonance occurs at a specific carrier frequency, resulting in an obvious attenuation peak, which significantly reduces signal quality. Figure 2. illustrates the atmospheric attenuation in (dB/km) depending on the frequency in (GHz). The peak attenuation measured at frequencies 183 GHz, 325 GHz, 380 GHz and 450 GHz is approximately 28 dB/km, 39 dB/km, approximately 400 dB/km and approximately 500 dB/km respectively. Therefore, it is necessary to operate in frequency bands below 1000 GHz, where attenuation is less than 100 dB/km. Consequently, the frequency windows are estimated as follows: 100–117 GHz, 123–175 GHz, 190–320 GHz, 335–376 GHz, 385–443 GHz, 453–515 GHz, 627–711 GHz, and 808–902 GHz [**?**] [32] and can be shown in Figure 2.4

- **Material Penetration:** In general, THz waves can penetrate a few millimetres into non-polar, low-moisture materials such as plastics, ceramics, and textiles [**?**]. For instance,

they can penetrate up to a few millimeters in materials like plastics and ceramics. However, their penetration depth is significantly limited in polar or moisture-containing materials due to strong absorption by water molecules. In biological tissues, THz waves typically penetrate between 0.1 to 0.5 mm [33]. This limited penetration in moisture-rich environments poses challenges for outdoor communications using THz waves, especially in humid or rainy conditions. The absorption by water vapor in the atmosphere further restricts the effective transmission range, making it less suitable for certain outdoor applications [34].

- **Device technology:** Developing devices operating at THz frequencies involves complex and expensive fabrication techniques, often requiring advanced materials and precise engineering.

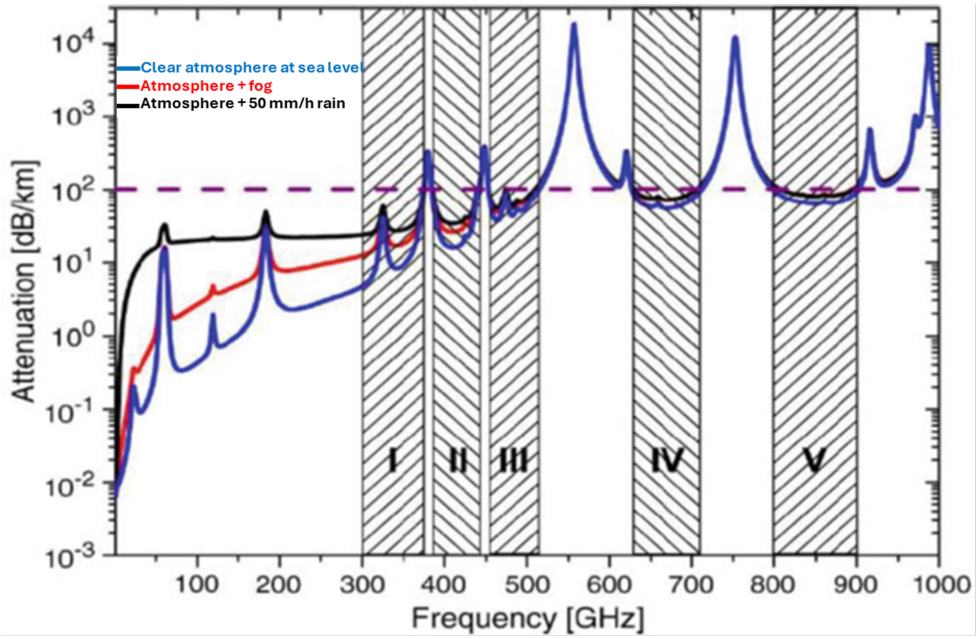

Figure 2.4: THz band attenuation due to atmospheric absorption [2].

2.4 THz Antenna Design

The increasing demand for spectrum resources requires the exploration of higher frequency bands for antenna operation. THz antennas can use the vast bandwidth of the THz spectrum, significantly outperforming conventional antennas by providing more bandwidth. They combine the benefits of millimetre waves (mm-Waves) and light waves, offering a wider usable frequency band, stronger beam directional and enhanced security and interference resistance compared to millimetre waves. In contrast to light waves, THz waves are more efficient and the penetration is stronger [24]. The primary advantage of THz antennas is their wide operating bandwidth, which

is crucial for the performance of THz wireless communication systems in radiating and detecting THz waves. The effectiveness of these antennas affects the overall quality of the communication system, especially in terms of bandwidth and gain. Furthermore, the characteristics of the THz antenna are vital for determining the data transmission rate, imaging resolution, and operational range of detection systems. THz antennas have a wide range of advantages, including wide bandwidth, high resolution, strong directivity, and potential for miniaturization.

2.4.1 Principle of THz Antenna Design

- **Size and Scaling:** Because of the high frequency of a THz antenna, are significantly smaller than those used in lower frequency bands. This allows integration into compact devices but also poses challenges to manufacturing precision and integration with other electronic components.
- **Materials Selection:** The performance of THz antennas is highly dependent on the materials used, as the skin depth is much smaller and the material properties affect the radiation efficiency.
- **Bandwidth and Efficiency:** : Compared to microwave antennas, THz antennas typically exhibit narrower bandwidths and lower radiation efficiency. Enhancing these aspects involves innovative design approaches, such as the use of metamaterials or multi-resonant structures.
- **Integration and Packaging:** THz antennas must be designed for integration into devices and systems, considering factors such as form factor, mounting options, and compatibility with other components.
- **Performance Optimization:** Use techniques such as simulation, modelling, and optimization algorithms, including those based on AI, to fine-tune THz antenna designs to achieve optimal performance metrics such as gain, bandwidth, and radiation pattern.

2.4.2 Development of THz Antenna

The development of THz antennas marks a major advancement in wireless communication technology. THz's research originated from research in the 19th century and gained particular attention at the end of the 20th century. Practical applications of THz waves emerged in the 1980s, paving the way for the development of THz communications standards in 2017. Significant contributions to THz communication systems have been made globally, with Japan's Nippon Telegraph and Telephone Corporation (NTT) leading the field in THz communications, achieving transmission rates up to 100 Gbps, which highlighted the potential of THz frequencies for ultra-high-speed data transfer.

2.4.3 Significant Milestones in THz Antenna Design

1. **Planar Antenna:** Planar Antennas: In the late 1990s and early 2000s, planar antennas such as microstrip patch antennas and slot antennas were used in THz applications [**?**]. These antennas are relatively easy to fabricate and integrate with other planar circuit technologies, making them a popular choice for early THz systems.

2. **Plasmonic Antennas:** The concept of plasmonic antennas was introduced in the early 2000s, which utilizes surface plasmon resonance to achieve efficient radiation at THz frequencies. Plasmonic materials, such as certain metals and graphene, offer a way to overcome some of the propagation challenges associated with THz waves [35].

3. **Metamaterial-Based Antennas:** The development of metamaterials—artificial structures with engineered electromagnetic properties—represents a key leap forward. Metamaterial-based antennas can be designed to exhibit unique properties, such as negative refractive index and enhanced directivity, which are beneficial for THz communications [36].

4. **Graphene-based Antenna:** Graphene, a two-dimensional material with excellent electrical and mechanical properties, is a promising THz antenna material. Graphene-based antennas have tunable frequency response, high efficiency and flexibility, making them suitable for a variety of THz applications [37].

5. **3D Printed Antennas:** Recent advances in 3D printing technology enable the fabrication of complex antenna geometries that were previously unachievable. 3D printing enables rapid prototyping and customization of THz antennas, which is critical for experimental and low-volume production scenarios [38].

Despite this, THz antenna design still faces considerable challenges, including high propagation losses, atmospheric absorption, and the need for high-precision fabrication techniques. As discussed in Section 2.3, overcoming these challenges is critical for the widespread adoption of THz technology in wireless communications.

2.4.4 Types of THz Antenna Design

THz antennas are designed in diverse configurations and sizes, encompassing an array of designs such as angle array reflectors, on-chip antennas, pyramidal cavities within dipoles, dielectric lens planar antennas, microstrip planar antennas, bowtie dipoles, photoconductive antennas, THz horn antennas, and graphene-based antennas [39]. Furthermore, THz antennas can be roughly categorized based on their manufacturing material into three categories: metallic antennas, primarily represented by horn antennas; dielectric antennas, predominantly based on lens antennas; and antennas utilizing new materials such as graphene or carbon nanotubes (CNTs) [6].

- **Horn Antenna**

  Among these, the horn antenna is a common metallic antenna designed for use in the THz frequency band. Several types of horn antennas exist, including E-plane horn antennas, H-plane horn antennas, circular/conical horn antennas, and corrugated and pyramidal horn antennas as shown in Figure 2.6(a) and b. Typically, conical horns are used as antennas for classic millimeter-wave receivers. Corrugated and dual-mode horn antennas offer several advantages, including rotationally symmetric radiation patterns, high gain of 20 to 30 dBi, low cross-polarization levels of approximately -30 dB, and 97%-98% efficiency. These antennas typically provide approximately 30%-40% and 6%-8% bandwidth respectively [40]. However, due to the extremely high frequency of THz waves, the size of horn antennas is inherently small, posing challenges, especially in the design of antenna arrays. This complexity results in high costs and limited production capacity [41]. Moreover, silicon-based on-chip antennas experience high radiation losses and low gain due to the high permittivity and low resistivity of the silicon substrate [42].

- **Dielectric Lens Antennas**

  Dielectric lens antennas are considered quasi-optical systems in which the traditional waveguide horn is replaced by a planar printed antenna on a wide dielectric substrate alongside a silicon lens as shown in Figure 2.6(h). This lens material is used to delay travelling waves, converting them from a spherical wavefront to a planar wavefront. Compared to waveguide horn antennas, dielectric resonator antennas, known for their compact size and high radiation efficiency have the advantage of a simple process, easy integration and cost-effective micro-machining techniques. However, as dielectric resonator antennas incorporate a dielectric substrate, they encounter challenges associated with the surface wave effect (also known as thick medium mode) particularly as frequencies approach the THz band. This phenomenon encounters difficulties in achieving wide bandwidth and robust mechanical designs [43] [44].

- **Photoconductive Antennas**

  Typical photoconductive antennas exhibit various geometries, including dipole antennas and large aperture antennas. some of the examples include the bow-tie photoconductive antenna, a variant of the dipole antenna, and the logarithmic-helical antenna, commonly used for integrating large aperture antennas as shown in Figure 2.6(d),(f) and (h). As [45] and [46] [8] indicate logarithmic-helical antennas feature a constant radiation impedance and low reactance, making them extensively utilized in photoconductive emitters. Presently, these antennas primarily operate within the low-frequency band of THz, with limited research focusing on the high-frequency band. However, current photoconductive antennas still face challenges such as large material loss, low photoelectric conversion efficiency, and limited output power.

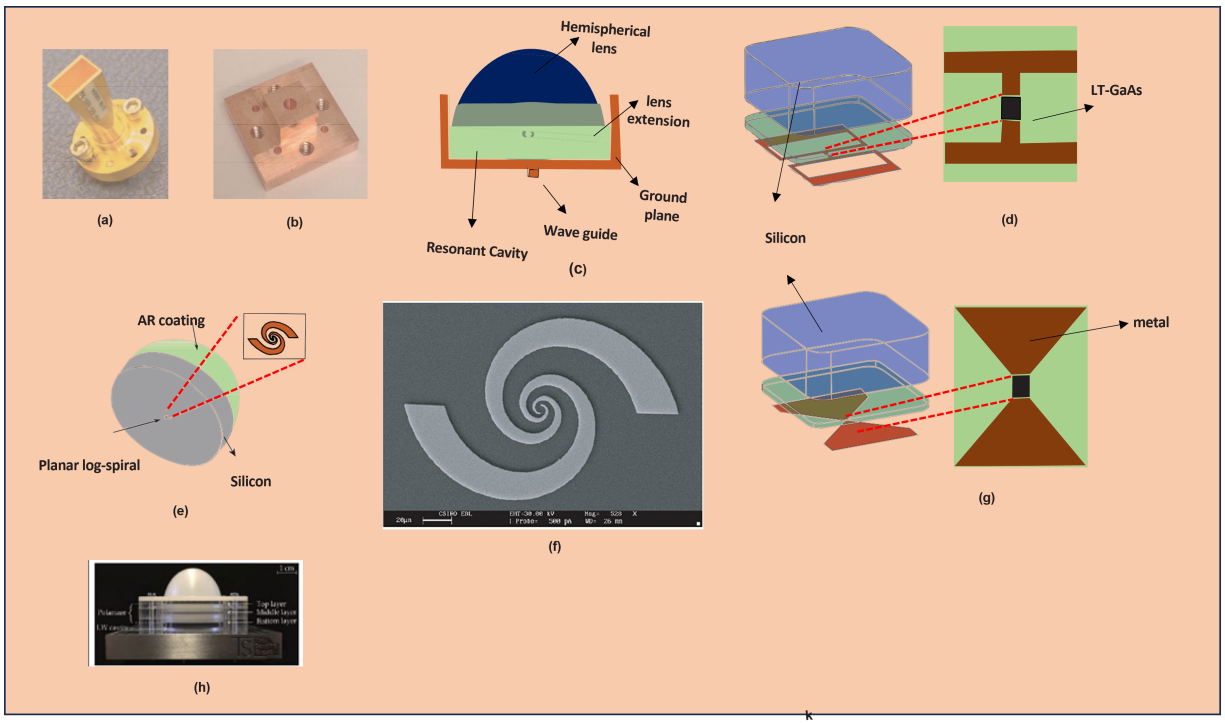

Figure 2.5: Various types of Thz antenna: (a) Rectangular THz horn [3] (b) multi-angle THz horn [4] (c) extended hemispherical silicon THz lens [5] (d) H-dipole THz PCA [6] (e) planar log-cycle fed THz lens antenna [7]. (f) spiral shape THz PCA (g) Bow-tie THz PCA [8] (h) Fabricated THz lens antenna [9]

- **Microstrip Antennas**

  However, for communication purposes, due to integrating capability and low loss, the horn and the planar antenna have been recommended. In most recent developments, horn antennas have been used to achieve high gain, However, this type of antenna suffers from phase error and is not compact, making it difficult to incorporate them into planar circuits [41]. The other option is the planar microstrip antenna, which is inherently limited by its gain and bandwidth despite its good integration capability, and relatively simple fabrication using conventional techniques and its compact size as shown in Figure 2.6. However, in this thesis, the focus is placed on the modified planar antenna array to achieve bandwidth and gain performance.

2.4.5 THz Planar Antenna Array

The primary focus of 6G wireless communication is the development of high-gain antennas with wider bandwidth and high radiation efficiency. To enhance the efficiency and gain of a single-unit cell, the antenna array technique is employed. This technique involves feeding the elements of the microstrip array antenna using either a single line or multiple lines. Based on the feeding method, the array can be classified into three categories: (a) Corporate/parallel fed, (b)

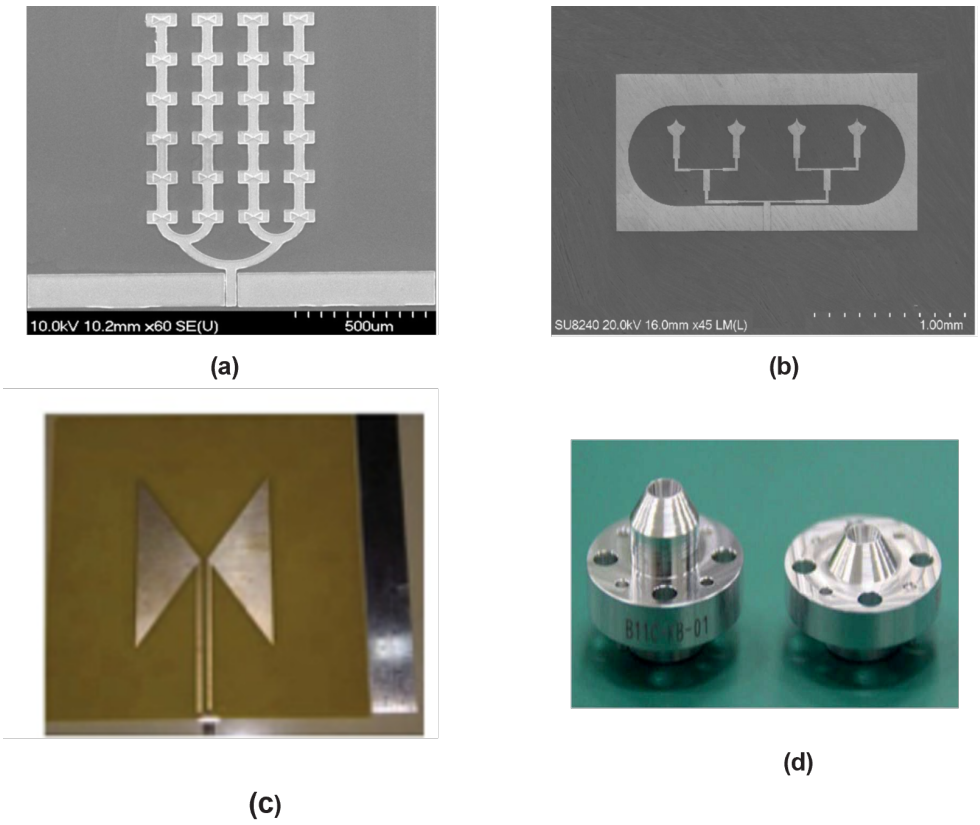

Figure 2.6: Various types of a planar antenna (a) CPW-based THz antenna array (b) PICA antenna array [10](c) planar bow-tie THz antenna [11] (d) processed based on aluminum materials Corrugated horn [12]

Series fed, and (c) Hybrid fed. Given that it's widely known that the maximum gain of a unit-cell rectangular microstrip antenna can reach up to 8 dBi. The antenna realized gain can be calculated from the following equation 2.1. To further enhance the gain, array techniques are employed. Moreover, as a rule of thumb, doubling the number of elements in a corporate/parallel/hybrid array will enhance the antenna gain by 3 dB, contributing to the overall antenna gain through proper design.

$$\text{Gain} = \eta \times D \tag{2.1}$$

$$G_{\text{dB}} = 10\log(G) = 10\log(\eta \times D) \tag{2.2}$$

where G is the antenna gain η is the antenna efficiency, and D is the antenna directivity.

2.4.6 Series Fed Array

Series-fed antennas are a fundamental design in antenna array configurations, primarily valued for their simplicity and efficiency in power distribution. These antennas feed input power se-

quentially from one end (port1) of the array to the other as shown in Figure 2.7(a), ensuring minimal transmission line losses compared to parallel-fed designs. However, a significant challenge with series-fed antennas is their susceptibility to frequency-dependent phenomena such as beam squint. Beam squint occurs because the phase shift on the antenna element changes with frequency, affecting the main beam angle and potentially affecting the antenna's performance over its operating range. To mitigate these issues, series-fed arrays often employ strategies to effectively manage phase transitions. Although series-fed antennas inherently have narrow bandwidths and potentially high side-lobe levels (SLL), their design simplicity and lower loss characteristics make them attractive for many applications [47] [48]. Figure. 2.7(a) shows the basic configuration of the serially fed microstrip antenna array. The compact configuration of these arrays enables compact and efficient setups, making them particularly suitable for applications where space and power efficiency are critical.

2.4.7 Corporate/Parallel Fed Array

Corporate/parallel-fed array, the power distribution system is designed to ensure that each antenna element receives an equal amount of power with the required phase shift. This is typically achieved using a complex network of power dividers and phase shifters. In these configurations, each antenna element or subgroup of elements is fed directly from a common source through a network of transmission lines. Figure 2.6(b) illustrates the typical layout of a corporate/parallel fed array, highlighting the network of feed lines that distribute power across the array. The primary advantage of corporate/parallel feeding is its ability to control the phase and amplitude across the antenna array, which is crucial for beamforming applications. Moreover, the design supports wider bandwidths and higher power handling capabilities than series-fed arrays, enhancing their suitability for high-demand applications like radar and satellite communications. Additionally, the parallel feed approach tends to support wider bandwidths and higher power handling capabilities than series-fed arrays. In terms of design, the corporate/parallel fed array approach utilizes a power dividing mechanism that splits power by 2N (Where N=1,2,6,16), while using tapered lines or a quarter-wavelength transformer as shown in Figure 2.7(b). A significant challenge in designing N ×N corporate fed/parallel fed arrays is managing the impedance of the feed lines, which may need to exceed 110 Ω for higher N values. Current PCB fabrication limits, typically around 50 Ω, make it challenging to maintain the required spacing (D1 and D2) between each branch to suppress grating lobes effectively [49]. According to antenna theory, the spacing should be less than or equal to $\lambda_0/2$ (Where λ_0 is the wavelength in free space) to prevent the formation of grating lobes.

2.4.8 Hybrid Fed Array

Hybrid-fed arrays incorporate features from both series-fed and corporate/parallel-fed configurations, offering a balanced approach to addressing the specific challenges of antenna design for high-performance communication systems [50] [51]. This configuration aims to exploit the best attributes of both feeding techniques to enhance antenna performance across a range of parameters including gain, bandwidth, and radiation efficiency. Figure 2.7(c) illustrates a typical layout of a hybrid-fed antenna array, showing how the elements are interconnected to maximize the advantages of both series and parallel configurations. Table 2.2 outlines the advantages and disadvantages of different microstrip array antenna techniques, as detailed in references [51]–[56].

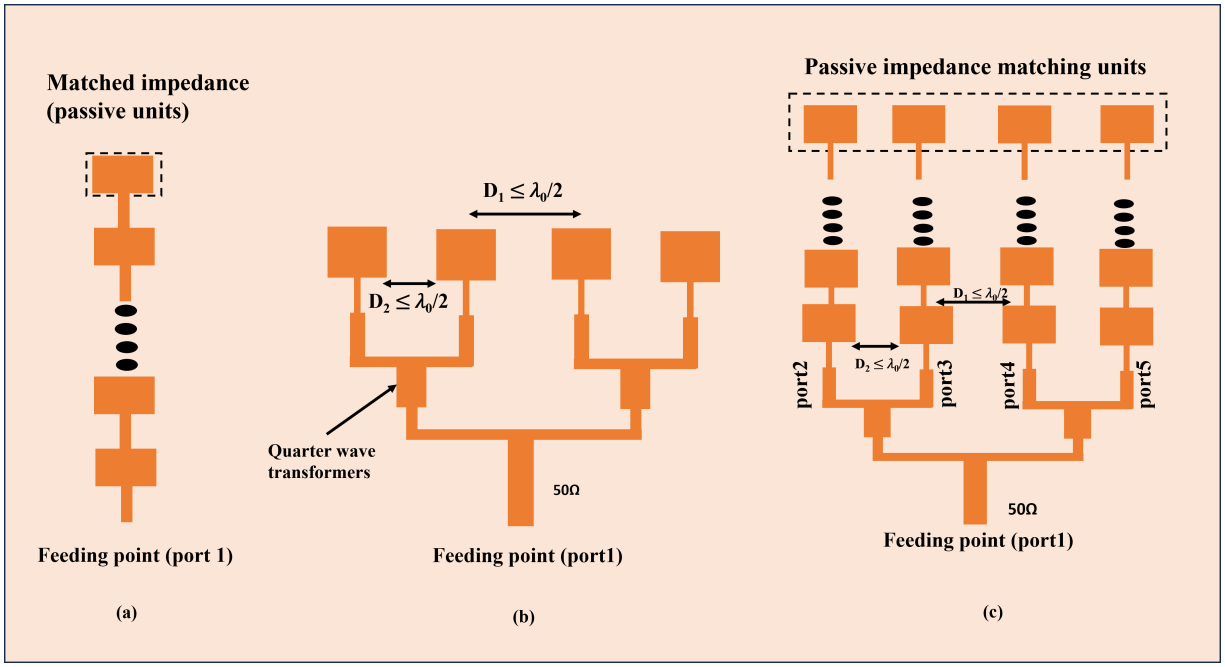

Figure 2.7: Basic configurations of Antenna Array: (a) Series-fed antenna array (b) corporate/parallel fed array (c) hybrid-fed antenna array.

2.5 AI-driven Antenna Design Techniques

The evolution of wireless communication technologies toward 6G highlights the need for advanced antenna designs to meet the high frequency and high bandwidth requirements of THz frequencies. Addressing these requirements, the design and optimization of THz frequency antennas in 6G wireless communication face unique challenges, including complex topological profiles, material composition and stringent performance requirements [57]. These challenges require innovative approaches in antenna design, leveraging advanced AI-driven technologies to achieve efficient and robust solutions. This section explores various AI-driven techniques used in antenna design, focusing on global optimization and surrogate model-assisted evolutionary algorithms.

Table 2.2: Comparison of Antenna array configuration

No	Antenna Array configuration	Advantages	Disadvantages
1	Series Fed Antenna Array	• Simplifies design and fabrication processes. • Reduces feed network complexity. • Minimizes losses by decreasing the number of connections. • Ensures consistent gain across the array with a linear feeding method.	• Narrow bandwidth. • Limited beamforming capabilities. • Difficulty in controlling the amplitude and phase of each element independently.
2	Corporate/Parallel Fed Antenna Array	• Improved beamforming capabilities. • Wide bandwidth. • Better control of amplitude and phase. • Achieve higher gain due to the ability to feed each element with an optimized amplitude and phase.	•Complexity in the design increases with the number of elements and the potential for uneven power distribution. • Insertion losses of the power dividers reduce the gain. • $\lambda/4$ transformer for impedance matching, 50 μm minimal widths of lines.
3	Hybrid Feed Antenna Array	• Improved performance in terms of bandwidth and beamforming. • Achieve higher gain to better signal strength and quality over the covered areas.	• Design complexity and cost are higher, so balancing the feed network can be challenging. • Potentially higher losses due to combined feed networks. • Requires careful balancing of feed techniques to avoid performance degradation.

2.5.1 Antenna Design and Optimization

The design of modern antennas often involves parametric studies, where engineers adjust a few key design parameters in discrete steps to understand their impact on antenna performance [58] as shown in Figure 2.8. While this approach combines engineering experience with system exploration, it is exhaustive and does not guarantee a successful outcome, especially for complex antenna structures with many interrelated parameters and specifications. To overcome these challenges, automated design approaches through optimization are preferred. This method allows for the concurrent consideration of multiple design parameters and facilitates the discovery of high-quality design solutions. However, traditional numerical optimization techniques have their limitations:

Local Optimization

Antenna local optimization often relies on a good initial design as a starting point to ensure success. Unfortunately, for many practical antenna design cases, it is often not possible to obtain a good initial design [59] [60].

Global Optimization

Antenna global optimization requires extensive full-wave electromagnetic (EM) simulations (i.e., objective function evaluation) to obtain a near-optimal design, making it computationally expensive and time-consuming [61] [60].

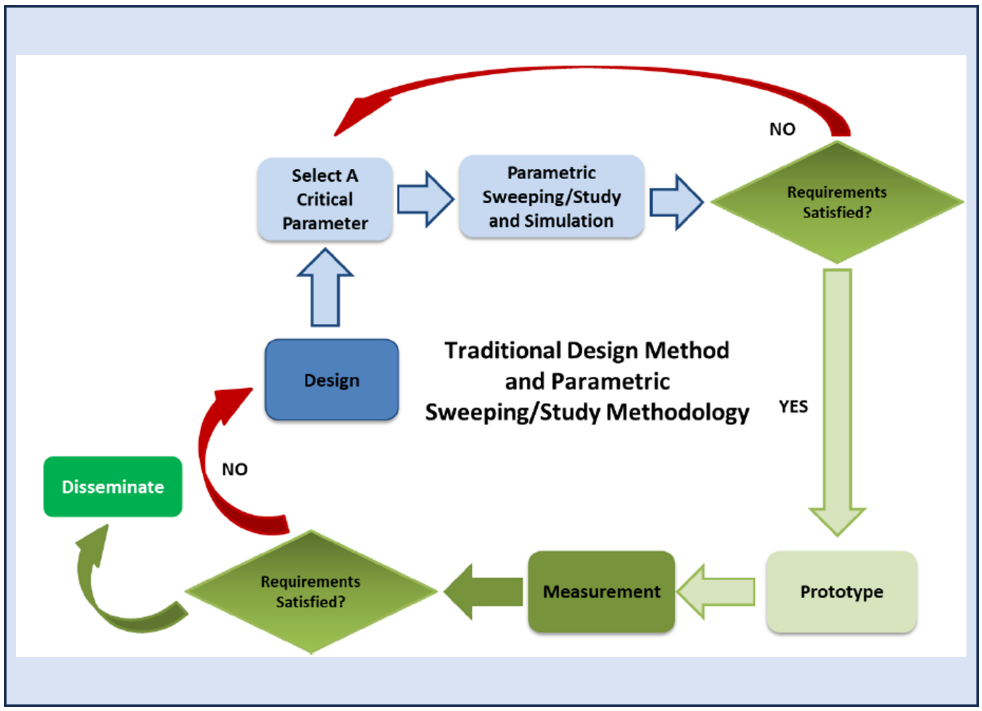

Figure 2.8: Workflow for the manual design of antennas

Given these constraints, standard local and global optimization techniques are not always suitable for the automated design of various types of antennas, necessitating more efficient and intelligent approaches. To overcome these limitations by integrating AI techniques, specifically machine learning (ML), into the kernel of conventional numerical optimization methods to make them more efficient and robust. This approach often takes the form of surrogate modelling, where predictions from meta-models or data-driven models replace expensive full-wave electromagnetic simulations in the optimization process.

2.5.2 Antenna Global Optimization and Surrogate Model-Assisted Evolutionary Algorithms

To address the limitations of traditional optimization methods, global optimization techniques enhanced by surrogate models were developed. These methods combine the robustness of evolutionary algorithms (EA) with the efficiency of surrogate models to reduce the computational burden of antenna design optimization. Evolutionary algorithms such as genetic algorithm (GA), differential evolution (DE), and particle swarm optimization (PSO) perform a nature-inspired global search of the antenna's design space to find a near-optimal design. The primary advantages of using EA in antenna design include independence from the initial design and avoidance of time-consuming and manual tuning [58]. However, due to the large number of full-wave electromagnetic simulations required, EA's computational budget may become prohibitive. Furthermore, EA often exhibits slower convergence speed for certain antenna design problems [57]. To reduce computational costs and enhance the efficiency of the EA, surrogate models built using ML techniques were used to replace full-wave EM simulations in their optimization kernels. Such EAs, called surrogate model-assisted EAs (SAEAs), tend to be more efficient and provide higher-quality design solutions than their pure EA counterparts [62] [63]. The Surrogate Model Assisted Differential Evolution (SADEA) family of algorithms for antenna synthesis exemplifies this approach, which combines evolutionary computation with supervised learning techniques [64]–[69].

2.5.3 Surrogate Model-assisted Differential Evolution for Antenna Synthesis Series

Surrogate model-assisted differential evolution (SADEA) presents a series of advances in antenna design optimization, addressing the challenge of high computational costs and the need for robust design exploration.

SADEA-I (1st generation)

SADEA-I combines evolutionary computation with supervised learning techniques to improve the efficiency of antenna design optimization. This approach eliminates the need for good initial designs and ad hoc processes, providing a more general and robust framework suitable for a variety of antenna design problems. SADEA-I has proven to significantly reduce optimization time and improve design quality compared to traditional methods [64].

M-SADEA (2nd generation)

M-SADEA (multi-fidelity surrogate model-assisted differential evolution) introduces multi-fidelity modelling, which uses a combination of low- and high-fidelity models to filter and re-

fine design solutions. This approach improves the efficiency of surrogate modelling, making it effective for high-dimensional antenna structures. By employing radial basis functions (RBF)-assisted local optimization and adaptive Gaussian process (GP) surrogate modelling, M-SADEA reduces training costs while maintaining optimization efficiency [65].

P-SADEA (3rd generation)

P-SADEA introduces parallel processing to expedite the optimization process, leveraging parallel computing resources for the simultaneous evaluation of multiple designs. This generation utilizes Bayesian neural network (BNN)-based agent modelling and adaptive lower confidence bound (LCB) pre-screening. This combination reduces the computational cost of surrogate modelling, making P-SADEA suitable for optimizing complex and high-dimensional antenna structures [66].

TR-SADEA(4th generation)

The TR-SADEA (Training Cost Reduced Surrogate Model-Assisted Hybrid Differential Evolution for Antenna Optimization) method improves the efficiency of optimizing complex antennas with numerous design variables and specifications [67]. Its features:

- Self-Adaptive Gaussian Process Surrogate Modeling: Dramatically reduce training time while maintaining predictive accuracy by clustering candidate designs and sharing GP models.
- Hybrid optimization framework: Combined with RBF-assisted local optimization, it improves convergence speed and reduces calculation time. This approach replaces some GP models early in the optimization process.

SB-SADEA (5th generation)

The SB-SADEA (Adaptive Bayesian Neural Network Surrogate Model-Assisted Differential Evolution for Antenna Optimization) method introduces significant improvements in the convergence speed and training cost of antenna design optimization [68]. Its key features:

- Replaces the traditional Gaussian Process (GP) model with a Bayesian Neural Network (BNN).
- Provides high-quality predictions with statistically grounded uncertainty for each candidate design.
- educes the training complexity significantly compared to GP models, making it suitable for antennas with many design variables and specifications.

- Integrating a self-adaptive LCB approach with a BNN-based surrogate model.
- Enhance the balance between exploration and exploitation during optimization, improving convergence speed and solution quality.

Recently, the SADEA method has proven suitable for optimizing complex and high-dimensional antenna structures. Techniques such as radial basis function (RBF)-assisted local optimization and adaptive Gaussian process (GP) surrogate modelling are used to reduce the training cost of the surrogate model while maintaining optimization efficiency. To further reduce computational costs, the harmonious working of Bayesian neural network (BNN)-based surrogate modelling and self-adaptive lower confidence bound (LCB) pre-screening is employed, as exemplified by the latest SADEA algorithm. The improved PSO approach has also been demonstrated using antenna problems, including SIW cavity-backed slot antennas and linear arrays, resulting in good design solutions. However, in this thesis, the first generation of SADEA and SB-SADEA, the latest implementations, have been successfully employed, and SB-SADEA has been shown to be very efficient for contemporary EM design synthesis.

2.6 Summary

The advancement of 6G wireless communications is closely tied to the development and integration of THz technology. This chapter delves into the evolution of wireless communications technology, highlighting the transformative potential of THz frequencies, which are critical to achieving the ultra-high data rates and minimal latency envisioned by 6G. THz technology, characterized by high bandwidth capabilities, is vital for applications requiring rapid data transmission and high network densities. Challenges associated with THz frequencies, such as significant atmospheric absorption and the need for advanced antenna designs, are also discussed. Innovative solutions in materials science and antenna design are considered critical for efficient utilization of the full spectrum of THz frequencies. Additionally, the chapter highlights the role of artificial intelligence (AI) in optimizing antenna design, which promises to simplify the design process, enhance performance metrics, and reduce computational costs.

Chapter 3

High-Performance Sub-THz Planar Antenna Array

3.1 Introduction

THz spectral region from 0.1 THz to 3 THz is envisaged to hold immense potential in the next generation of wireless technologies. Recently, research has focused on this terahertz gap, because of its unprecedented channel capacities. At the physical layer, the design complexities and fabrication of THz devices, especially antennas, are the prime bottlenecks to realizing its full potential. This article introduces a cost-effective, easy-to-fabricate, and reproducible sub-THz antenna design based on single-layer planar printed circuit board technology [70]. The sub-THz band is selected for the antenna design due to its suitability for short-range applications, despite challenges such as increased free space loss and atmospheric attenuation. However, communication at the sub-THz band is still possible up to 1 km at 300 GHz under certain assumptions. The antenna incorporates carefully designed quasi-cross slots and applied machine learning-assisted global optimization techniques to achieve the desired performance metrics. The antenna performance is elucidated through numerical simulations and verified through a rigorous in-house THz experimental framework around 100–110 GHz. The proposed antenna offers a peak gain of 13.90 dBi with a variation of less than 1 dB throughout the 100-110 GHz band. The antenna has the potential to achieve terabit per second(Tbps)data rates and futuristic high-resolution short-range THz imaging applications.

3.2 Design and Optimization of THz Antenna

This section details the comprehensive design process of both the individual antenna elements and their subsequent integration into an array configuration. The focus is on achieving optimal performance metrics, such as high gain, broad bandwidth, and minimal mutual coupling, through design strategies and advanced optimization techniques.

3.2.1 The Unit Element Design

The first step involves the design of a rectangular patch antenna with a dimension of 1.71 mm × 0.60 mm as shown in Figure 3.1(a), aiming the resonant frequency of 105 GHz using the standard design equations. The antenna is designed on RT/Duroid 5880 substrate with a dielectric constant of 2.2 a thickness of 0.125 mm and a dissipation factor of 0.004, and a copper thickness of 17.5 μm.

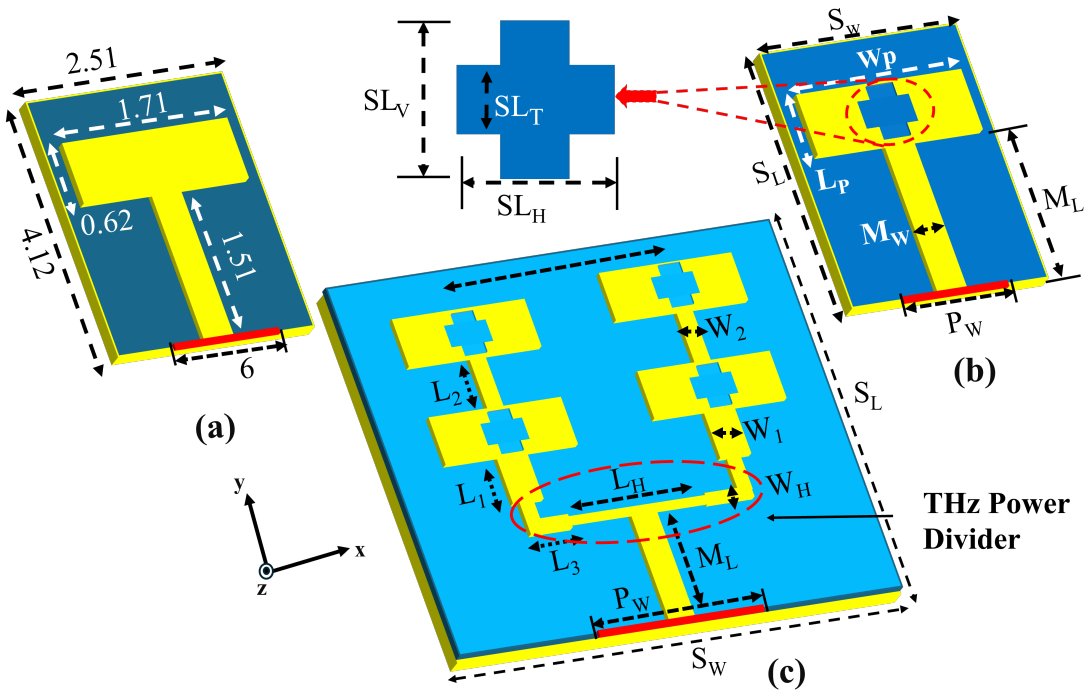

Figure 3.1: Design evolution and geometrical dimensions of the proposed sub-THz antenna.

The specific dimensions of the antenna were optimized to achieve a balance between the antenna's resonant frequency and maintain its compact size, ensuring compatibility with compact THz systems. The antenna is modelled in CST Microwave Studio (CST-MWS 2022) using the finite integration technique (FIT) method with an accuracy of -40 dB and a maximum cell density of 20 cells per wavelength, resulting in approximately 3,344,156 hexahedral mesh cells in total. The antenna design comprises a driven rectangular patch incorporating a slot. These slots are strategically positioned at the head and centre to create a quasi-cross-slot configuration as shown in Figure 3.1(b). This is particularly important given that patch antennas inherently possess narrowband. Enhancing the impedance bandwidth, one approach is to increase the substrate thickness and reduce the quality factor. However, this can lead to increased antenna dimensions and losses, along with altered radiation patterns due to stronger surface waves, which are undesirable in the sub-THz band. To maintain simplicity in the sub-THz band design and reduce complexities, quasi-cross slots were incorporated into the radiating patches, a technique proven effective in literature for modifying current paths and generating higher-order current

modes. Such modifications lead to notable improvements in the antenna's performance, including reduced side-lobe levels, increased gain, and correction of the squint effect, thereby overall enhancing the radiation characteristics. Furthermore, the antenna's bottom side is covered with a full copper layer, serving as a ground plane to permit broadside radiation beams.

3.2.2 Hybrid 2×2 Array Design

Designing antenna arrays is crucial for enhancing THz system performance, especially for achieving high antenna gain. Our design process commenced by evaluating various parameters sensitive to optimization performance within a corporate-fed network as shown in Figure 3.1(c). The designed feeding network, based on transmission line theories, precisely controls the amplitude and phase of the current supplied to each antenna element, ensuring effective power distribution. The feed junctions and transitions are carefully matched using $\lambda_0/4$ transmission line sections to minimize reflections, where even minor discrepancies in dimensions can substantially affect the array's bandwidth and performance—key considerations for THz sensing and imaging applications that demand exceptional precision and reliability.

A hybrid parallel-series fed array configuration was employed to achieve a compact size and high gain beam. The inter-element element gap was optimized at 1.32 mm (0.68 λ_g or 0.46 λ_0), as demonstrated in Figure 3.1(c) Where λ_g and λ_0 represent the guided and free space wavelengths, respectively, at 105 GHz. This optimum spacing was determined using the SADEA-I algorithm, which aims to minimize mutual coupling and improve radiation efficiency, thus enhancing bandwidth and array gain to address the significant path loss challenges at sub-THz (100-110 GHz) frequencies.

In corporate feeding network two-way power divider is used which divides 50 Ω, feed line into a 100 Ω as depicted in Figure 3.1(c). Quarter wave transformers are used to match the 100 Ω lines to the edge impedance. To ensure desired impedance matching across the target frequency band, precise adjustments are made to the feed line dimensions, including width and length, to achieve impedance levels of 50 Ω, 70 Ω, and 100 Ω. Concurrently, the array's symmetrical layout around the y-axis plays a significant role, not only in improving the uniformity of the radiation pattern but also in simplifying the fabrication process.

Through extensive optimization, involving over 550 iterations with the SADEA-I algorithm, we established the optimal dimensions for a high-performance array topology, showcasing the critical role of AI-driven techniques in achieving stringent design criteria in THz antenna arrays.

3.3 Geometric Optimization and Performance Enhancement

The design of the proposed antenna presents significant challenges, primarily due to its small form factor and the need for high gain and directivity in the sub-THz band. Additionally, the requirement for the antenna to maintain a broad beamwidth—to facilitate detection from multiple

angles in THz imaging—further complicates the design. This requires maintaining a relatively consistent boresight gain across the desired bandwidth, which leads to the need for geometrical optimization in the slotted patch as well as in the feeding structure to optimize overall performance within the target band.

3.3.1 Optimization Algorithm: SADEA-I

To obtain the optimal antenna design, the Surrogate-Assisted Differential Evolution Algorithm for Antenna Synthesis (SADEA-I) [19] is employed via the MATLAB Antenna Toolbox. SADEA-I is the first generation of the SADEA algorithm series [64], [65], [67]–[69]. SADEAs combine supervised learning and evolutionary search techniques to effectively explore and exploit the antenna design search space. In SADEA-I, the supervised learning method used is Gaussian process (GP), which constructs surrogate models that approximate antenna performances. The surrogate modeling works harmoniously with the differential evolution (DE)-based global search for a balanced exploration and exploitation of the design space. The model management method used in SADEA-I is the surrogate model-aware evolutionary search framework [71].

In each iteration, a surrogate model is built using the available simulated candidate designs and their performances. New candidate designs are generated by DE search operators, and their performances are predicted by the GP surrogate model. Using the prediction results, the predicted best candidate design is simulated and used to update the surrogate model for the next iteration. This iterative process continues until the optimal design is obtained. More details about SADEA-I are in [64].

Comparison with Other Optimization Techniques

Widely utilized local optimization techniques (e.g., Trust Region Framework (TRF) in CST Microwave Studio) were applied, but the results were far from satisfactory; although the specifications for bore-sight gain and total efficiency were met, the max($|S_{11}|$) is poor (i.e., about -6 dB). Moreover, the use of available global optimization techniques (e.g., particle swarm optimization), was estimated to require a prohibitive amount of time without a guarantee of success [64], [69] [72]. Consequently, as described, the SADEA-I from the MATLAB Antenna Toolbox was used to obtain an optimal design. The initial phase involved element design, with design variables detailed in 3.1.

3.3.2 Objective Function and Optimization Process

The objective function is to minimize the fitness function (F_{mpa}) in Equation 3.1. This ensures that the antenna meets the target performance metrics in Table 3.3. While the overall size of the antenna is not directly specified in (1), the defined search ranges and geometric constraints are deliberately chosen to promote a compact, low-profile design. For instance, during the

optimization, the parameter (SLv) must be greater than (SLh) to maintain a minimal physical footprint which is among the main design goals.

$$F_{mpa} = \max(|S_{11}|) + w \cdot \max([6\,\text{dBi} - G_{min}, 0]) + w \cdot \max([0.70 - \eta_{min}, 0]) \tag{3.1}$$

Here, the worst performances of $|S_{11}|$, bore-sight gain and total efficiency are used, which are at different frequencies. In this equation, w denotes the penalty coefficient, preset to a value of 50, which is set empirically [59]. Instead of using a weight-sum of the three performance metrics, for which the balance of them is hard to control, specifications are provided for bore-sight gain and total efficiency. This setting ensures that violations of bore-sight gain and total efficiency specifications, denoted by G_{min} and η_{min}, are significantly penalized, prioritizing these aspects in the optimization process. After conducting 350 electromagnetic (EM) simulations, the specifications were met within a total design time of approximately 10.5 hours.

Table 3.1: Search ranges and dimensions of the single antenna element (dimensions in mm)

No	**Parameter**	**Lower Bounds**	**Upper Bounds**	**SADEA-I Optimum**
1	Patch length (L_p)	0.512	0.95	0.7075
2	Patch width (W_p)	1.61	3.5	1.7157
3	Microstrip length (M_L)	1.23	3.00	2.12
4	Feed Guide width (P_w)	6	10	6.9592
5	Microstrip width	0.20	0.35	0.3124
6	Width of Slot (SL_w)	0.20	0.32	0.2109
7	Length of Slot (SL_l)	$\geq SL_w$	0.33	0.2203
8	Vertical Slot depth (SL_v)	0.38	0.46	0.3852
9	Horizontal Slot depth (SL_h)	$\geq SL_v$	0.46	0.4779
10	Substrate Length (SL) = M_L + (2 × SL_h) + 0.2			

Using the individual elements, the array configuration is then optimized. This phase addresses the arrangement and collective behavior of the antenna elements to achieve desired array-level characteristics such as broadside gain and minimal sidelobes in the radiation pattern. In high-frequency (THz) regimes, the efficiency of microstrip lines drops significantly because of serious losses at the bends and discontinuities. As a result, developing a low-loss, planar feeding network is imperative for maintaining efficient performance. SADEA-I investigates various array configurations, including the spacing between elements, distribution patterns, and feeding strategies. The design parameters, along with their respective search ranges as detailed in Table 3.2. These parameters are crucial in reducing the fitness function, denoted as F_{mpa} in Equation 3.2, to meet the requirements. Although the antenna size is not explicitly included in the given Equation, the defined search parameters and geometric limitations are strategically set to guarantee a compact and low profile design. Thus, as part of the optimization process, the

key performance metrics and design constraints are encapsulated in the fitness function (F_{mpa}) defined as follows:

$$F_{mpa} = \max(|S_{11}|) + w \cdot \max([10\,\text{dBi} - G_{min}, 0]) + w \cdot \max([0.70 - \eta_{min}, 0]) \\ + w \cdot \max([-15\,dBi - SL_{\max(\Phi=90^\circ)}, 0]) + w \cdot \max([-10\,\text{dBi} - SL_{\max(\Phi=0^\circ)}, 0]) \tag{3.2}$$

Table 3.2: Search ranges and dimensions of the antenna array (dimensions in mm)

No	Parameter	Lower Bounds	Upper Bounds	SADEA-I Optimum
1	Horizontal line length (L_H)	0.33	4.00	3.5680
2	Horizontal line width (W_H)	0.20	0.28	0.2060
3	Microstrip length (M_L)	1.25	3.00	2.15
4	Feed line1 length (L_1)	0.40	0.90	0.8810
5	Feed line1 width (W_2)	0.32	0.46	0.3301
6	Feed line2 length (L_2)	0.60	0.90	0.7810
7	Feed line2 width (W_2)	0.20	0.25	0.2262
8	Substrate Length (S_L) = M_L + W_H(1.5 × (L_1 + W_2)) + 0.2			

After 550 EM simulations, an optimal design was obtained, with the overall optimization time being approximately 21.5 hours. Specifically, Figure 5.23 illustrates the convergence behaviour of different optimization algorithms, namely SADEA-I and PSO, by plotting the maximum reflection coefficient $|S_{11}|$ within the operational bandwidth. The term "Max $|S_{11}|$" refers to the highest $|S_{11}|$ value observed during the optimization process, which is critical for assessing and minimizing the worst-case reflection coefficient across the bandwidth.

It is evident that SADEA-I requires the least number of EM simulations to achieve the desired value compared to PSO. Specifically, SADEA-I uses an average of 550 EM simulations to meet all the specifications listed in Table 3.3. Furthermore, SADEA-I converges to achieve the current best max $|S_{11}|$ of -12.15 dB after 1028 EM simulations. In contrast, the 2022 CST-MWS PSO achieves a current best max $|S_{11}|$ of -6.12 dB after 1050 EM simulations. It is also important to note that the convergence trend for the 2022 CST-MWS TRF is not shown in Figure 5.23 due to geometrical incongruities, as mentioned earlier. In this use case, SADEA-I performs best in both optimality and efficiency.

The simulated results, shown from Figure 3.3 to Figure 3.8, meet the requirements for the desired band (100-110 GHz). The physical implementation is illustrated in Figure 3.9. The dimensions of the entire array are approximately 5.2 mm × 5.12 mm × 0.127 mm, which corresponds to 1.82 $\lambda_0 \times 1.79\lambda_0 \times 0.044\lambda_0$, where λ_0 is the free space wavelength at 105 GHz.

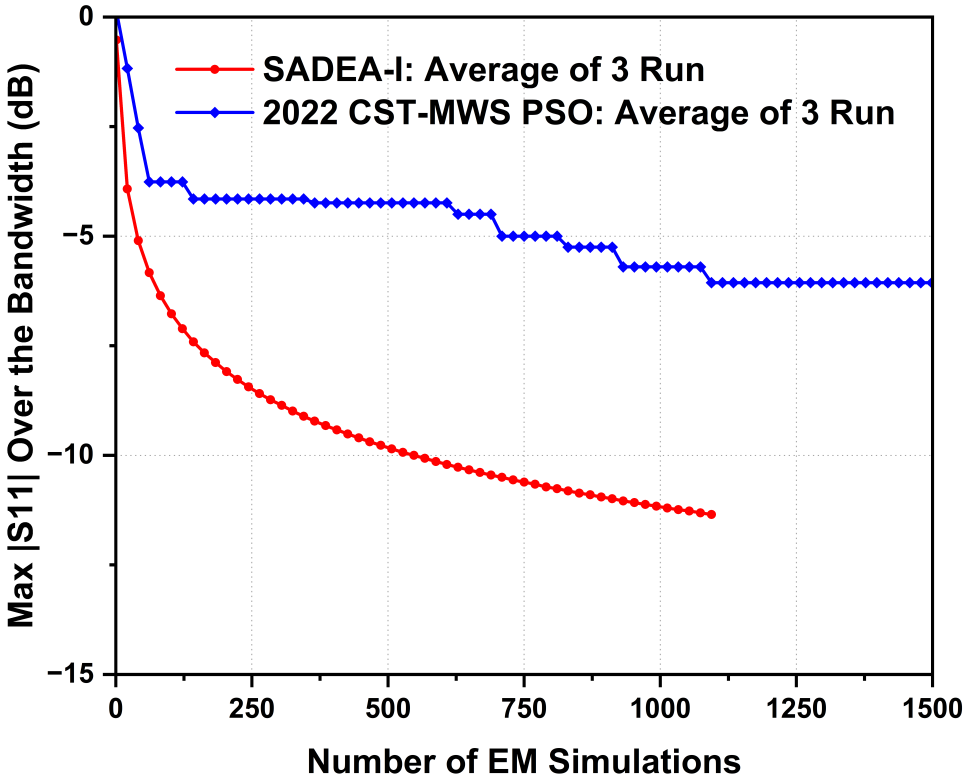

Figure 3.2: Convergence trend of SADEA-I and 2022-CST-MWS PSO

3.4 Simulated Results and Discussion

In this section, we present the results obtained from the simulations conducted to evaluate the performance of the proposed antenna array. The simulations were designed to assess various metrics, including bandwidth, realized gain, and efficiency.

3.4.1 Bandwidth and Realized Gain

For the single-element design, we initially excluded the quasi-cross slots to establish a baseline performance. The time-domain (TD) simulation in the full-wave electromagnetic CST solver was performed. The simulated reflection coefficient of a single element without quasi-cross slots shows a reflection coefficient below -10 dB and provides a narrow bandwidth of about 3.5 GHz (101–104.5 GHz), as illustrated in Figure 3.3. Upon the integration of a quasi-cross slot into the single-element antenna, the modification led to a significant redshift, causing the antenna to resonate dually at approximately 100.8 GHz and 108.4 GHz, with a return loss of less than -10 dB. To further enhance performance, the SADEA-I algorithm was used as discussed in the previous section. This adjustment expanded the -10 dB impedance bandwidth to cover a 10 GHz range, from 100 to 110 GHz. These modifications had an impact on the current distribution and impedance characteristics of the antenna. The motivation for extending the array design, extensively discussed in the antenna design section, was to examine the potential for

additional performance improvements. Following the same optimization strategy, the 4-element array not only maintained wideband performance but also showed improvement in impedance bandwidth to 10 GHz (100-110 GHz), as depicted in Figure 3.3, while maintaining the dual resonances, occurring at 100.8 GHz and 108.1 GHz, with a return loss of -25 dB and -40 dB, respectively. These resonances show a slight shift toward lower frequencies, due to structure modification. This adjustment leads to a wideband response and more consistent operational bandwidth, essential for advanced sub-THz imaging and sensing applications [73].

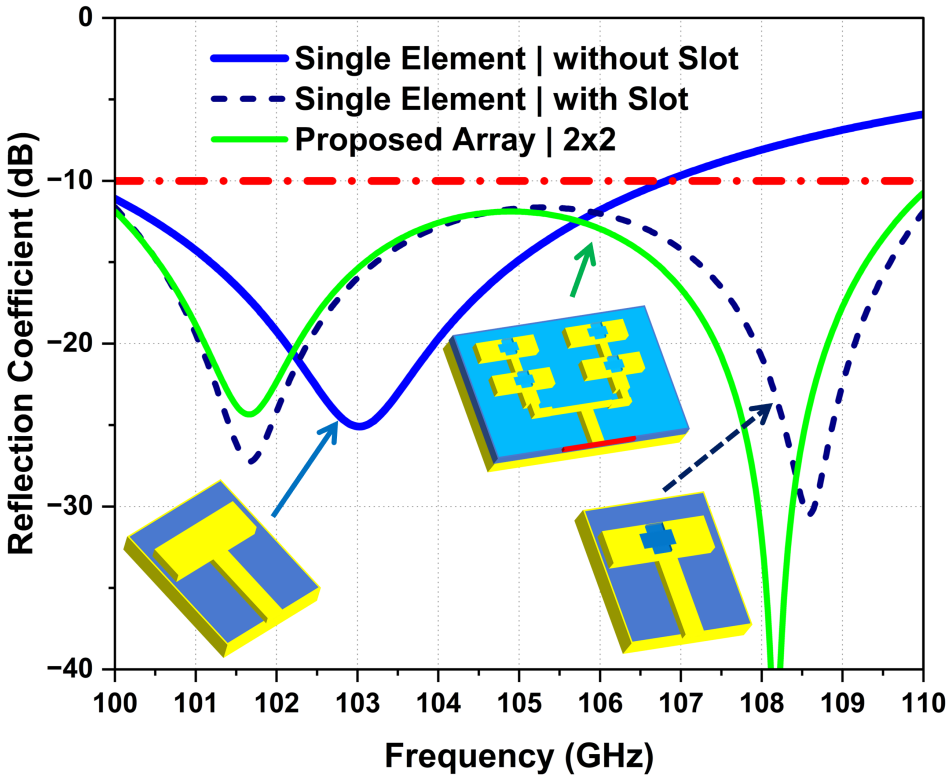

Figure 3.3: Simulated reflection coefficient of the various design configuration.

Moreover, Figure 3.4 illustrates a systematic comparison of the realized gain for the various antenna design configurations. A single antenna element without slots achieved a maximum gain of 5.65 dBi at 103.62 GHz and less than 6 dBi throughout the desired band (100-110 GHz). However, the incorporation of a primitive quasi-cross slot enhances the boresight gain by 2 dBi at certain frequencies within the operational band. After an extensive optimization using the SADEA-I algorithm, the maximum boresight gain of the single element with the quasi-cross slot increased to approximately 9.04 dBi at 105.5 GHz, resulting in an improvement of roughly 2.5 dBi. Moving to the array configurations, the 4-element array displays a significant uplift in the gain, reaching a maximum of approximately 14.43 dBi at 105 GHz, while the minimum in-band realized gain is observed to be 12.90 dBi. In contrast, the simulated realized gain consistently exceeds 13.1 dBi across the band of interest (100-110 GHz). The gain variation within the operating band of interest for this array is minimal, suggesting a stable performance across the

spectrum with variations possibly within a narrow window of less than 1 dBi. These findings underscore the impact of design and optimization strategies on enhancing the performance of antenna elements and their configurations.

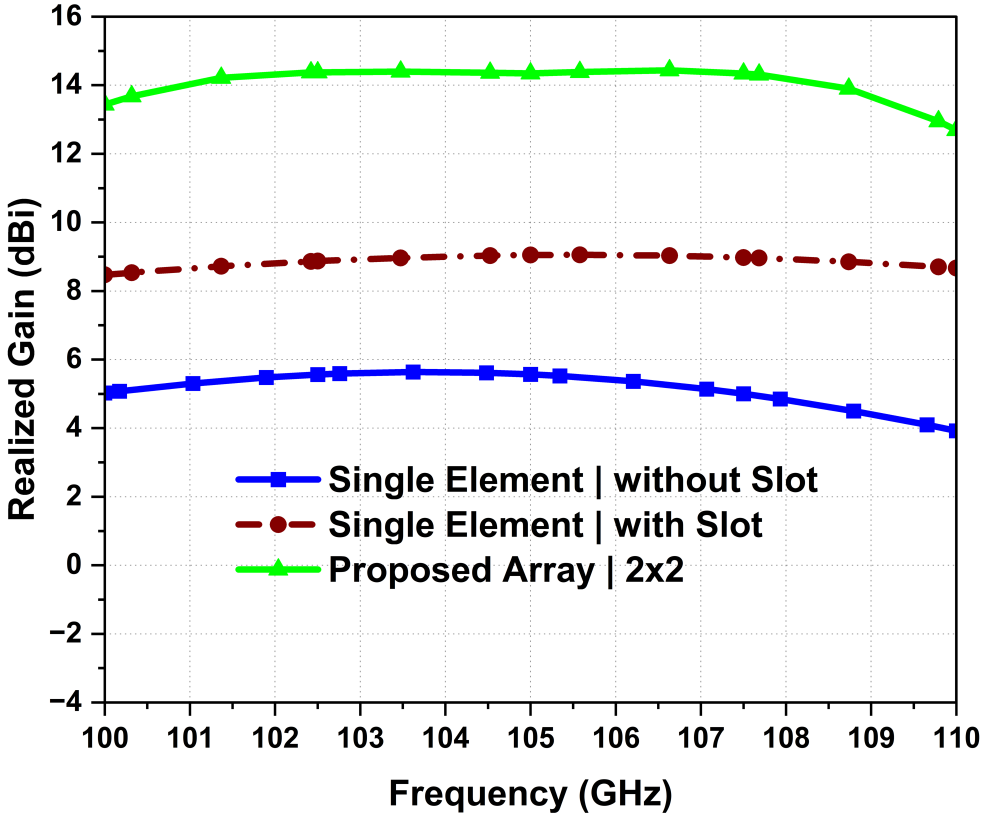

Figure 3.4: Realized gain of the various design configuration.

3.4.2 Efficiency

For the single element with quasi-cross slots across the entire band of interest, the optimized minimum In-band total efficiency is 79.21%, as illustrated in Figure 3.5. It is important to note that total efficiency represents the ratio of radiated power to input stimulated power, accounting for losses due to mismatch. Similarly, the same optimization technique was employed for the 4-element array design; the minimum in-band total efficiency is 82.2% and this performance is consistently maintained above the threshold across the entire frequency range, showcasing a stable efficiency profile.

3.4.3 Radiation Patterns

The 2D radiation patterns in the x-z plane (phi 0°) and y-z plane (phi 90°) at 100, 105, and 110 GHz are depicted in Figure 3.6(a) and (b), respectively. These patterns exhibit high stability across the frequency range. In the x-z plane (phi 0°), the half-power beamwidths (HPBWs) are

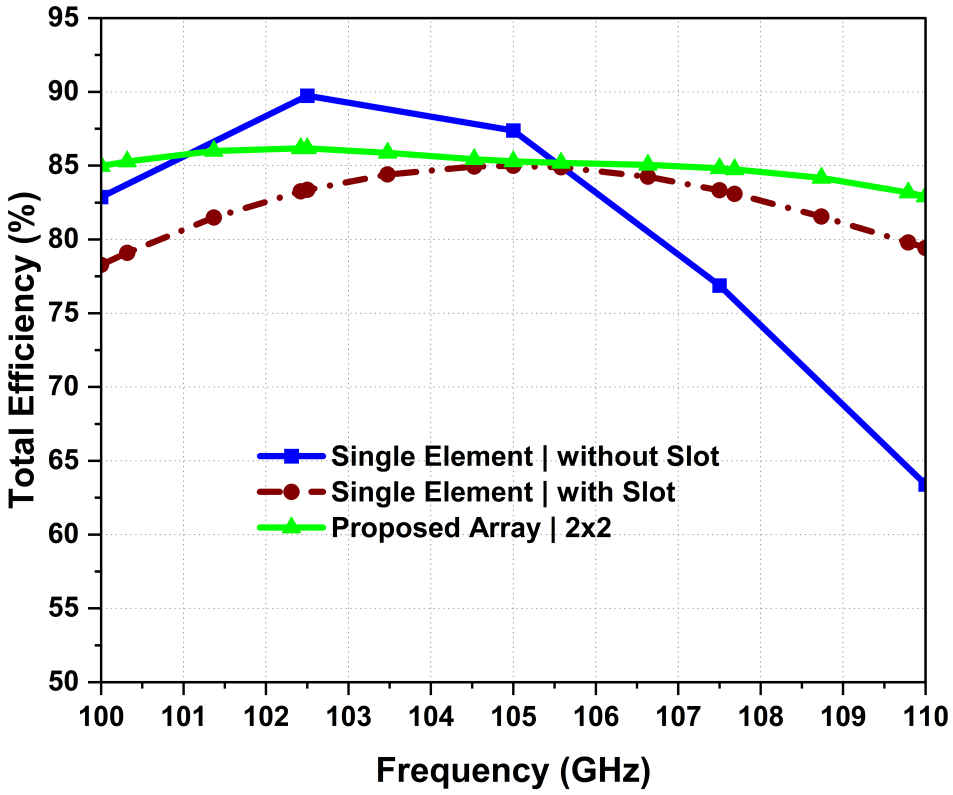

Figure 3.5: Simulated total efficiency of the various design configurations across (100-110 GHz)

23.12°, 21.5°, and 20.2°, while the side-lobe levels (SLLs) are -14.2 dB, -12.3 dB, and -10.21 dB at 100 GHz, 105 GHz, and 110 GHz, respectively. Similarly, in the y-z plane (phi 90°), the HPBWs are 39.7°, 38.6°, and 37.5°, with SLLs of -26.2 dB, -16.3 dB, and -13.1 dB at 100 GHz, 105 GHz, and 110 GHz, respectively, as shown in Figure 3.6(b). In the y-z plane (phi 90°), the HPBWs are relatively higher, due to the presence of a fan-shaped pattern, which is expected because of the linear array configuration.

Notably, the SLLs maintain a value below -10 dB in both planes, indicating minimal cross-polarization levels in the direction of the main beam, as detailed in Figure 3.7. Moreover, the antenna exhibits a has a high front-to-back ratio, consistently exceeding 30 dB within the targeted frequency band of 100–110 GHz.

The presence of connectors can introduce distortions in the radiation pattern, primarily due to the generation of additional surface waves. To minimize this impact, a longer feed line (with proper impedance matching) can be utilized to increase the sufficient distance between the connector and the radiating elements. However, in real RF circuits, the connector is absent, and the antenna array is directly linked to the RF circuitry.

Reflecting these practical considerations, Figure 3.8 presents a visual comparison of EM properties for different antenna configurations. The top row shows the radiation pattern of the antenna elements in a 3D perspective. The single element without slots shows a relatively symmetrical radiation pattern, which is altered when a slot is integrated, indicating a change in the

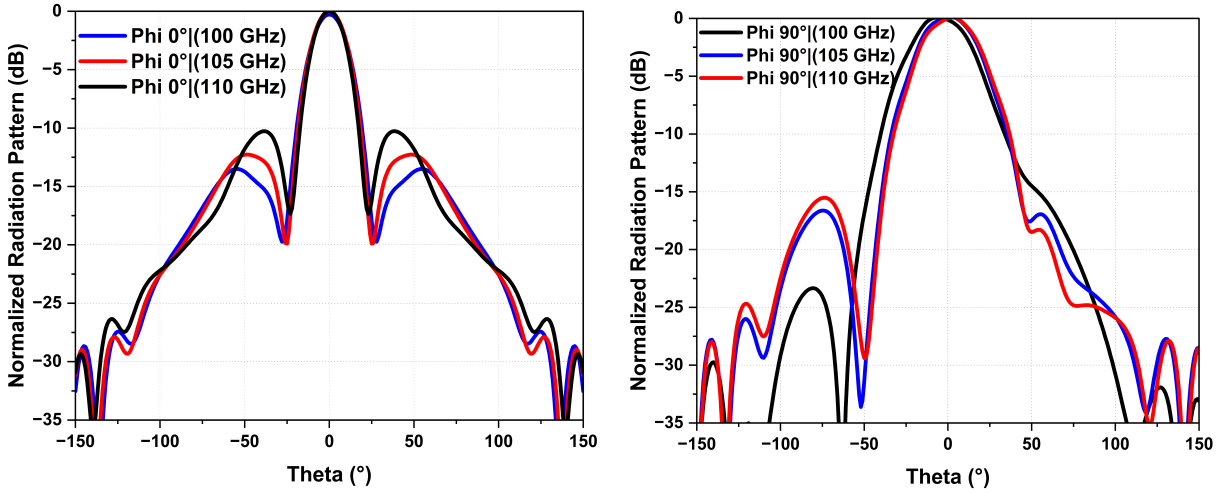

(a) (b)

Figure 3.6: Simulated normalized radiation patterns of THz planar array at various operating frequency point (a) phi 0° and (b) phi 90°.

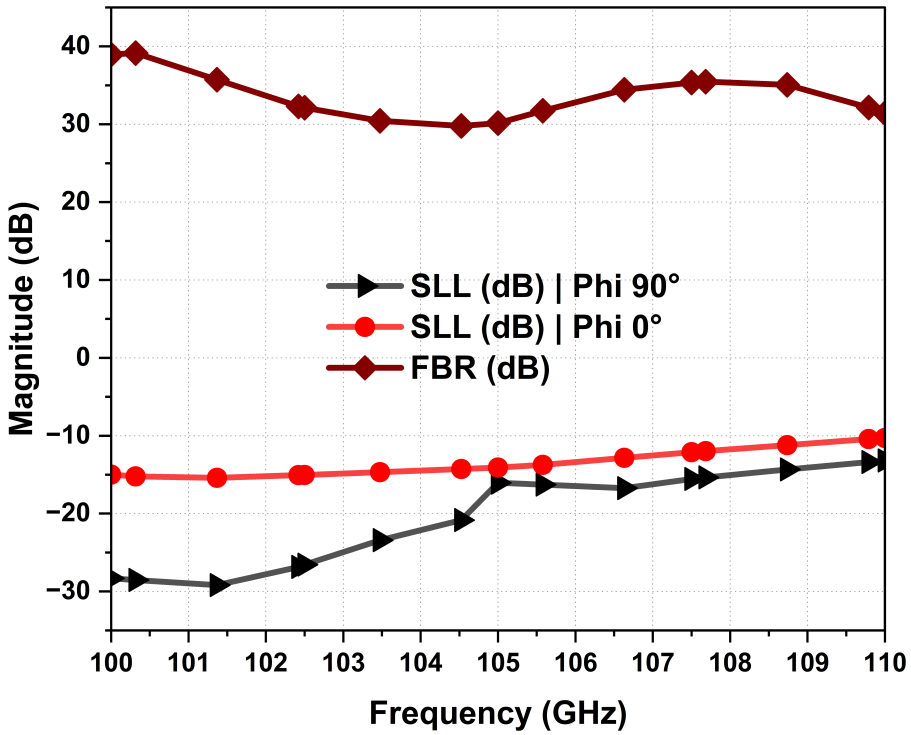

Figure 3.7: SLL | phi 0° and phi 90° and Front-to-Back Ratio of the Proposed Array Antenna.

gain and intensity of the radiated energy. The 2×2 array shows a focused beam with pronounced main lobe, suggesting a higher gain or stronger signal in a particular direction. In the bottom left, the E field distribution is shown with high intensity along the antenna elements, indicating effective radiating regions. The bottom right image maps the current distribution, with the most intense areas suggesting the primary radiating sections of the array. Notably, the feed network appears to be free of high-intensity current, which would correspond to unwanted radiation. This

observation indicates that the array has been optimized to efficiently focus radiation through its elements efficiently, thereby achieving high radiation efficiency and potentially high gain. The overall performance summary for the proposed sub-THz antenna configuration are shown in Table 3.3.

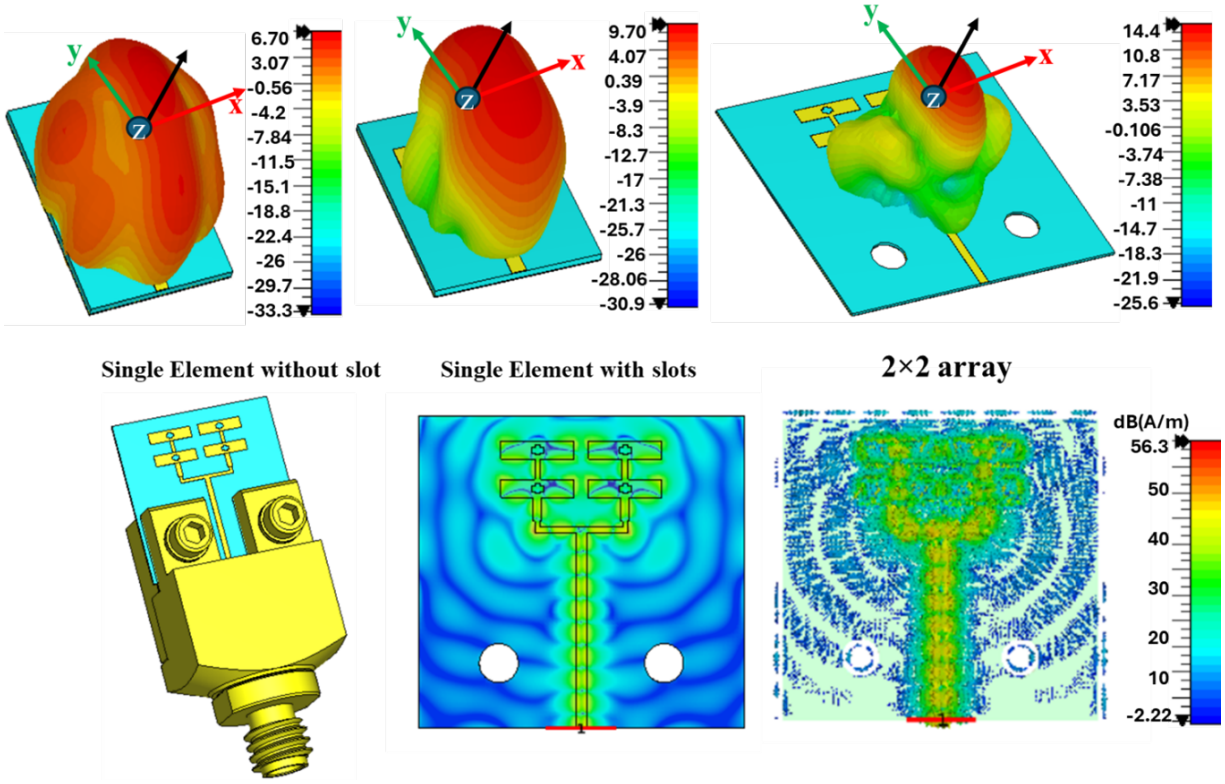

Figure 3.8: (top) 3D radiation pattern of the proposed single element and antenna array at 105 GHz. (bottom) E-field distribution and surface current distribution at 105 GHz.

Table 3.3: Performance summary for the proposed sub-THz antenna configuration

Configuration	**Design Constraints**	**Specifications**	**SADEA-I Optimum**
Single Element with Quasi-Cross Slots	S_{11} Realized Gain Total Efficiency	≤ -10 dB ≥ 6 dBi $\geq 70\%$	-12 dB 8.2 dBi 79%
2×2 Array	S_{11} Realized Gain Total Efficiency SLL ($\Phi = 90^\circ$) SLL ($\Phi = 0^\circ$)	≤ -10 dB ≥ 10 dBi $\geq 70\%$ ≤ -15 dBi ≤ -10 dBi	-11 dB 12.9 dBi 82.2% -15.12 dBi -10.21 dBi

3.5 Prototype Fabrication and Measurement Results

The sub-THz array was fabricated and tested using a low-cost standard PCB fabrication technique. For antenna array excitation, an end launch 1-mm standard solderless connector was utilized, achieving a minimal insertion loss of 0.6 dB, making it optimum for high frequencies up to 110 GHz. As soldering is not required in this type of connector, the loss due to the copper deposition during the soldering process is hence avoided (as it might adversely affect the performance at THz frequencies). It is important to note that we used 1-mm standard RF equipment in our measurement setup, which supports a maximum frequency of 110 GHz. The fabricated array, along with the integrated connector is shown in Figure 3.9. The quasi-cross slots designed and fabricated have a slightly round edge rather than being purely rectangular because the slot's edge thickness is less than 0.08 mm and is quite difficult to achieve pure rectangular shapes.

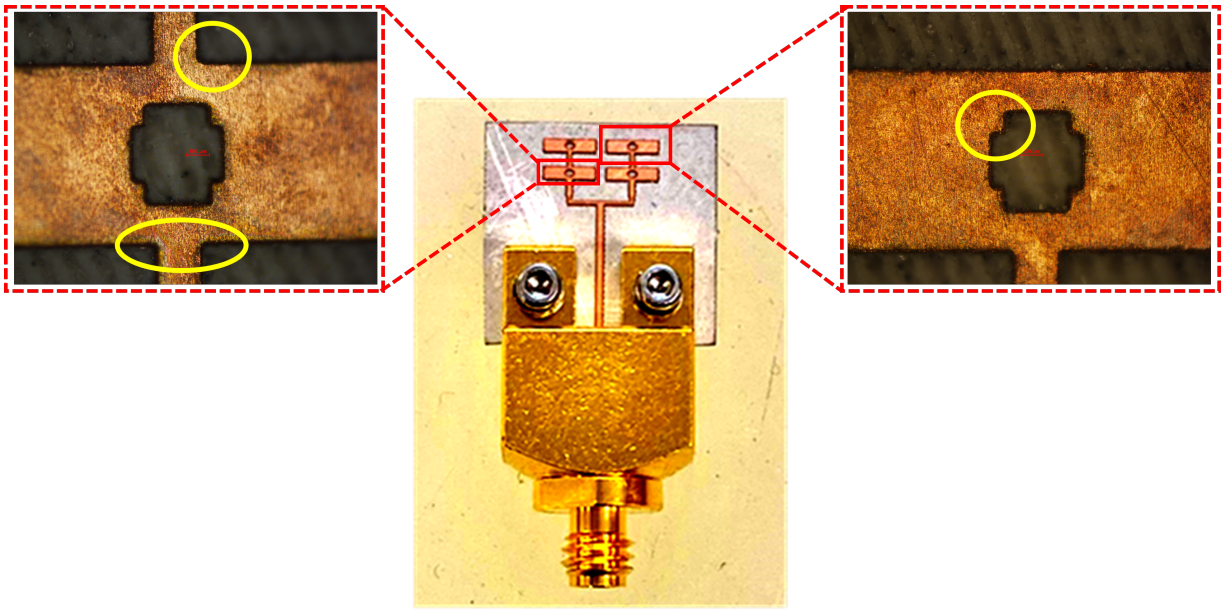

Figure 3.9: The fabricated prototype of THz planar antenna array

For mechanical reasons and to facilitate the assembly of the connector with the array, it was necessary to extend the substrate's width to 10 mm, allowing for the placement of screw holes along the substrate's width. Additionally, a feed length of 5 mm was employed to ensure a reasonable gap between the connector and the parallel feed network, preventing any influence of the connector on the radiation pattern during antenna measurements. As mentioned earlier, in practical RF circuits, the antenna is typically connected directly to the RF front end without the presence of a connector within the circuitry. Adding these additional dimensions led to no significant effect on radiation characteristics. However, the connector transition was also simulated in CST to verify that the connector is matched to 50Ω.

3.5.1 Measurement of Reflection Coefficient and Gain

The measurement setup consists of an N5260A millimetre head controller connected to E8361A (Vector Network Analyzer (VNA) with a frequency range from 10 MHz–67 GHz. The N5260A up-converts the VNA output to 110 GHz. This step ensures the accuracy and reliability of the measurement by extending the VNA capability to higher frequencies. The setup is shown in Figure 3.10. The fabricated antenna is connected to the millimetre head controller through a 1mm connector as indicated in Figure 3.10.

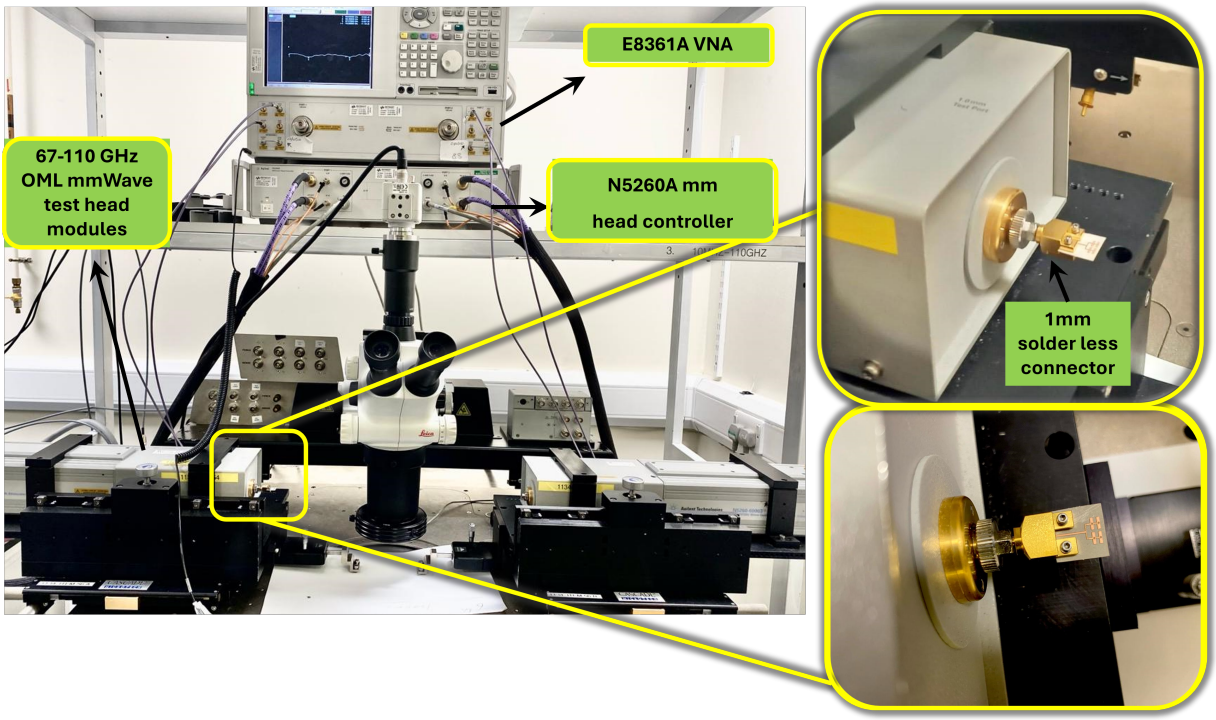

Figure 3.10: Sub-THz antenna measurement setup using OML mmWave test head module for S_{11} measurement and right side view of the array connected with mmWave extender.

The measured operational frequency band is from 100 to 110 GHz. Both simulated and measured results are depicted in Figure 3.11, illustrating a close agreement between the measured S-parameter and the simulated counterpart. The deviations observed in the measured $|S_{11}|$ are due to many practical reasons, amongst which fabrication tolerance is prominent.The gain of the antenna array (G_T) was calculated by solving the Friis transmission equation as

$$P_{\mathrm{RX}} = \frac{P_{\mathrm{TX}} G_{\mathrm{RX}} G_{\mathrm{TX}} \lambda^2}{(4\pi R)^2} \tag{3.3}$$

$$G_T = 10\log_{10}\left(\frac{4\pi R}{\lambda}\right) + 5\log_{10}\left(\frac{P_{\mathrm{RX}}}{P_{\mathrm{TX}}}\right) \tag{3.4}$$

Here, G_{RX} and G_{TX} refer to the gain of the receiving and transmitting antenna, respectively. P_{RX} and P_{TX} represent the received and transmitted powers. Since the two antennas are identical,

G_{RX} is the same as G_{TX}, and both are equal to the gain of the tested antenna. The power ratio of the received and transmitted powers (P_{RX}/P_{TX}) is equivalent to the square of the voltage gain (S_{21}), which was directly measured from the VNA. Moreover, the boresight gain versus frequency for the proposed sub-THz antenna shows a peak measured gain of 13.90 dBi at 105 GHz. Across the desired frequency band (100-110 GHz), the measured gain remains above 12.56 dBi, with a variation of less than 1.35 dBi. This confirms the antenna's effectiveness for far-field THz sensing and imaging applications.

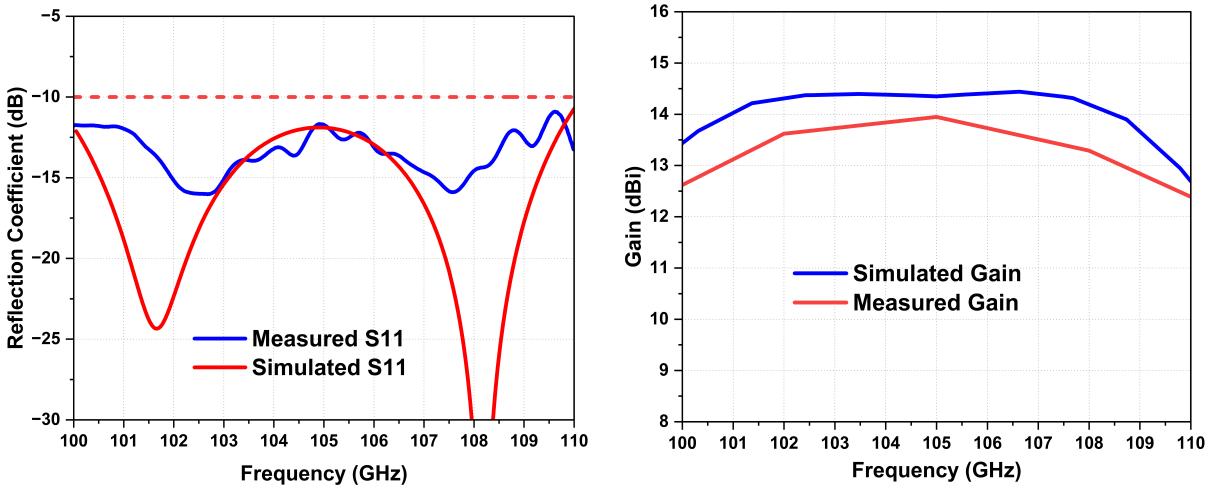

(a) Measured S_{11}

(b) Measured gain

Figure 3.11: Measured S_{11} along with the measured gain of THz planar antenna array

3.5.2 Measurements of Radiation Pattern

Following the calibration, the antenna far-field pattern measurement was conducted in a self-built environment using two identical antenna prototypes placed at a certain distance apart as shown in Figure 3.12. During measurement, the transmitting and receiving antennas were positioned face to face following the E-plane or H-plane, and should satisfy the far-field condition. Only partial radiation angle and operating frequency are measured as a result of the test system limitation in the laboratory. The measured radiation patterns in the x-z plane (as phi 0°of simulated in Figure 3.6) at 100, 105, 110 GHz are shown in Figure 3.12. The elevation plane is the principal plane because the elements' arrangement is along the y-axis. Moreover, The main beam angle in the phi 90° plane changes with frequency due to the progressive phase shifts across the series-fed patch elements, causing the main beam to squint or shift direction as the frequency changes. Note that this is an inherent phenomenon associated with series-fed arrays. In other words, the phase constant β at the antenna aperture varies with operating frequency, which results in the overall radiation pattern tilting at different frequencies. However, in the proposed design, the beam tilt in phi 90° is within 3° between 100–110 GHz, as shown in Figure 3.13, which matches quite well with the simulated results. The SLLs are below -10 dB and x-pol

levels are below -30 dB in the direction of the main lobe. The measured radiation patterns in the elevation plane are shown in Figure 3.13. The whole antenna performance could also be verified because the measured results agree well with the simulated ones.

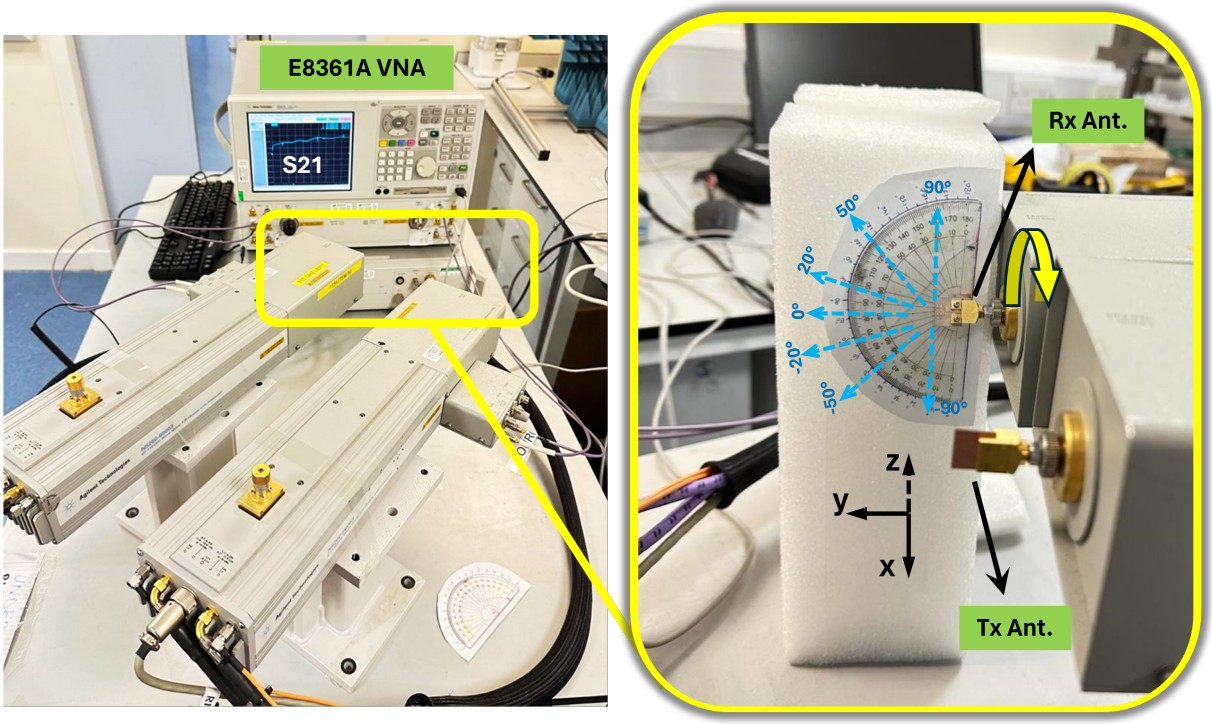

Figure 3.12: Experimental setup for radiation pattern measurement.

The measured radiation pattern agrees well with the simulated one. The patterns show some discrepancies between simulation and measurement, which is common in practical antenna testing due to factors such as fabrication tolerances, environmental conditions, or measurement errors. For instance, the simulated results for both Phi 0° and Phi 90° (represented by solid lines in blue and green, respectively) show smoother and more symmetrical lobe structures compared to their measured counterpart which exhibit variation and lower peak gains.

3.5.3 Comparison of the Proposed Antenna With State-of-the-Art

The performance comparison of the proposed array design with other closely related antenna arrays at the THz band available in the literature is presented in Table 3.4. It can be observed that the proposed array outperforms various other designs in terms of high-performance indicators such as wide impedance bandwidth (BW) and high flat gain while maintaining a compact size.

Moreover, Table 3.4 provides a comparative analysis between the proposed single-layer planar antenna array and previously reported antenna array configurations. This comparison highlights distinctions in performance metrics such as gain, efficiency, bandwidth, and design complexity. Unlike the larger and more intricate designs found in the literature, our proposed antenna stands out through its compact size and efficient performance.

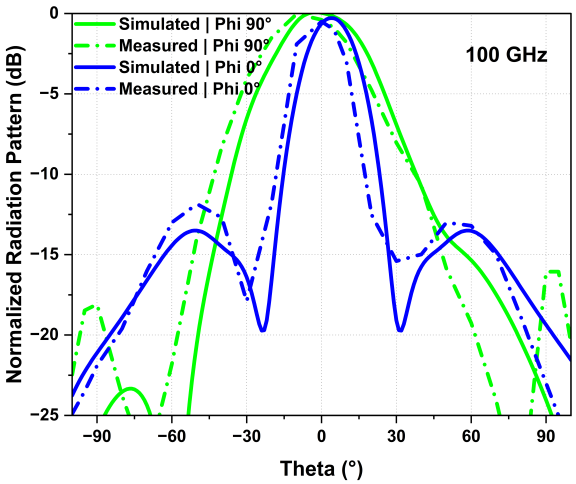

(a) Measured pattern in plane 90° and 0° at 100 GHz.

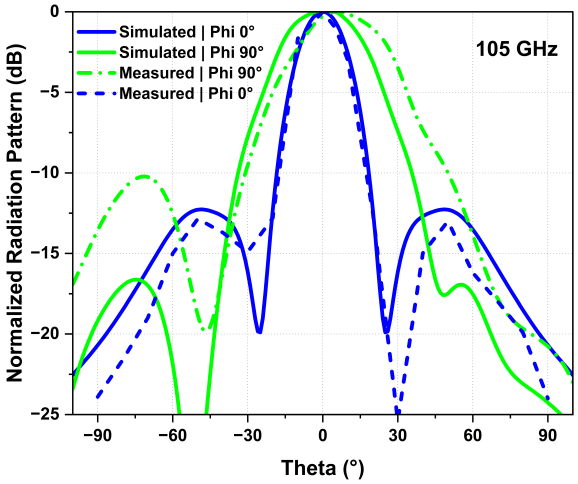

(b) Measured pattern in plane 90° and 0° at 105 GHz.

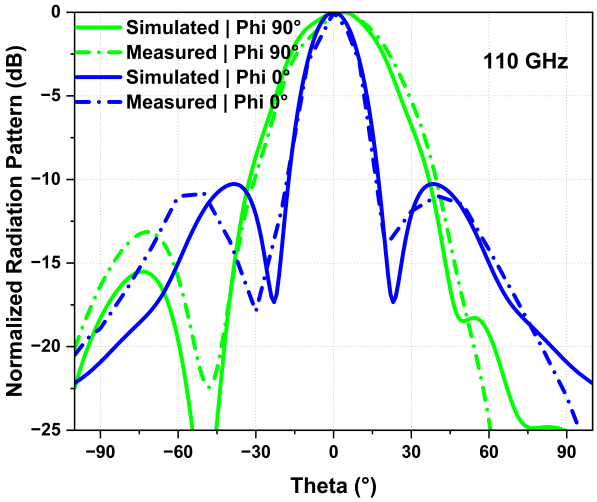

(c) Measured pattern in plane 90° and 0° at 110 GHz.

Figure 3.13: Radiation patterns at different frequency ranges from 100, 105, and 110 GHz in both the plane (90° and 0°).

For instance, the design in [74] achieves a marginally higher gain but at the cost of a larger physical footprint and narrower bandwidth. In contrast, the designs in [75], [73], and [76] exhibit lower gains. Particularly, [73] displays a gain fluctuation exceeding 2.5 dBi within the relevant frequency range, indicating inconsistent performance, which is suboptimal for applications requiring stable and high-quality communication.

Our hybrid parallel-series fed array stands out by integrating a low-profile form with high gain and wide bandwidth. Operating within the -10 dB impedance bandwidth of 100-110 GHz, it achieves a peak gain of 14.35 dBi (simulated) and 13.9 dBi (measured). Furthermore, the total efficiency exceeds 85%, with less than 1 dBi variation in gain across the specified frequency range. Its compact size $(5.2 \times 5.12 \times 0.127$ mm), along with its low-cost classification, makes it an attractive option for standalone antenna applications.

Table 3.4: Performance comparison of the proposed antenna with other related antennas in the literature.

Ref.	Antenna Type	-10 dB imp. BW (GHz)	Peak Gain (dBi) (Sim/Meas)	Efficiency (%)	Array size (mm)	Cost
[74]	Series fed array	99-101.5	15.82*	52	$12 \times 3.078 \times 0.150$	Low
[77]	Microstrip patch array	304-318	11.25	90	$0.706 \times 0.626 \times 1$	-
[78]	Series fed array	100	13.2*	-	$3.078 \times 2.4 \times 100$	Low
[79]	Microstrip patch array	213-0.240	16.2	-	$2.81 \times 2.54 \times 1$	-
[80]	SIW	194-196	12.2	86	$20 \times 13.5 \times 0.125$	-
[75]	Planar antenna array	350-385	8.15	65.71	$6 \times 6 \times 1$	-
[81]	Planar antenna array	75-110	16.9/5*	-	$7.8 \times 7.8 \times 0.69$	High
[80]	On-chip antenna	290-316	13.5/11.7*	≥ 55	$20 \times 3.5 \times 0.126$	High
[73]	Dipole antenna	95-102	≤ 4.8*	-	-	Medium
[82]	Series fed array	98-103	13.4/12.2*	94	$6.197 \times 3.386 \times 0.127$	Low
[76]	Off-chip antenna	137-158	8.6*	81	$12.3 \times 4.5 \times 0.905$	Low
This work	**Planar antenna array (single layer)**	**100-110**	**14.35/13.9***	≥ 85	$5.2 \times 5.12 \times 0.127$ ($1.82 \times 1.79 \times 0.044\ \lambda$ at 105 GHz)	Low

3.6 Summary

In this chapter, we propose a high-performance sub-THz antenna fabricated using low-cost PCB laser milling technology. The basic antenna design incorporates a quasi-slot integrated on a patch and is fed with a strip line. We have achieved an improved radiation pattern and higher antenna gain by modifying the radiation apertures. A 2×2 sub-THz antenna array was fabricated and tested, demonstrating a measured peak gain of 13.43 dBi at 105 GHz and a return loss of better than 10 dB across the 100-110 GHz frequency range. The antenna was then opti-

mized using machine learning-assisted global optimization techniques, which further improved the gain, bandwidth, and efficiency while minimizing the SLLs within the desired band. The proposed antenna boasts a simple feeding structure, low fabrication costs, wide bandwidth, and high gain, making it well-suited for THz sensing and imaging applications.

Chapter 4

Efficient and High Gain Sub-THz Series-fed Antenna Array

4.1 Introduction

This chapter comprehensively presents the design, analysis, and performance of the proposed wideband 5-element linear array and subsequent slot-integrated series-fed arrays with co-polarized parasitic patches. The addition of parasitic patches on the top conducting surface of the array enhances co-polarized currents, leading to increased gain without enlarging the antenna aperture. This design strategy prioritizes achieving high-performance metrics and simplicity in design geometry to lower costs and reduce fabrication complexities within the sub-THz operating range, which encompasses frequencies from 0.1 to 1 THz. This chapter delves into a detailed discussion of the methodologies employed in antenna design, alongside an in-depth analysis of performance metrics. Furthermore, it covers the practical aspects of fabrication and provides comprehensive measurement results. The primary objective here is to develop high-gain, compact sub-terahertz series-fed antenna arrays that strike an optimal balance between performance, simplicity, and cost-effectiveness. The series-fed approach is chosen because of its inherent benefits in enhancing antenna gain and directivity, minimizing feed network length, and significantly reducing ohmic and dielectric losses while simplifying the overall design, factors that are crucial for the effective operation and viability of antenna systems at sub-THz frequencies. This chapter aims to validate the feasibility of these design enhancements through both theoretical and empirical methodologies, paving the way for their application in next-generation wireless communication systems.

4.2 Design of Sub-THz Series-fed Antenna Array

Developing an efficient sub-THz series-fed antenna array involves rigorous design processes to ensure the specific design considerations and techniques employed to achieve a high-performing

antenna array suitable for sub-THz applications.

4.2.1 Design Methodology

The design of the proposed 5-element wideband linear antenna array is based on conventional patch antennas, which are inherently narrowband. Techniques to improve bandwidth include incorporating cuts/slots in the patch, adding parasitic patches, or using defective ground structures [83]. Another method involves increasing substrate thickness while reducing the quality factor to overcome the narrow bandwidth limitation. However, this approach can lead to drawbacks including increased surface waves, larger antenna dimensions, and higher losses. These consequences must be carefully considered when seeking to design a wide-band antenna array. In contrast to conventional patch antenna impedance matching approaches, the proposed antenna design avoids all of the aforementioned design complexities. The proposed solution introduced multiple resonances intentionally within the desired frequency band by employing a series-fed topology with multiple patch elements. As the RF signal propagates through the series array, the loading impedance of each patch element varies, leading to different resonant modes emerging in close spectral proximity. This strategic arrangement causes the resonant modes to converge, ultimately resulting in a wideband -10 dB impedance matching characteristic.

4.2.2 Practical Design Approach

The design evolution step for achieving a 5-element series-fed array with optimized dimensions is depicted in Figure 4.1. Initially, the dimensions of the microstrip patch element, specifically the width (W) and length (L), were calculated for operating frequency at 105 GHz. These calculations were based on the standard equations for patch antennas, as detailed in [49].

$$W = \frac{c}{2f_r}\sqrt{\frac{2}{\varepsilon_{eff}+1}} \tag{4.1}$$

$$L = \frac{c}{2f_r\sqrt{\varepsilon_{eff}}} - 2\Delta l \tag{4.2}$$

The effective permittivity and extended length were calculated as:

$$\varepsilon_{\text{eff}} = \frac{\varepsilon_r+1}{2} + \frac{\varepsilon_r-1}{2}\left[1+12\frac{h}{W}\right]^{-\frac{1}{2}} \tag{4.3}$$

$$\Delta L = 0.412h\frac{(\varepsilon_{\text{eff}}+0.3)\left(\frac{W}{h}+0.264\right)}{(\varepsilon_{\text{eff}}-0.258)\left(\frac{W}{h}+0.8\right)} \tag{4.4}$$

Here f_r = center operational frequency, c = speed of light, ε_r = relative permittivity of the

substrate, ε_{eff} = effective relative permittivity of the substrate, h = the thickness of the substrate, and ΔL = extended length of the patch that depends on width and height of the substrate.

A thin 0.127 mm low-loss Rogers RT/Duroid 5880 material was used as the substrate with a given dielectric constant of 2.2, a copper conductor layer of 18 μm, and a loss tangent of 0.001. Initially, a half-wavelength patch (with a length and width of 0.63 mm and 1.14 mm, respectively) operating at 100 GHz was designed. The full ground plane is used at the bottom of the substrate to achieve a broad-side radiation pattern. A 50 Ω feed line was used to excite the patch. However, a typical microstrip patch antenna faces a significant challenge in impedance matching due to its high intrinsic impedance, approximately 200 Ω, which deviates from the standard 50 Ω system impedance. To address this challenge, our approach included extending the patch width and adopting a series-fed array configuration. To achieve a wide impedance bandwidth and modify the radiation pattern, the design of the antenna integrates cross-slots, centrally positioned on the rectangular patch. This configuration ensures a uniform distribution of the electric field across the patch, thus enhancing the antenna's radiation characteristics while maintaining its compact form factor. The geometric design parameters of the antenna, as shown in Figure 4.1, have been carefully optimized with fabrication constraints, ensuring that the design is not only theoretically sound but also practically feasible for fabrication.

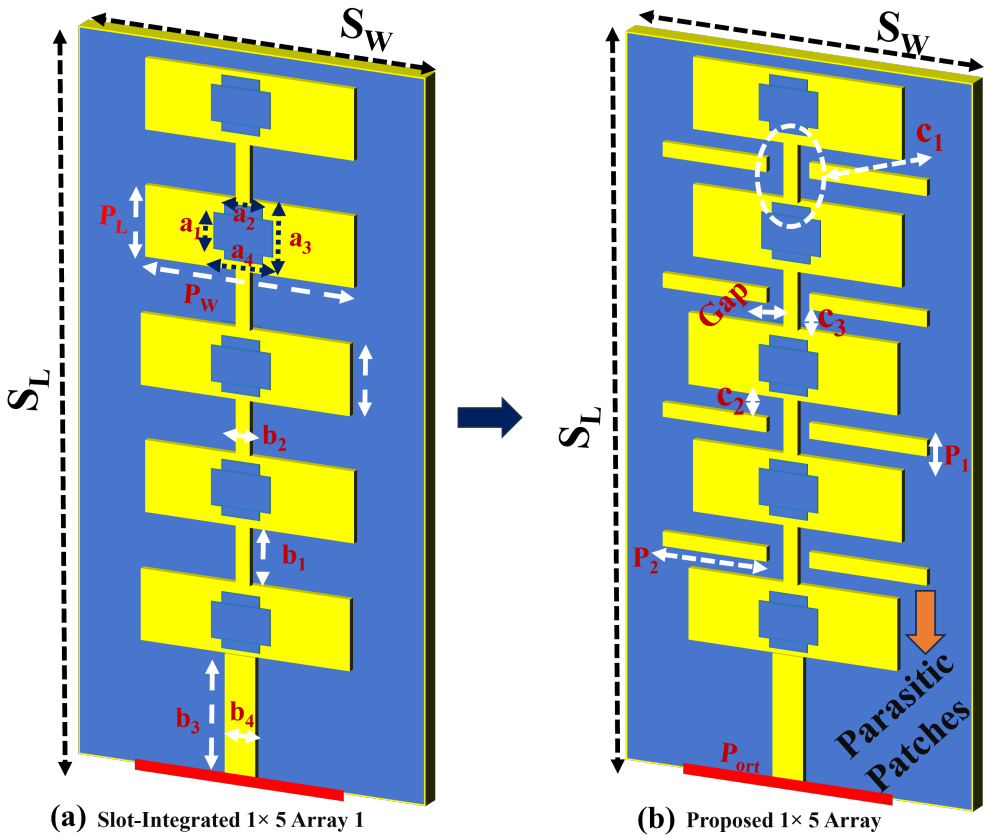

Figure 4.1: (a) Design evolution steps towards the proposed array (b) Proposed 1 × 5 array with parasitic patches.

4.3 Enhancing Performance with Slot-Integrated Arrays and Parasitic Patches

To meet the increasing demand for high-performance antenna systems in THz communication, various advanced techniques have been explored. One effective approach is the integration of slot elements and parasitic patches into antenna arrays. These design enhancements can significantly improve key performance metrics such as bandwidth, gain, and radiation efficiency.

4.3.1 Integration of Parasitic Patches for Improved Series-Feed Array Performance

Our design process begins with a baseline model—a linearly polarized, series-fed array without parasitic patches. As shown in Figure 4.1, this initial setup serves as a control for subsequent design enhancements. One of the primary advantages of utilizing a series feed is the elimination of power division networks, which are typically associated with spurious radiation that can degrade the system's overall performance.

The series feed configurations enhance the antenna's radiation efficiency by directly feeding each element in sequence, reducing losses commonly seen with other feeding techniques. However, to further push the performance boundaries, we explored integrating co-polarized parasitic patches into the antenna structure. The purpose of this addition is to increase gain and aperture efficiency without increasing the physical footprint of the array.

We developed an enhanced design by adding co-polarized parasitic patches directly to the antenna aperture, depicted in Figure 4.1(b). These parasitic patches are strategically added to the primary radiating element without increasing the overall size of the antenna. They function by re-radiating received energy in phase with the main radiator, effectively enhancing the main beam's strength and focus while minimizing side lobes. This approach of gain enhancement is particularly valuable as it avoids the typical trade-offs with antenna size, preserving the array's compactness which is crucial for sub-THz applications.

To demonstrate the effectiveness of this design change, we provide a comparison of performance metrics between the initial design without parasitic patches (Figure 4.1(a)) and the modified design Figure 4.1(b). This comparison clearly shows the improvements in bandwidth, gain, and radiation efficiency, substantiating the benefits of integrating parasitic patches into series-fed arrays.

4.3.2 Effective Integration and Testing

Moreover, the antenna also includes a 1-mm solderless connector to facilitate easy integration with measurement setups, avoiding the complications of soldering which could otherwise impact performance through heat damage or impedance mismatches. The design ensures minimal

reflection and optimal power transfer, managed through careful impedance matching:

$$Z_{\text{in}} = Z_0 \left(\frac{1+\Gamma}{1-\Gamma} \right) \tag{4.5}$$

where Z_{in} is the input impedance, Z_0 is the characteristic impedance of the line, and Γ is the reflection coefficient, ensuring minimal reflection and power transfer.

These enhancements are achieved through rigorous optimization, laying the foundation for subsequent simulation and fabrication phases, which are detailed elsewhere in this chapter.

4.3.3 Advantages of Co-polarized Parasitic Patches

The inclusion of co-polarized parasitic patches plays a crucial role in our antenna design, specifically enhancing its performance by increasing gain and reducing side lobes. These patches work by re-radiating captured energy in phase with the emission from the main radiator. This coherent re-radiation effectively enhances the main beam while suppressing energy dispersion in unwanted directions. The quantitative impact of these patches on the antenna's gain is expressed through the following equation:

$$G = 10\log_{10} \left(\frac{4\pi \text{Area}_{\text{eff}}}{\lambda^2} \right) \tag{4.6}$$

where $Area_{eff}$ represents the effective area of the antenna, which is increased by the additional radiating surface provided by the parasitic patches. This increase not only boosts the gain but also enhances the overall efficiency of the antenna. The equation assumes isotropic radiation conditions, suitable for theoretical evaluations in free space environments.

This integration leads to higher gain without compromising the antenna's compact size, crucial for sub-terahertz applications where maintaining robust performance in small form factors is challenging.

4.4 Antenna Optimization Using SADEA-I

The design of the proposed antenna must operate over a wide frequency range or bandwidth, and achieve high gain and efficiency which is particularly challenging for THz indoor wireless communication systems. These characteristics are essential for effective data transmission over short distances within indoor environments, ensuring a consistent and high-quality signal capable of overcoming typical indoor propagation challenges. To address these requirements, the Surrogate-Assisted Differential Evolution for Antenna Synthesis (SADEA-I) optimization technique is employed.

4.4.1 Antenna Parameterization for SADEA-I

Identifying parameters is the first step in any antenna design optimization procedure. The SADEA-I optimization process involves optimizing several parameters, such as patch length (PL), patch width, substrate height, and other geometry parameters listed in Table 4.1. These parameters significantly affect the antenna's performance, impacting bandwidth, gain, and efficiency, which are critical for robust communication in the specified sub-THz range.

To select these design variables, a detailed parametric study was conducted. This study involved systematically varying each parameter within a predefined range while keeping other parameters constant to observe their impact on key performance metrics. The ranges for each parameter were determined based on initial design specifications and empirical data from previous studies. For instance, the patch length (PL) was varied from 0.51 mm to 0.95 mm in 0.5 mm increments, and the resulting changes in bandwidth, gain, and efficiency were meticulously recorded and analyzed.

The selection of variables was guided by several critical factors. Sensitivity analysis was performed to identify parameters that exhibited high sensitivity to performance metrics. This prioritization ensures that the optimization process focuses on the most influential variables, thereby enhancing the antenna's overall performance. Additionally, parameters were chosen based on their ability to provide optimal trade-offs between competing performance metrics, such as bandwidth and gain, ensuring that improvements in one metric did not significantly degrade another. Practical considerations were also taken into account, with an emphasis on parameters that are feasible to fabricate and implement in real-world scenarios. For example, in the initial design (Figure 4.1(a)), the variable $[a_1, a_2, a_3, a_4]$ is limited to standard values (minimum width of 0.2 mm) because LPKF milling machines can achieve minimum trace widths of 200 micrometers (0.2 mm) for RF designs, ensuring the practical applicability of the optimized designs.

Initially, local optimizers such as the Trust Region Framework (TRF) in CST Microwave Studio were employed, but the results were far from satisfactory; although the specifications for bore-sight gain and total efficiency were met, the max($|S_{11}|$) is poor (i.e., about -7.5 dB). Moreover existing global optimizers, such as particle swarm optimization (PSO), were estimated to require prohibitively long durations without a guarantee of success [64] [69] [72]. Consequently, as detailed in Chapter 2, the state-of-the-art method known as Surrogate Assisted Differential Evolution for Antenna Synthesis (SADEA-I) was utilized to obtain an optimal design [64], [84]. The initial phase involved the design shown in Figure 4.1(a), with variables detailed in Table 4.1. The goal is to minimize the fitness function F_{mpa} as described in Equation (4.7), ensuring the antenna achieves the performance targets outlined in Table 4.1. Although the overall antenna size is not explicitly defined in Equation (4.7), the design considerations ensure optimal performance. The selected search ranges and geometric constraints are intentionally set to achieve a compact and low-profile design.

$$F_{mpa} = \max(|S_{11}|) + w \cdot \max([12\,\text{dBi} - G_{min}, 0]) + w \cdot \max([0.70 - \eta_{min}, 0]) \quad (4.7)$$

In this context, the worst-case performances of $|S_{11}|$, bore-sight gain, and total efficiency at various frequencies are considered. Here, w represents the penalty coefficient, empirically set to 50 [59]. Instead of employing a weighted sum of the three performance metrics, which complicates their balancing, specific targets are established for bore-sight gain and total efficiency. This method ensures that any deviations from the bore-sight gain and total efficiency requirements, denoted by G_{min} and η_{min}, incur substantial penalties, thereby prioritizing these factors in the optimization process. After 50 hours of optimization, SADEA-I obtains the optimal design in Table 4.1 with the performance shown in Table 4.2. It can be seen that all the specifications are satisfied.

After performing 450 electromagnetic (EM) simulations, the design met the required specifications within a cumulative design time of roughly 10.5 hours. It can be seen that all the specifications are satisfied. The physical implementation is shown in Figure 4.8 and the overall dimension is $5\,\text{mm} \times 5\,\text{mm} \times 0.127\,\text{mm}$, which corresponds to $4.725\,\lambda_0 \times 1.75\,\lambda_0 \times 0.044\lambda_0$ (where λ_0 is the free space wavelength at 105 GHz). The SADEA-I-optimized design frequency response is depicted in Figure 4.2 to Figure 4.5.

Table 4.1: Search ranges and dimensions of the SADEA-I optimum for the proposed (All the dimensions in mm)

No	Parameters	Array 1		Proposed Array		SADEA-I optimum
		Lower Bounds	Upper Bounds	Lower Bounds	Upper Bounds	
1	P_L	0.512	0.95	-	-	0.63
2	P_W	1.61	3.5	-	-	1.14
3	a_1	1.23	3.00	-	-	0.21
4	a_2	0.21	0.32	-	-	0.24
5	a_3	0.20	0.35	-	-	0.39
6	a_4	0.20	0.32	-	-	0.48
7	b_1	0.40	0.75	0.30	0.90	0.80
8	b_2	0.12	0.25	0.15	0.30	0.23
9	b_3	1.23	3.00	1.23	9.00	1.81
10	b_4	-	-	0.30	0.50	0.45
11	G_{ap1}	-	-	0.10	0.30	0.25
12	P_1	-	-	0.15	0.40	0.22
13	P_2	-	-	0.10	0.95	0.93
14	C_1	-	-	0.50	0.85	0.70
15	C_2	-	-	C_3	0.22	0.18
16	C_3	-	-	$\geq a_4$	0.22	0.15
17	P_{ort}	-	-	6	10	7.5
18	$S_L = 5 \times P_1 + (2 \times b_3) + b_4 + 7.5$					12.50
19	$Sw = P_W + (3 \times b_4) + 4 \times P_2 \times (4 \times C_3) + 5.25$					10.53

Table 4.2: Performance specification for the proposed antenna array (95-110 GHz)

No	Item	Specifications	SADEA-I Optimum
1	Maximum return loss (S11)	≤ -10 dB	-11.4 dB
2	Minimum bore-sight gain (Gmin)	≥ 12 dBi	12.3 dBi
3	Minimum Total Efficiency	$\geq 70\%$	82.5%

4.5 Simulated Results of the Proposed 1 × 5 linear Array:

The proposed 1×5 linear array was subjected to extensive simulations to evaluate its performance. The results demonstrate the effectiveness of the design in achieving desired performance metrics, essential for advanced THz communication systems. Key parameters such as bandwidth and gain were carefully analyzed to understand the array's capabilities and limitations.

4.5.1 Bandwidth and Gain

The optimized reflection coefficient (-10 dB impedance bandwidth) of the proposed 1×5 linear array is shown in Figure 4.2. The array provides a -10 dB impedance bandwidth of 20 GHz, spanning from 94 to 110 GHz. However, our primary interest lies within the 100-110 GHz range. Consequently, subsequent results and discussions will focus exclusively on this frequency band.

Figure 4.3 illustrates the realized gain of different design evaluation steps across the operational frequency range. The three configurations compared are: Slots-integrated Patch Element, Array without Parasitic Patches, and Array with Parasitic Patches. It is evident that the inclusion of parasitic patches significantly enhances the realized gain.

The peak realized gain of the proposed antenna array with parasitic patches reaches approximately 16.50 dBi at 106.50 GHz, as shown in Figure 4.3. This configuration demonstrates high performance compared to the array without parasitic patches and the slots-integrated patch element, which have lower gains.

The gain fluctuation across the 100-110 GHz band is less than 0.90 dB, indicating stable performance within our band of interest. The addition of parasitic patches not only improves the peak gain but also ensures a more consistent gain across the desired frequency range.

These results underscore the effectiveness of incorporating parasitic patches into the antenna design, leading to enhanced performance in terms of realized gain and maintaining stability over the operational bandwidth. This makes the proposed antenna array a suitable candidate for applications requiring high efficiency and stable gain in the 100-110 GHz frequency range.

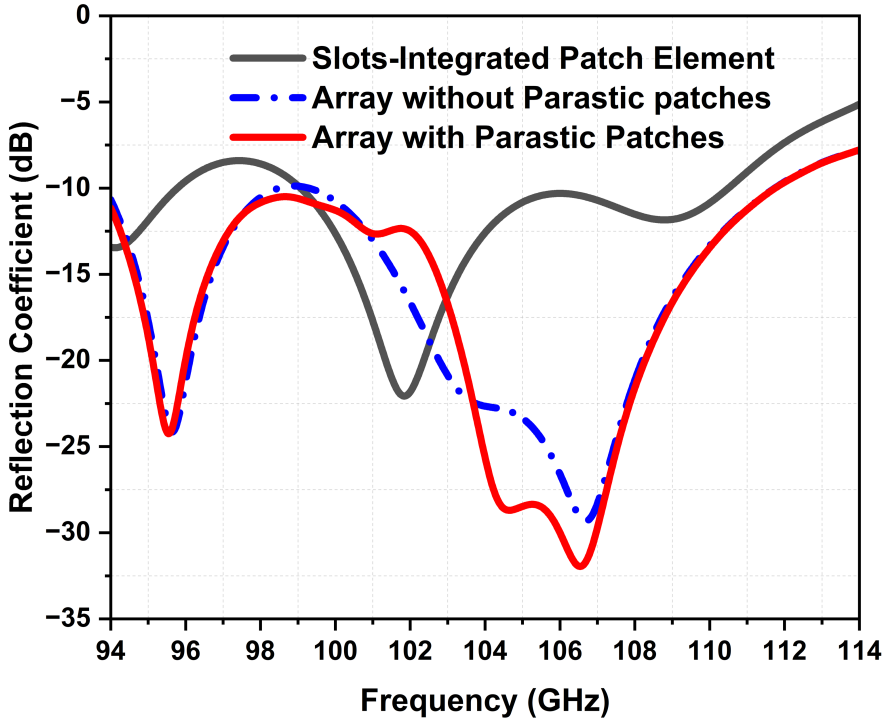

Figure 4.2: Simulated reflection coefficient of different design evaluation steps.

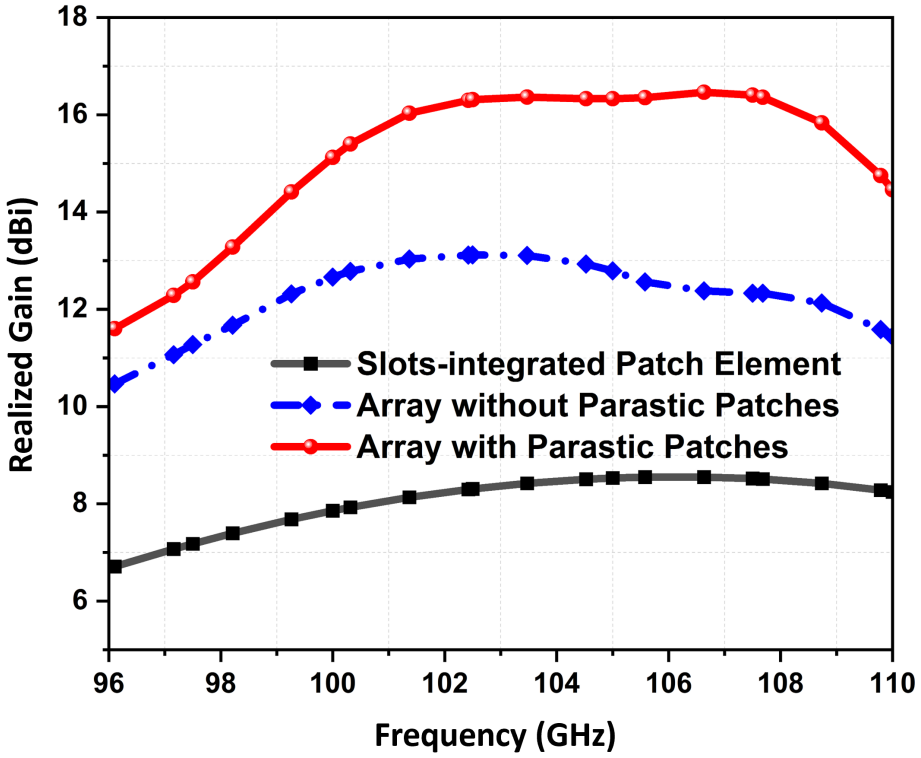

Figure 4.3: Realized gain of different design evaluation steps.

4.5.2 Efficiency

Further insights into the efficiency of the antenna system are gleaned from Figure 4.4, which illustrates radiation efficiency across various antenna configurations. The baseline configura-

tion, represented by the slots-integrated patch element, sets a foundation for comparison. When parasitic patches are omitted, the radiation efficiency experiences a dip, as indicated. However, the incorporation of parasitic patches enhances the efficiency, especially in the mid-band frequencies around 102-106 GHz. The radiation efficiency is over 92.4%. The design achieves a significant increase in aperture efficiency from 9.18% to 20.47%, while maintaining the same antenna array size. Moreover, the aperture efficiency, which was calculated from the following equation:

$$A_{\text{aperture}} = \frac{A_{\text{em}}}{A_p} = \frac{G_0 \lambda_0^2}{4\pi A_p} \tag{4.8}$$

where A_p is the physical area of the antenna array and A_{em} is the maximum effective area of the proposed antenna. λ_0 and G_0 denote the free-space wavelength and peak gain of the antenna. The aperture efficiency is increased by adding parasitic patches because the gain is increased while maintaining the same antenna area as shown in Figure 4.1(b).

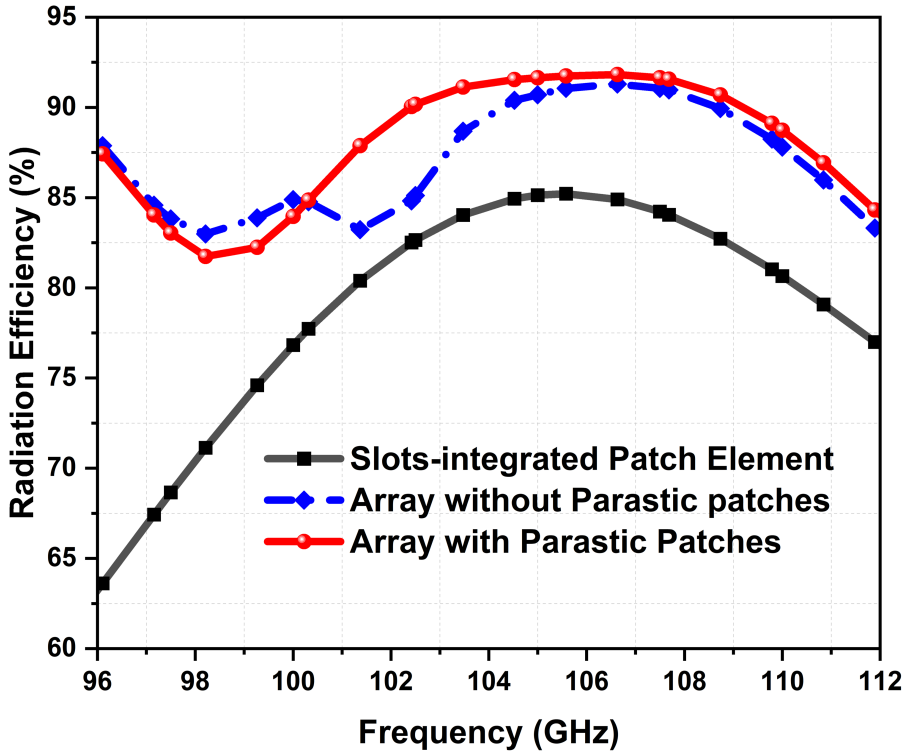

Figure 4.4: Total efficiency of the different design evaluation steps

4.5.3 Radiation Pattern

The radiation characteristics of the proposed antenna array were thoroughly analyzed within the 100-110 GHz sub-THz band. The 3D radiation pattern at various frequency points is illustrated in Figure 4.5, revealing a fan-shaped pattern in the x-z plane (Phi 0°). The 2D patterns in the

x-z plane, shown in Figure 4.6(a), exhibit a half-power beam width (HPBW) ranging from 52° to 68°. In contrast, the y-z plane (Phi 90°) patterns in Figure 4.6(b) display a more constrained HPBW, spanning 22° to 26°. These beam width variations are due to the linear configuration of the array, which narrows the radiation pattern along the element axis while expanding it orthogonally.

At 110 GHz, the array predominantly radiated in the broadside direction. Moreover, throughout the entire frequency band, the side-lobe levels (SLLs) consistently remained below -10 dB in both planes, indicating efficient pattern control. Additionally, the E-field distribution across different operating frequency points, demonstrated in Figure 4.7, shows strong field strength across the aperture over a wide band.

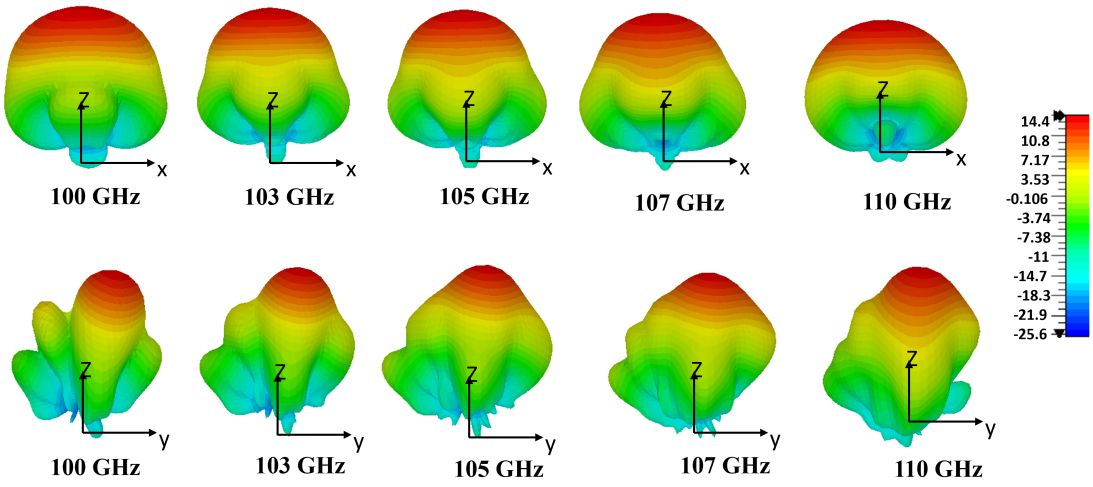

Figure 4.5: 3D simulated radaition pattern of the propsed 1×5 array in 100-110 GHz diffent angular veiw

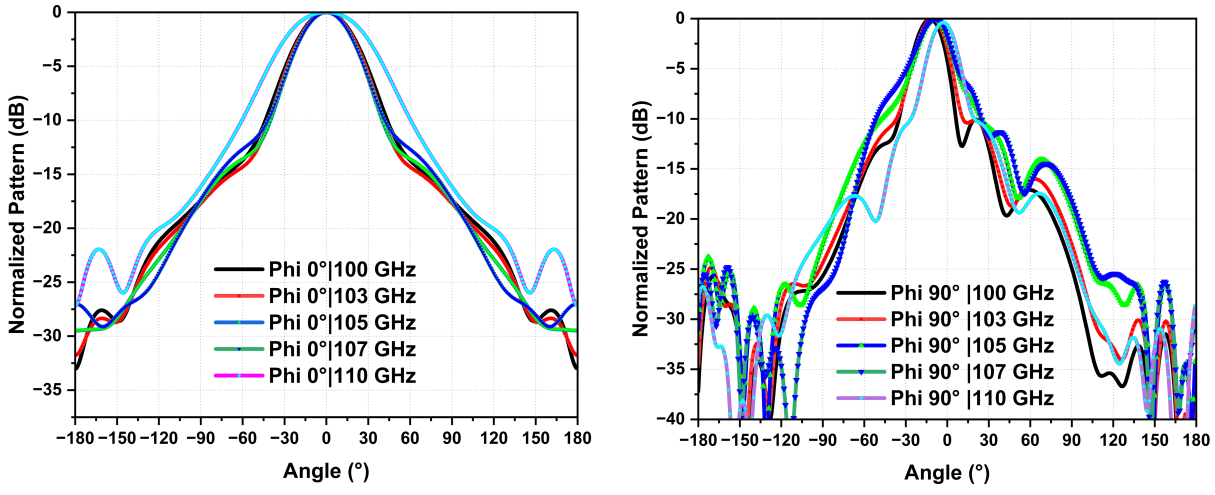

(a) (b)

Figure 4.6: 2D rectangular plot of simulated radiation pattern of the proposed 1×5 array across 100-110 GHz. (a) H-plane (b) E-Plane.

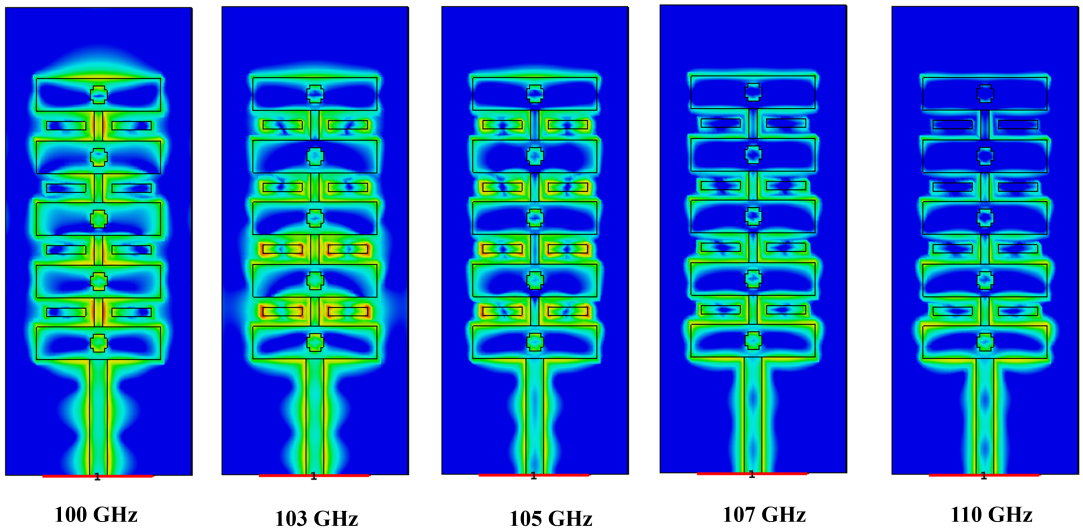

Figure 4.7: E-field distribution of the proposed 1×5 array across 100-110 GHz

Table 4.3: Performance comparison of sub-THz antenna array designs

Comparison Parameter	**Array 1**	**Proposed Array**	**Improvement**
Return Loss (dB)	-25 dB (106.5 GHz)	-32.5 dB (106 GHz)	-7 dB
Measured Return Loss	-	100-110 GHz	-
Bandwidth	15 GHz	15 GHz	-
Peak Realized Gain	12.91 dBi (variation $>$ 2 dBi)	16.50 dBi (variation $<$ 0.90 dBi)	3.59 dBi
Peak Total Efficiency	88.12%	90.15%	2.03%
Aperture Efficiency	9.18%	20.47%	11.29%
Size in mm	12.50 mm $\times$ 5 mm $\times$ 0.127	12.50 mm $\times$ 5 mm $\times$ 0.127	-

4.6 Prototype Fabrication and Measurements

To validate the design and performance of the proposed antenna array, a prototype was fabricated and subjected to comprehensive measurements. This section details the fabrication process, the materials used, and the techniques employed to construct the prototype, followed by the measurement setup and results. Additionally, the impact of fabrication tolerances on the performance of sub-THz antenna designs is discussed to highlight potential challenges in the fabrication process.

4.6.1 Fabrication Process

The prototype of the proposed 1×5 series-fed arrays with co-polarized parasitic patches is shown in Figure 4.8. The dimensions of the 1×5 array are $5\,\text{mm}(4.725\lambda) \times 5\,\text{mm}(1.75\lambda) \times 0.127\,\text{mm}(0.044\lambda)$, where λ is the free space wavelength at 105 GHz. Fabrication was performed using the LPKF ProMat S103 milling machine at the University of Glasgow. To ensure mode-free performance within the sub-THz frequency range, a 1 mm standard solderless connector was utilized for the feed. Given the challenges associated with soldering at such high frequencies, including potential excess loss and alterations in resonance frequencies if not executed flawlessly, solderless connectors offer a preferable solution for practical measurement.

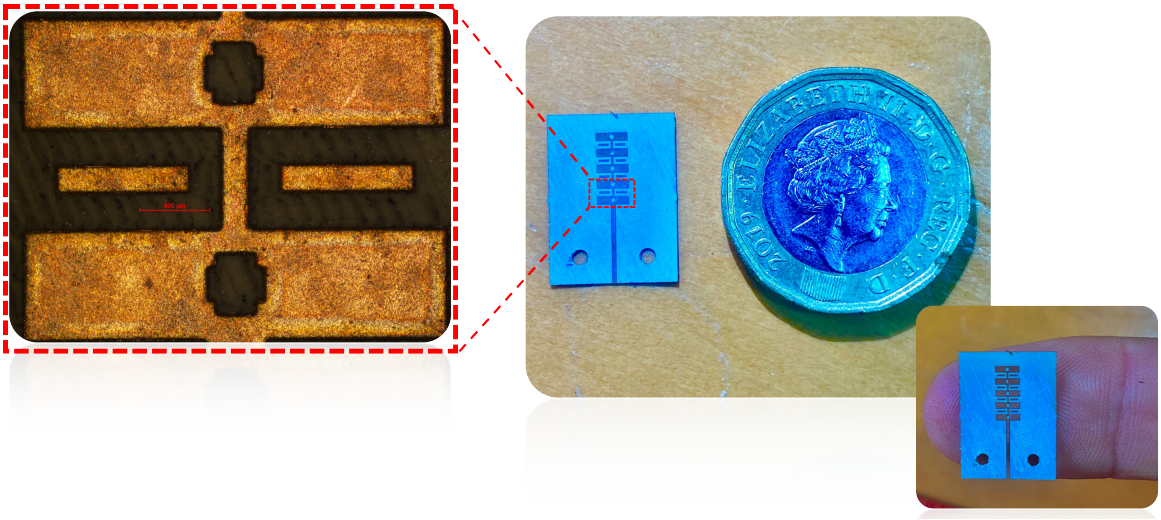

Figure 4.8: Fabricated Prototype of the 5-Element Series-Fed Antenna Array with Integrated Co-Polarized Parasitic Patches, shown with a one-pound coin for scale comparison.

4.6.2 Measurement of Antenna Performance

The measurement setup was arranged in an open space within an indoor laboratory environment to measure the reflection coefficient. This setup involved the integration of the N5260A millimeter head controller connected to an E8361A Vector Network Analyzer (VNA), covering a frequency range from 10 MHz to 67 GHz. To extend the VNA's capabilities to higher frequencies, the N5260A was employed to upconvert the VNA output to 110 GHz, ensuring heightened accuracy and reliability of measurements. The configuration is illustrated in Figure 4.9, where the fabricated antenna is interfaced with the millimeter head controller via a 1-mm connector.

Moreover, the measured operational frequency band ranges from 100 to 110 GHz. Both simulated and measured results are depicted in Figure 4.10, illustrating a close agreement between the measured S-parameter and the simulated counterpart. Consequently, the simulated and measured -10 dB impedance bandwidths span from 100 to 110 GHz, denoting a fractional bandwidth of 9.52%, as shown in Figure 4.10. A slight difference in the resonance frequency

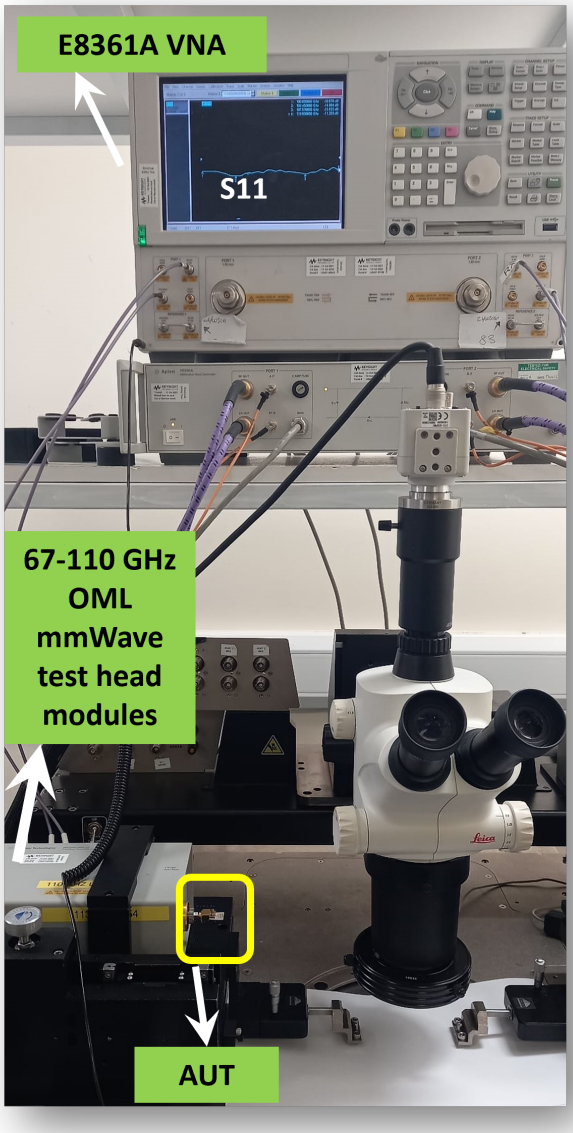

Figure 4.9: Measured (S_{11}) of the proposed array along with using (OML mmWave test-head module).

between the measured and simulated S-parameters can be attributed to fabrication tolerances or environmental factors.

4.6.3 Impact of Fabrication Tolerance on Sub-THz Antenna Design

As antenna structures are increasingly miniaturized for sub-THz frequencies, the impact of fabrication tolerances becomes more pronounced. Slight deviations in dimensions can significantly affect the antenna's resonance characteristics, impedance matching, and bandwidth. This is clearly illustrated in the magnified image of the fabricated prototype shown in Figure 4.11. For instance, in simulations, the microstrip transmission lines and patches are designed with ideal

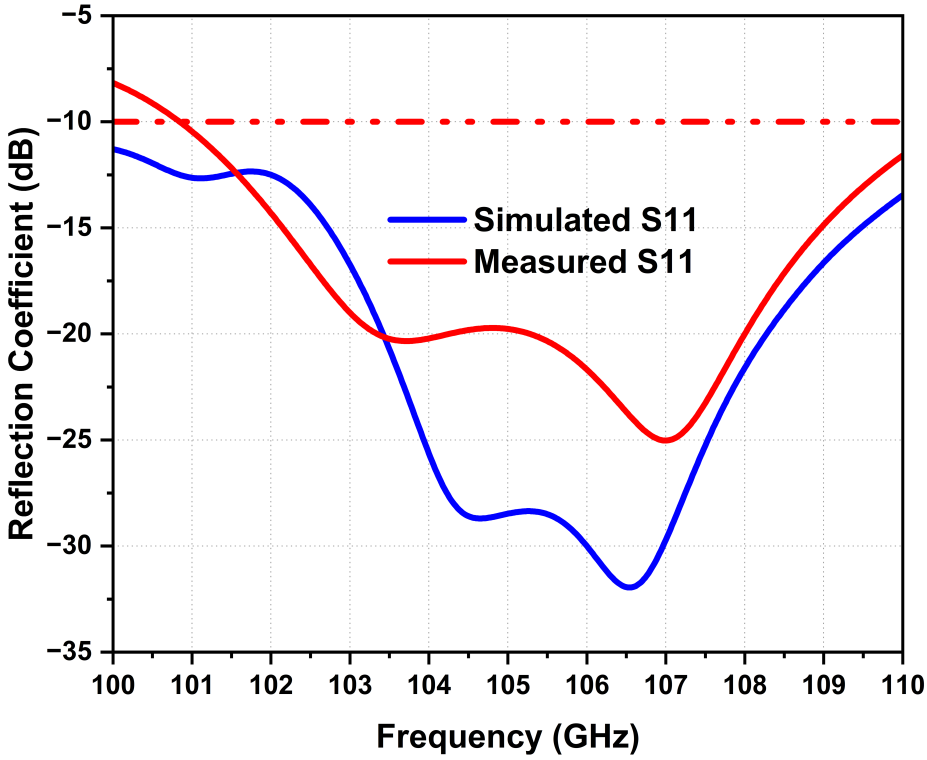

Figure 4.10: Measured S_{11} of the proposed array.

90° corners; however, the fabricated prototype exhibits rounded or bent corners in the microstrip transmission lines and patches, as highlighted by the yellow circles in the Figure 4.11. The copper surface also appears non-uniform rather than smooth. These fabrication tolerances can degrade antenna performance, as evidenced by deviations in the measured $|S_{11}|$ parameter, which is depicted in Figure 4.10. Furthermore, the precise alignment of the RF connector pin—having a tiny diameter of 0.05 mm—is crucial, as it must accurately contact the microstrip feed line. Any misalignment can lead to suboptimal performance, preventing the achievement of desired results.

4.6.4 Comparison with State-of-the-Art Antenna Designs:

The performance of our proposed antenna array is evaluated against other closely related designs in the sub-THz band, as detailed in Table 4.4. This evaluation reveals that our design surpasses several competing arrays in key performance metrics. Specifically, it demonstrates a wider impedance bandwidth and consistently high gain, all while maintaining a compact form factor. These enhancements highlight the superior performance and efficiency of our antenna design, making it ideal for applications where space and signal integrity are critical.

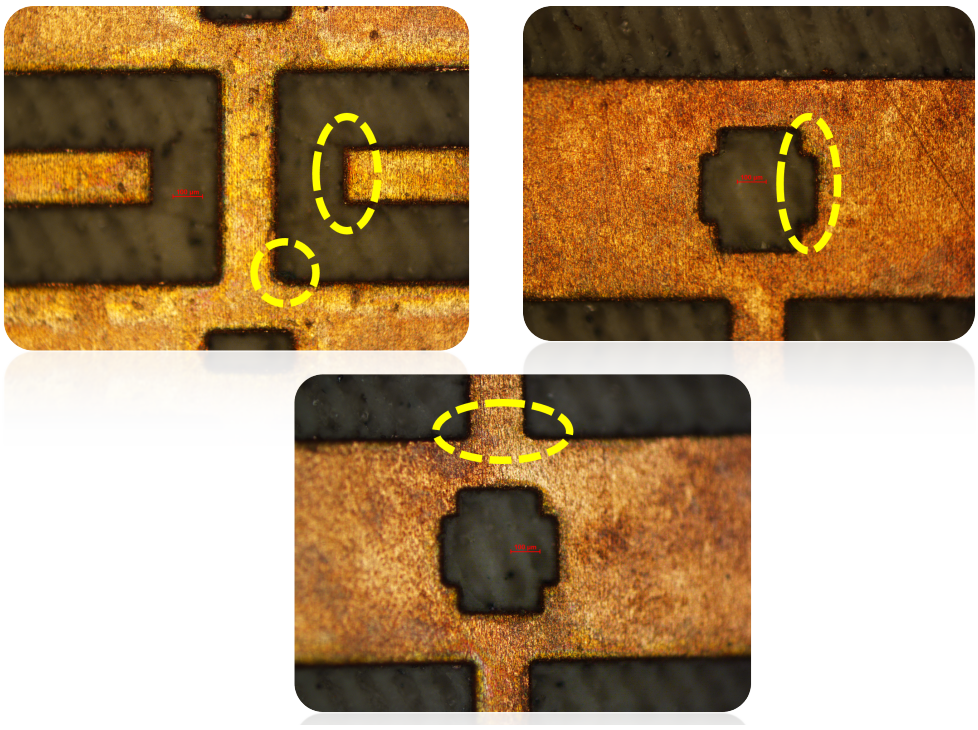

Figure 4.11: Practical demonstration of the fabrication tolerance.

Table 4.4: Performance comparison of the proposed THz antenna array with the literature

Ref No	**Array Geometry**	**-10 dB Impedance Bandwidth (GHz)**	**Peak Gain (dBi)**	**Efficiency (%)**
[13]	Planar antenna array	305-318	7.35	90
[78]	Single layer PCB microstrip patch array	99-101.5	15.2	50
[15]	Parallel series fed array microstrip patch array	112-135	5	-
[85]	L-probe differential fed patch	100–125	9.8	-
[86]	8 × 8 slot substrate integrated	130-145	20.5	59.2
[87]	Substrate integrated waveguide (SIW) array	130.2-158.8	16.3	55
[88]	Microstrip mesh array	90-95.5	13.3	-
[89]	Dielectric Resonator Antenna	100-110	9	80
This Work	**Series-fed linear array with co-polarized parasitic patches**	**95-110**	**16.50**	**92.4**

4.7 Summary

This chapter has presented a comprehensive design and analysis of a high-gain, efficient sub-terahertz series-fed antenna array tailored for sub-THz. This approach leverages the integration

of co-polarized parasitic patches and a series-fed configuration to enhance performance metrics such as gain and radiation efficiency while maintaining a compact and cost-effective design. The design methodology detailed in this chapter began with the theoretical foundations of antenna array physics, progressing through a rigorous optimization process using the SADEA-I algorithm. This approach not only optimized the geometric parameters of the antenna array but also ensured that the design met stringent performance specifications required for THz indoor wireless communication applications. The optimized design achieved a noteworthy gain of 16.50 dBi and maintained excellent radiation efficiency across the operational band of 95-110 GHz. Significantly, the integration of co-polarized parasitic patches played a pivotal role in augmenting the array's directivity and reducing side lobes, which are crucial for minimizing interference and enhancing signal clarity in dense communication environments. The simulated and prototype measurement results have shown close agreement, affirming the design's practical viability and effectiveness.

Chapter 5

Ultrawide-band Terahertz Flexible Antenna Arrays

5.1 Introduction

In the context of terahertz communications, previously highlighted complexities continue to challenge the design and fabrication of effective THz antennas. This chapter builds on these foundational concepts, introducing micro-fabricated THz antenna arrays designed to me the stringent requirements of 6G wireless communication by enhancing bandwidth, gain, and efficiency. The design of these arrays employs coplanar waveguide (CPW) feed techniques, which simplify the micro-fabrication process by improving antenna integration through enhanced impedance matching and reduced transmission losses. techniques discussed in Chapter 2, which involve adding structure or shape modifications to improve gain and bandwidth, often increase the design complexities of the THz antenna. As a result, achieving optimal performance can be challenging.

Addressing these complexities, the use of artificial intelligence (AI) techniques in antenna design has become increasingly prevalent. In this chapter, we explore the potential of AI to streamline antenna design through the use of AI-driven antenna design optimization algorithms, specifically SADEA-I and self-adaptive Bayesian neural networks surrogate model-assisted differential evolution for antenna optimization (SB-SADEA). This method, the latest instalment in the SADEA series, aims to reduce complexities while fully exploring the full potential of the antenna structure. The optimized antenna prototype, fabricated on a flexible substrate with a gold layer for radiation, demonstrates the advantages of precise fabrication and measurement processes essential for THz communications. This flexibility potentially revolutionizes antenna deployment in diverse environments, aligning with the scalability and adaptability requirements of future wireless networks.

5.2 THz Antenna Design Consideration

The design of antennas for THz applications involves unique challenges and requirements due to the high frequencies and short wavelengths involved. These considerations are crucial for developing efficient and high-performance THz antennas. This section delves into various aspects of THz antenna design, starting with an overview of different antenna topologies and their specific design methodologies.

5.2.1 Antenna Topologies and Their Design

THz technologies, known for their high spectral resolution, have found applications across various domains, including THz imaging and sensing [90], biomedical science [91], military, and environmental monitoring [92]. The antenna plays a vital role in the success of wireless communication and due to this; one of the thrust areas of the research in THz communication is the antenna system. Several antenna topologies have been used in the THz range for various applications [93]. For example, Yagi-Uda [94], bow tie, on-chip antennas [95], printed dipole antennas [96], metamaterial-based antennas, and wideband horn antennas [97]. Similarly, a nanoantenna array was also developed for subwavelength focusing of THz waves [98]. A theoretical analysis of a highly directed antenna array having 16 elements at 0.3 THz was shown in [95] with a maximum directivity of 18.1 dBi. In [99] a corporate feed antenna array with slot radiators and a layer of polarizing patches is designed to operate at 350 GHz. A UWB antenna covering the lower THz band is designed and numerically analyzed [100]. Similarly, a 3.2 THz array of patch antenna micro-cavities connected by narrow plasmonic wires presented in [101] demonstrates THz lasers made of arrays of 10×10 patch antenna micro-cavities. However, the size and structural complexities of the device become a great issue at the THz frequency. The limitations of material and fabrication capability at this small size limited the consideration of new antenna geometry with new techniques.

5.2.2 Integration of Corporate Feed Network and Slot Radiator

However, for communication purposes, due to integrating capability and low loss, the horn and the planar antenna have been recommended. In most of the recent developments, the horn antennas have been used to achieve high gain. However, this kind of antenna suffers from phase error and is not compact. The other option is the planar microstrip antenna, which is inherently limited by its gain and bandwidth despite good integration capability, and relatively simple fabrication through conventional techniques and compact size [46]. In addition to this, the feeding of the microstrip antenna array includes serial feeding, parallel feeding through corporate feed, spatial combiners, reflect arrays, and lens antennas [102]. The first two approaches, serial, and corporate feeding are often preferred for their simplicity, as they can be implemented on the

same substrate layer as the array itself, allowing for greater optimization of antenna weight, thickness, and cost. Furthermore, they are easier to fabricate at the nano and micro scale. Other feeding methods require more complex three-dimensional structures.

5.3 Practical Design of THz Antennas

The proposed 1×4 antenna array is characterized by a coplanar waveguide (CPW) transition that efficiently splits the signal into multiple ports, with each port terminated with uniformly optimized radiating patches as shown in Figure 5.1. The design was modeled using a full-wave commercial electromagnetic solver, CST Studio Suite 2023, with a maximum cell density of 20 cells per wavelength (approximately $4,370,800$ hexahedral mesh cells). The radiating elements of the array are gold-based and are implemented on a flexible polyamide substrate, notable for its low-loss and high-performance characteristics, which has a dielectric constant of 3.5 and $\tan\delta = 0.0025$ [103], [104], with a thickness of 124 μm (the thinnest thickness available in the market). Each patch incorporates a triangular slot, symmetrically etched on either side of the patch, making it the basic radiator due to its planar geometry and low profile. Integration of these triangular slots plays an essential role in improving the performance of the antenna array. Specifically, these slots contribute to improved impedance matching and reduced surface wave propagation. Consequently, these modifications result in an expanding bandwidth and an increase in both gain and radiation efficiency.

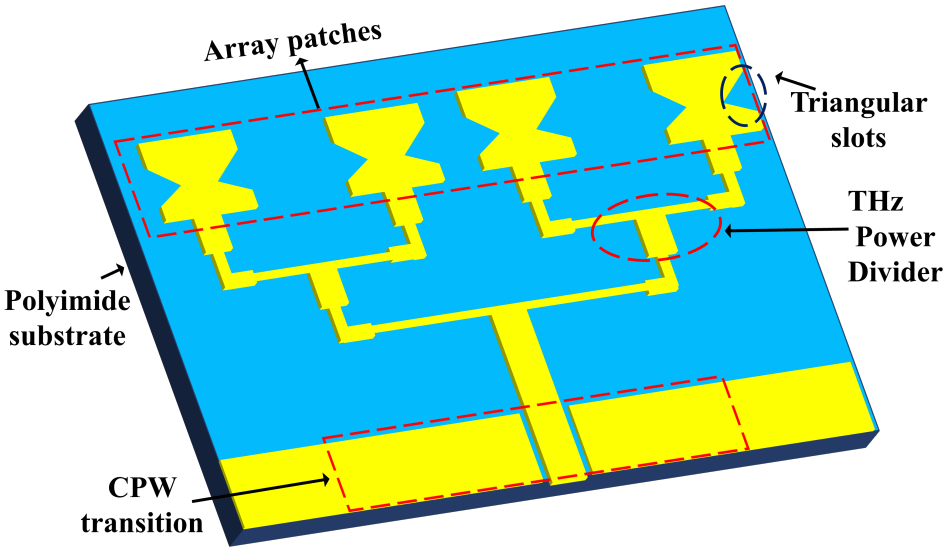

Figure 5.1: Geometry and dimensions of the proposed antenna array.

The feeding mechanism for each modified microstrip patch is optimized for a 50 Ω microstrip line, ensuring proper impedance matching and minimal signal loss. The gold-based radiating patch is chosen for its excellent conductivity and corrosion resistance, which are crucial for maintaining stable performance over time. The low-loss polyamide substrate provides

strong mechanical support while minimizing signal attenuation, allowing for high-quality transmission. The substrate ensures a compact and lightweight design.

Several techniques have been suggested and studied in the literature [105] to control the surface current distribution. Amongst these techniques, slot etching on the radiating patch has been well demonstrated to be more effective and efficient. The slots on the radiating patch change the current path; thus, generating higher-order current modes. This development has resulted in significant changes in the antenna characteristics, which leads to a reduction in the side lobes level, gain increment, and correction of the squint effect, thereby providing more improvement in the radiation characteristics. As a result, the geometry of the slot affects the surface current distribution. Moreover, it has two uniform rectangular planes with dimensions L_g and W_g, which are abreast and separated by the microstrip line. The uniform rectangular planes are both truncated and act as a coplanar waveguide (CPW). The optimized dimensions of the proposed antenna array are presented in Table. 5.1.

For the array design, the spacing between consecutive antenna elements was optimized to be 202 μm ($0.43\lambda_g$ or $0.35\lambda_0$, where λ_g and λ_0 are the guided and free space wavelengths, respectively, at 0.85 THz) to avoid radiation known as grating lobes in other directions than the broadside direction. In this work, triangular slot patches are excited using a corporate feed network, which involves three T-junction power splitters based on transmission line theory to obtain the precise magnitude and phase distribution for each antenna. In addition, the corporate feed was designed in a way that it inserts signals which are of the same magnitude and phase to each antenna to create a broadside radiation pattern. The input impedance of the antenna was aimed to be 50Ω and since the power splitting was done in parallel, the characteristic impedance of the transmission line was 100Ω. Hence $\lambda/4$ impedance transformer with 70.7Ω characteristic impedance was used with an optimized width of 35μm to convert back to 50Ω. The array is symmetric around the y-axis. The final critical dimensional parameters to construct a high-performance array topology are depicted in Figure 5.2.

5.4 Antenna Optimization Using SADEA-I

The proposed antenna design, as mentioned above, is particularly challenging because THz antennas require compactness while maintaining high gain and with the directional beam [6]. Consequently, AI-driven antenna design techniques [68] [65] are employed to optimize the antenna gain and efficiency, to meet the stringent requirements of THz communication. In the optimization process, a total of 16 design parameters were selected, considering their geometric constraints and respective search ranges as detailed in Table 5.1. These parameters were meticulously chosen to ensure they collectively satisfy the specifications outlined in Table 5.2. This selection is pivotal to achieving the desired antenna performance, encompassing factors such as size, gain, and efficiency within the THz frequency band. To ensure the patch, CPW ground

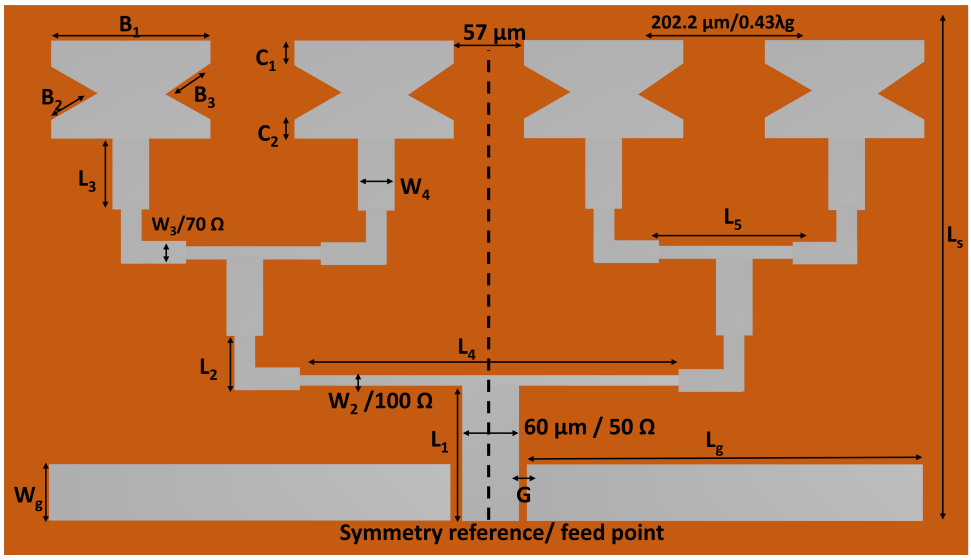

Figure 5.2: The geometry and dimensions of the triangular slots patch antenna array and the feeding network.

planes and waveguide port of the antenna array remain on the substrate during optimization, specific geometric constraints are enforced. For instance, during the optimization process, the microstrip line length is 210 μm and the partial ground plane length Lg cannot be greater than L_1. Thus, there is a single objective function and two constraints, as shown in the following expression:

$$\begin{aligned} \text{minimize} \quad & \max S_{11}(0.70 \text{ to } 0.95 \text{ THz}) \\ \text{subject to:} \quad & \text{min total efficiency} \geq 70\% \\ & \text{min realized Gain} \geq 6 \text{ dBi} \end{aligned}$$

$$F_{\text{mpa}} = \max(|S_{11}|) + w \times \max([7 \text{ dBi} - G_{\text{min}}], 0) + w \times \max([0.70 - \eta_{\text{min}}], 0) \tag{5.1}$$

Here, w denotes the penalty coefficient, preset to a value of 50 [22]. This setting ensures that violations of boresight gain and total efficiency specifications, denoted by G_{min} and minimum inband total efficiency (η_{min}), are significantly penalized, prioritizing these aspects in the optimization process. The focus initially lies on the specifications for gain and total radiation efficiency, subsequently prioritizing the S_{11} requirement. Clearly, modern optimization techniques are needed. Trust region framework with empirically determined initial designs and particle swarm optimization in CST-MWS was first employed, but they all failed to obtain design solutions which meet the specifications. After 550 EM simulations, costing about 42 hours, SADEA- I converged to obtain the optimal design variable (with a triangular slot configuration) in Table 5.1 with the performance shown in Table 5.2, it can be seen that all the specifications are satisfied.

Table 5.1: Search ranges and dimensions of the SADEA-I optimum for the proposed antenna array (All the Dimension in μm)

No	Parameters	Lower Bounds	Upper Bound	SADEA-I Optimum
1	B1	100	150	145
2	B2	15	40	36
3	B3	10	35	32
4	C1	12	30	27.50
5	C2	10.50	22.50	17.61
6	L1	10	300	210
7	L2	15	40	35
8	L3	40	100	80
9	L4	260	350	315
10	L5	60	120	105
11	Wg	20	150	54.5
12	W2	3	12	8
13	W3	2.5	15	12
14	W4	15	45	35
15	G	2	5	2.5
16	Pw	6	10	8.56
17	$W_{\text{ge}} = (S_{\text{w}} - (2 \times G) - L_5) + 5\mu m$			

Table 5.2: Performance specifications for the proposed antenna array

Item	Specification	SADEA-I Optimum
Return loss (S11)	$<$ -10 dB	-11.5 dB
Boresight gain (Gmin)	$>$ 6 dBi	7.00
Total Radiation Efficiency	$>$ 70%	80 %

5.5 Fabrication Process

The fabrication of THz antennas requires careful attention to detail to ensure that the designed parameters are accurately realized in the physical prototype. This involves selecting appropriate materials, employing precise fabrication techniques, and adhering to stringent quality control measures. An integral part of this process is choosing materials that perform well at THz frequencies, considering factors such as dielectric properties, loss tangents, and thermal stability.

5.5.1 Material Selection and Their Significance in the THz Frequency Range

The choice of material selection for the THz antenna fabrication process is paramount due to the distinct challenges posed by high-frequency operation. In our designs, we have specifically selected a flexible substrate with a gold layer as radiating metal which are both advantages for

THz application due to the:

- **Flexible Substrate**: Employing a flexible substrate such that polyimide presents notable advantages over a rigid substrate. Polyimide is particularly favoured due to its low dielectric losses and excellent mechanical properties, which include high flexibility and stability under thermal stress [106]. Known for its ability to withstand extreme temperatures, vibrations, and other challenging conditions, polyimide is widely used in aerospace, defence, automotive, and industrial applications [107]. The flexibility of polyimide is crucial for THz antennas that need to conform to non-standard surfaces or are required in wearable technologies [108].

- **Gold Metal**: The selection of gold for the radiating elements of an antenna is due to its excellent electrical conductivity and resistance to oxidation. At THz frequencies, shallow skin depths require materials with high conductivity to minimize resistive losses and ensure optimal antenna performance [109]. This ensures that the antenna can efficiently transmit and receive electromagnetic waves. Gold's stability under environmental exposure ensures the longevity and reliability of the antenna, which is critical in both terrestrial and space-borne applications [110].

5.5.2 Pattern Development and Job Submission Process

Prior to the fabrication process, patterns are developed using the L-Edit CAD program. This software features multiple configurable levels, a hierarchical cell structure, and capabilities for arraying. It allows for precise manipulation of features ranging from nanometers to centimetres in scale, accommodating the diverse needs of antenna array design. The hierarchical flow of the job submission process is shown in Figure 5.3.

5.5.3 Spot Size and Beam Current in Electron Beam Lithography

Some of the common spot sizes correspond to the beam current available in Vistec VB6 as shown in Table 5.3. For determining the spot size of a given beam current, the most precise method commonly employed is the knife-edge measurement [111]. In electron beam lithography, the required electron dose is determined based on the relationship between the spot size of the electron beam and the dimensions of the pattern being created. For cases where the beam's spot size exceeds the pattern dimensions, the electron dose is measured using an 'area dose'. The area dose in electron beam lithography (EBL) is influenced by two key factors: **Beam current**: It affects the spot size of the electron beam. A higher beam current results in a larger spot size. **Exposure frequency or beam step size (BSS)**: It determines the spacing between consecutive exposure points on the substrate. A smaller BSS means more exposure points and thus higher

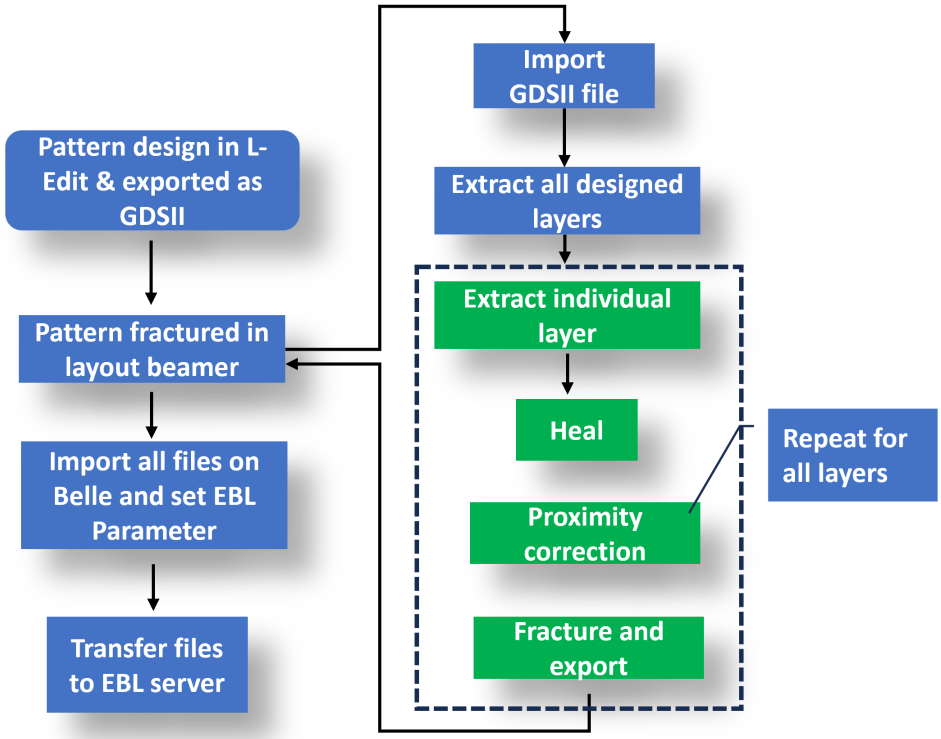

Figure 5.3: Flow of EBL job submission process

exposure frequency. The BSS is particularly important as it controls the precision of pattern development. A smaller BSS leads to higher pattern resolution but also longer write times.

$$D = \frac{I}{f \times \mathrm{BSS}^2} \quad (\mu C/cm^2) \tag{5.2}$$

where D is the area dose, I is the beam current, f is the frequency, and BSS is the beam spot size.

Table 5.3: Spot Size corresponds to the beam current

Beam current (nA)	**Spot size (nm)**
1	~3-4
2	6
4	9
8	12
16	19
32	24
64	33
100	45

5.5.4 Electron Beam Lithography (EBL)

Electron beam lithography (EBL) is a pivotal technique in the fabrication of THz antennas, as it allows for patterning extremely fine details that are critical for the small wavelengths at THz frequencies. This process utilizes a focused beam of electrons to draw custom shapes on a resist-covered substrate, achieving resolutions on the order of nanometers. Such high resolution is essential for creating the precise and intricate features of THz antenna elements, which directly influence the antenna's resonant frequency and bandwidth.

The James Watt nanofabrication (JWNC) facility utilizes a state-of-the-art Vistec vector beam (VB) 6 ultra-high resolution (UHR) extra-wide-field (EWF) electron beam lithography instrument, a Gaussian-beam lithography tool. Each shape in this tool is formed through a series of focused electron beam exposures. The instrument is equipped with a thermally assisted field emitter (TFE) source that generates an electron beam using a tungsten tip coated with Zirconium Oxide, creating a Schottky emitter that lowers the surface work function and facilitates electron tunnelling. High accelerating voltages, often reaching up to 100kV, are employed during the process, along with a beam blanker to selectively turn the beam on or off at high frequencies [112]. The system is designed to minimize the divergence of the beam using apertures, while a series of magnetic coils and quick focus coils precisely control and focus the electron beam onto the substrate surface. The result is a highly controlled lithographic process that mirrors the principles of photo-lithography, albeit with different resist coating and developing chemicals, optimized for the unique requirements of THz antenna fabrication.

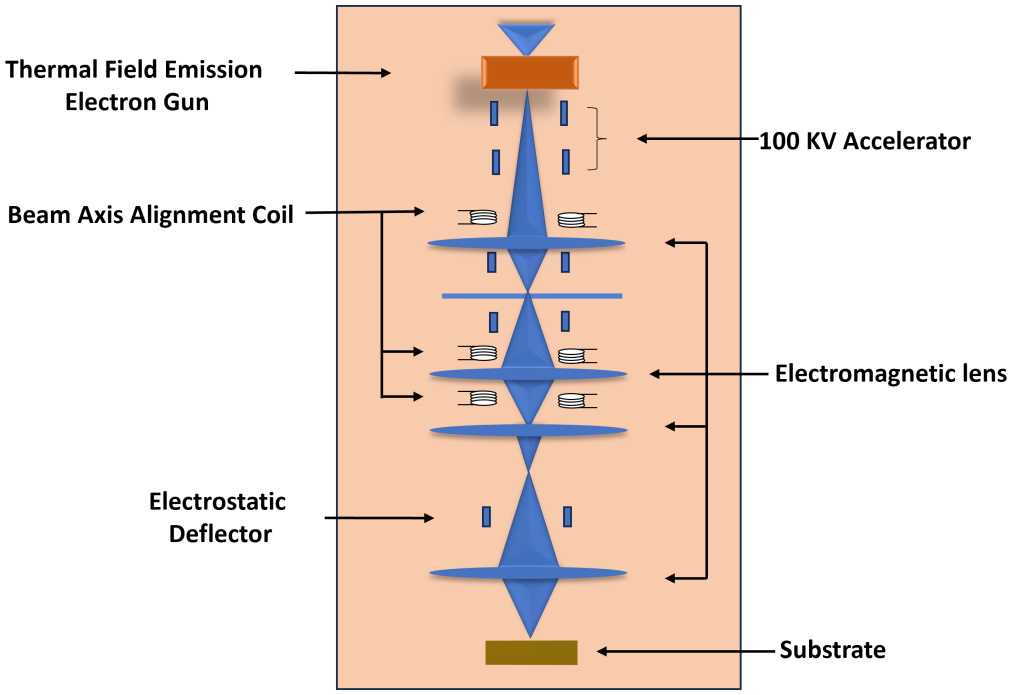

Figure 5.4: Schematic of an electron-optical Column in a VB6 Electron Beam Lithography system

5.5.5 Polymethyl Methacrylate (PMMA) Resist

Polymethyl methacrylate (PMMA) remains one of the most widely used positive-tone resists for electron beam lithography, holding its prominence for over four decades. Despite its low contrast and limited resistance to dry etching, PMMA enables the creation of ultra-high-resolution features, approaching the theoretical limits of lithography, and offers a broad processing window. PMMA is available in various molecular weights. In this study, we utilized PMMA 2010 and PMMA 2041, which have molecular weights of 150,000 MW and 500,000 MW respectively. These variants were diluted from 15% to 2.5% with anisole to achieve different resist thicknesses, allowing for a maximum resist thickness of 2 μm for PMMA 2010 and 1 μm for PMMA 2041. A brief comparison of high-resolution electron beam lithography resists is depicted in Table 5.4.

Table 5.4: Comparison of high-resolution EBL resists

Resist	**Tone**	**Sensitivity**	**Contrast**	**Etch Resistance**	**Developer**	**Resolution**
PMMA	Positive	High	Low	Poor	MIBK: IPA	∼4nm [113]
ZEP-520	Positive	High	High	High	Xylenes	∼12nm [114]
NEB-31	Negative	Low	High	High	TMAH	∼25nm [115]
HSQ	Negative	Low	High	High	TMAH	∼2.5nm [112]

5.5.6 Aluminium Wet Etching

Aluminium wet etching employs a solution based on phosphoric acid, which precisely etches aluminium with a resolution of approximately 1 micron. When removing aluminium from a surface, such as when it serves as a charge dissipation layer in electron beam lithography, a mild alkaline developer like CD26 is effective. For developing PMMA resist, a combination of Methyl isobutyl ketone (MIBK) and isopropyl alcohol (IPA) is used, with MIBK acting as the active agent. In this study, a 2.5:1 ratio of MIBK to IPA is utilized to achieve higher contrast in development.

5.5.7 Antenna Fabrication Workflow

The fabrication process of the proposed 1×4 triangular slot array was carried out at the James Watt Nanofabrication Centre (JWNC) at the University of Glasgow. Initially, the sample underwent a cleaning process using acetone and isopropanol in an ultrasonic bath. As shown in Figure 5.5 for a detailed visual representation of the subsequent fabrication steps. Following the cleaning, a bi-layer electron beam (e-beam) resist, specifically polymethyl methacrylate (PMMA), was deposited on the substrate. This involved applying a base layer of 15% PMMA, which was spin-coated at 5,000 rpm for 60 seconds with a thickness of 1260 nm and then baked at 180°C

for 2 minutes. Any resist on the back of the sample was removed with acetone prior to baking. A top layer of 4% 2041 PMMA, 150 nm thick, was subsequently spin-coated under the same conditions and similarly baked.

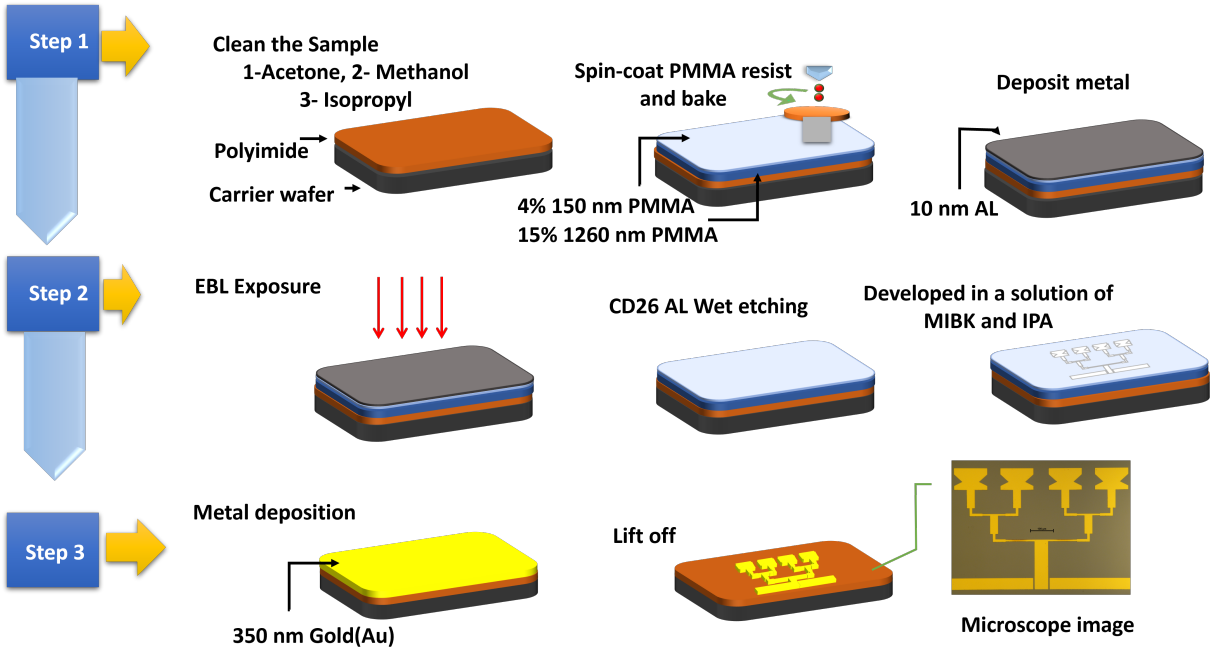

Figure 5.5: Fabrication steps for the proposed design

Before the e-beam exposure, a 10 nm thick aluminium was deposited on the top of PMMA. This acts as a charge dissipation layer (CDL), preventing static charge build-up on the surface during electron beam exposure. The CDL step is crucial to maintaining pattern fidelity and mitigating charging effects, which can cause pattern deformations, variation in feature size, and even complete pattern loss [116] [117]. Following the EBL using the Vestec VB6 beam writer, the CDL layer is stripped off from the surface. To remove, a weak alkaline developer is suitable such as CD26. The standard procedure involves immersing the substrate in CD26 for approximately one minute, which is sufficient to etch away the thin AL metal layer and then rinse thoroughly in water to halt the etching process and clear any remaining developer residues. The e-beam exposed PMMA was then developed with a 2.5:1 mixture of methyl isobutyl ketone (MIBL) at a temperature of 23 °C and rinsed in isopropyl alcohol (IPA). An inspection of the pattern fidelity was performed under a Zeiss optical microscope, known for its excellent resolution as shown in Figure 5.6 the pattern transferred on the substrate.

The undercut profile is caused by the bottom layer being more vulnerable to the e-beam dosage than the top layer. Lastly, a Ti/Au metal scheme (10 nm/350 nm) was deposited onto the patterned substrate using an electron beam evaporator (Plassys 450 MEB). The unwanted film was removed by dissolving the sample in warm acetone and placing the beaker in a hot water bath maintained at 50 °C. For 8 hours, the resist was dissolved in an acetone solution to remove any extra gold. Figure 5.7 presents a detailed front view of the antenna's profile as observed

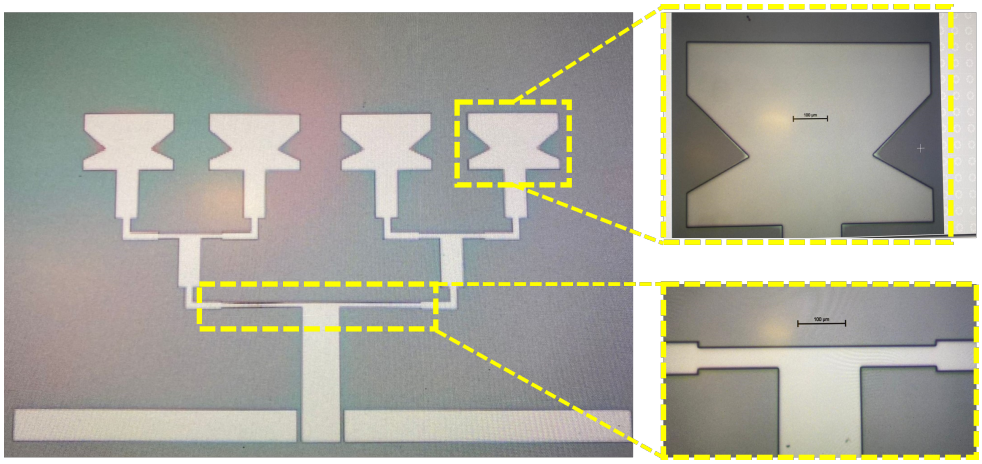

Figure 5.6: Pattern transferred on the substrate.

under the microscope. The image clearly shows the precise geometry and alignment of the feed network, along with the CPW gap (2 μm) and the width of the feed line which are crucial for antenna performance.

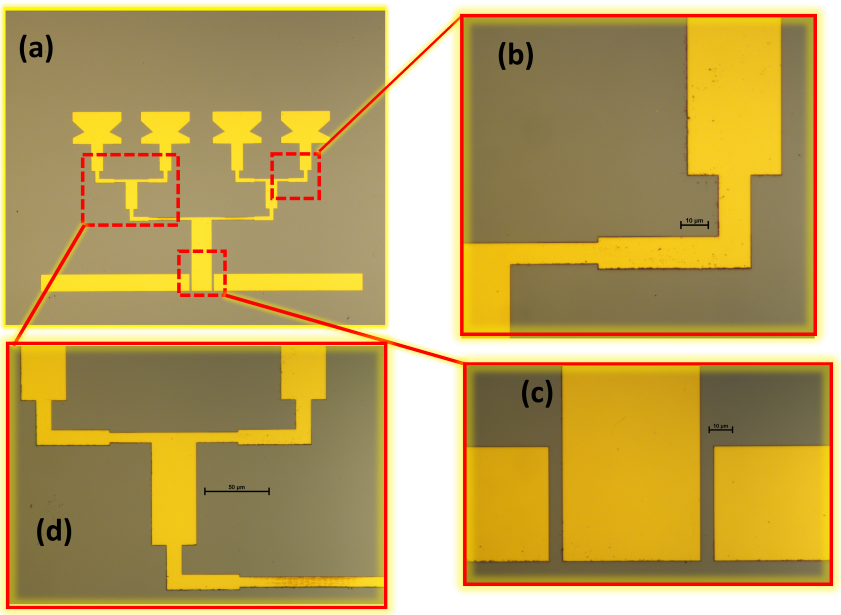

Figure 5.7: Optical image of the fabricated 1×4 triangular slot antenna array after the metal (gold) deposition: (a) full view of the antenna array, (b) feed line connection to the radiating element, (c) CPW (coplanar waveguide) gap, (d) view of the corporate feed network

Surface metrology performance measurements were meticulously acquired using the advanced optical profiler Contour GT, with the detailed results showcased in Figure 5.8. The illustrated surface profile provides a comprehensive visualization that substantiates the structural integrity of the antenna array. Notably, the profile demonstrates a pristine surface condition, with no discernible damage or cracks, indicating a high degree of precision in the fabrication process.

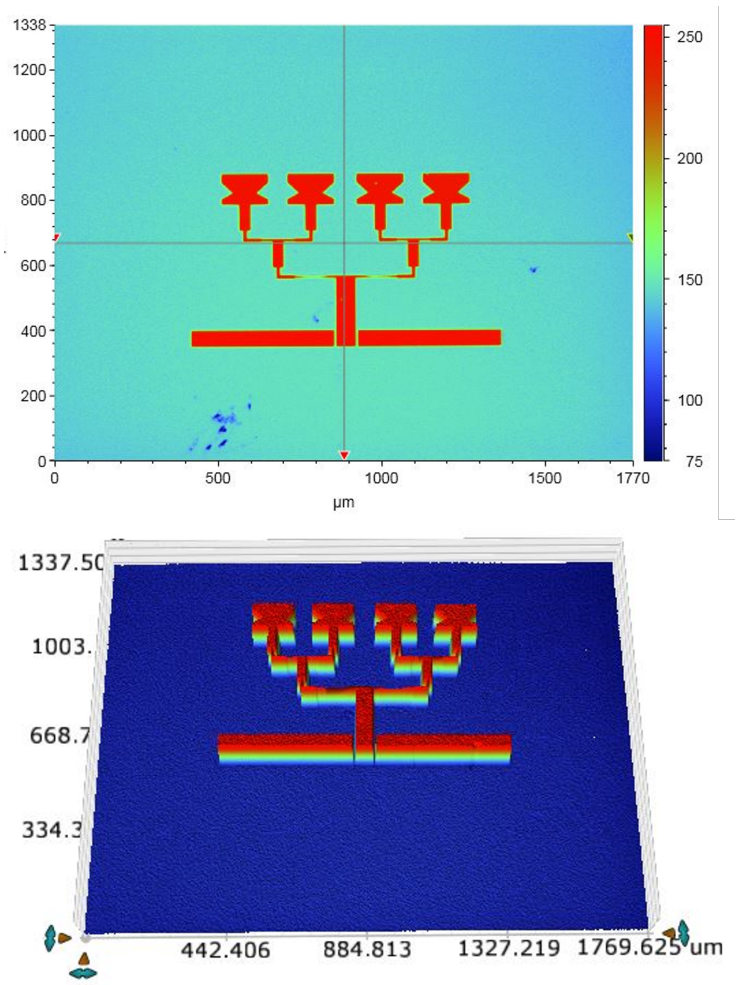

Figure 5.8: Optical counter PG image of the fabricated antenna array

5.6 Results and Discussion

The simulated reflection coefficients for the proposed antenna array and single element are depicted in Figure 5.9. The results highlight that the reflection coefficient S11, remains below -10 dB across the frequency spectrum from 0.70 to 0.95 THz, indicating a strong match. Notably at the resonance frequency 0.86 THz S11 dips to -45 dB. Furthermore, the antenna array exhibits an impedance bandwidth of 37.50%. The voltage standing wave ratio (VSWR) is maintained below 1.5, suggesting that the antenna array provides reliable performance within the specified frequency spectrum. The compact size and broad impedance bandwidth of the proposed antenna make it a promising candidate for future wireless communication.

Furthermore, Figure 5.10 shows the simulated realized gain and efficiency (radiation efficiency and total efficiency) versus the frequency of the designed antenna array, where it can be seen that the peak realized gain is 7.2 dBi at a 0.80 THz while the minimum in-band realized gain is observed to be 7.1 dBi. In contrast, the simulated realized gain consistently exceeds 6 dBi across the band of interest (0.70-0.95 THz). The gain variation within the operating band of interest for this array is minimal, suggesting a stable performance across the spectrum with

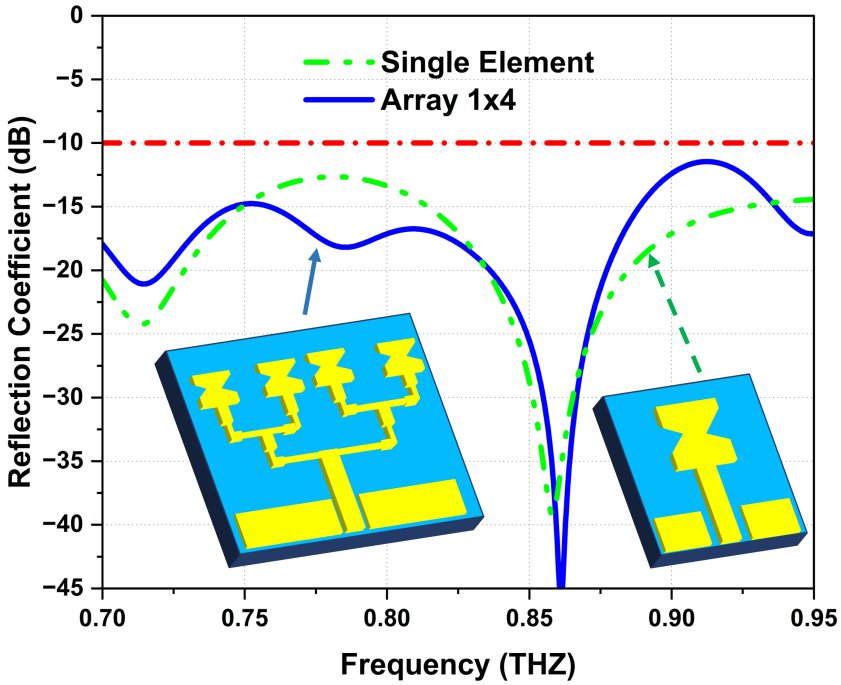

Figure 5.9: Simulated Reflection co-efficient of a single element and proposed THz antenna array

variations possibly within a narrow window of less than 1 dBi. These findings underscore the impact of design and optimization strategies on enhancing the performance of antenna elements and their configurations. Additionally, the total efficiency of the antenna remains consistently high across the entire operating band, ranging from 80% to 88%, with the minimum in-band total efficiency being 83.12%. This performance is consistently maintained above the 70% threshold as shown in Table 5.2, across the entire frequency range, showcasing a stable efficiency profile. This indicates that the antenna can effectively convert input power into radiated power with minimal losses.

In Figure 5.11, the simulated far-field radiation pattern results for the designed antenna array are shown, highlighting its strong directional radiation toward the broadside. The main lobes, representing the peak of radiation intensity, are clearly centred at approximately 0° in both the E and H planes across the displayed frequency range (0.75 THz to 0.95 THz). Notably, the SLLs are significantly suppressed, measuring below -9 dB in both planes. Furthermore, the simulated 3dB bandwidth is recorded as 36.5° in the E-plane and 26° in the H-plane, suggesting a relatively narrow beamwidth, especially in the H-plane. Such a narrow beamwidth is typically indicative of a more focused radiation pattern, which is desirable for targeting or direction-specific applications. Despite this, the consistent behaviour demonstrated in the simulated patterns suggests the antenna array's potential for stable and efficient performance within the THz spectrum.

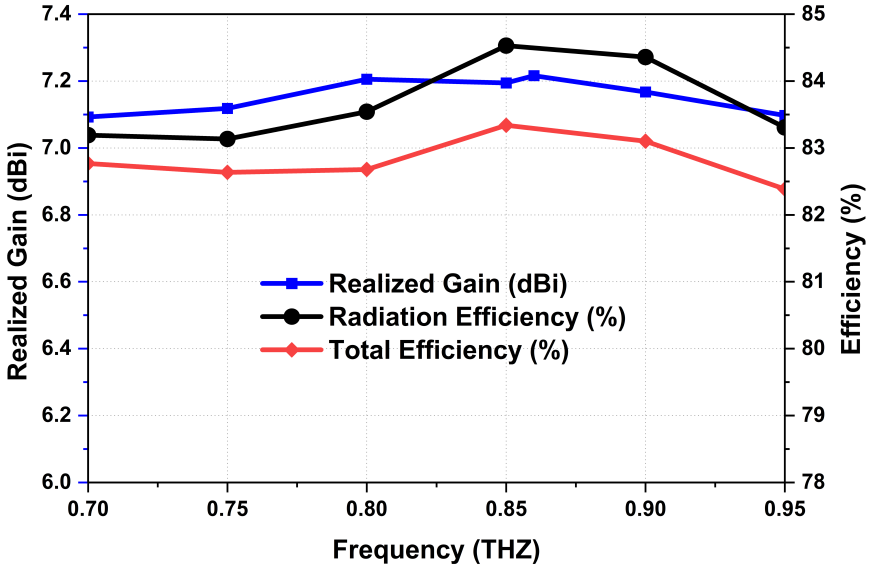

Figure 5.10: Simulated Realized Gain and Efficiency

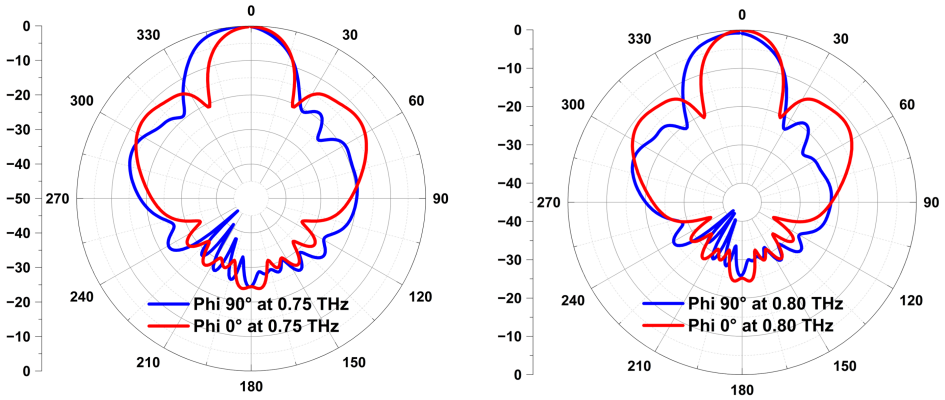

(a) Simulated radiation pattern in E and H-planes at frequencies 0.75 THz and 0.80 THz

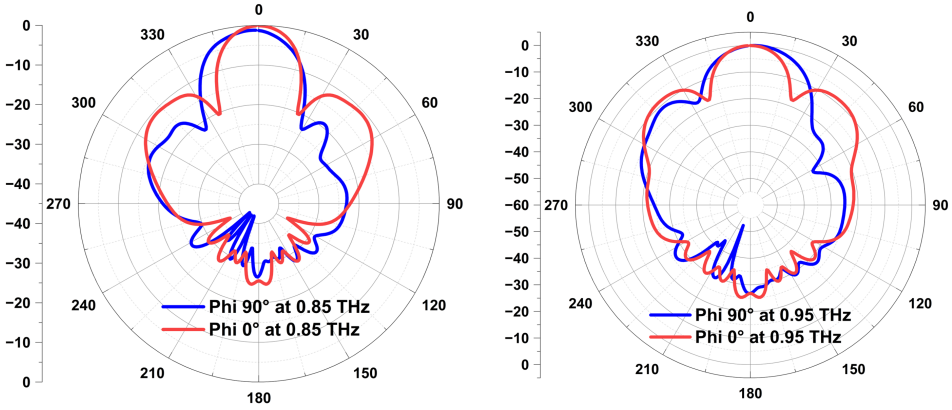

(b) Simulated radiation pattern in E and H-planes at frequencies 0.85 THz and 0.95 THz

Figure 5.11: Simulated radiation pattern of the proposed antenna at the various frequencies from (0.75 to 0.95 THz)

5.7 Hybrid-fed THz Antenna Array with 64 Elements

The antenna is one of the main components for successfully deploying cellular communication in the 6G at THz frequencies. Therefore, it is necessary to use techniques such as microstrip array, and slotting patches, to increase the gain and the impedance bandwidth. This section utilizes a hybrid feeding approach that combines the advantages of both direct and indirect feeding methods, improving the overall efficiency and bandwidth capabilities of the array. The design leverages microstrip arrays for their compact size and ease of integration, while slotting patches are employed to enhance the radiation pattern and minimize losses. Simulation results demonstrate that the antenna array operates effectively across the THz spectrum, achieving high gain and wide impedance bandwidth, which are critical for supporting the ultra-high frequency and broad bandwidth requirements of 6G technology.

5.7.1 Single Element Design

The initial design of a unit element within the THz antenna array is depicted in Figure 5.12. The antenna is modelled using CST-MWS 2022, with a configuration set to a maximum cell density of 15 cells per wavelength to have 500,000 hexahedral mesh cells in total. It is then analyzed using the finite integration technique with a time-domain solver have an accuracy of -40 dB. For the design of the microstrip THz patch antenna, we selected the resonance frequency and dielectric medium for which the antenna is to be designed, and then the parameters of the antenna can be calculated as follows. The width of the patch is calculated using the following equation:

$$W \approx \frac{c}{2f_r\sqrt{\frac{2}{\varepsilon_r+1}}} \tag{5.3}$$

The design of a microstrip patch antenna involves various key parameters. The resonance frequency is denoted by f_0, the width of the patch by W, the length of the patch by L, and the thickness of the patch by h. The relative permittivity of the dielectric substrate is represented by ε_r, and the speed of light is typically taken as 3×10^8 meters per second. An important aspect in the design is the effective refractive index value of a patch, which significantly influences how the radiation travels from the patch towards the ground. This radiation passage, known as the fringing effect, occurs through both the air and the substrate, which possess different dielectric values. The effective dielectric constant, ε_{rff}, is crucial in this context and is calculated using the following equation:

$$\varepsilon_{\text{rff}} = \frac{\varepsilon_r+1}{2} + \frac{\varepsilon_r-1}{2}\left[\frac{1}{\sqrt{1+12\frac{h}{W}}}\right] \tag{5.4}$$

Furthermore, due to the fringing effect, the electrically perceived size of the antenna increases. This fringing effect means that the patch appears larger than its physical dimensions, primarily due to the extension of the electric field beyond the physical boundaries of the patch. The actual increase in length ΔL of the patch due to fringing is calculated using the following equation:

$$\frac{\Delta L}{h} = 0.412 \frac{(\varepsilon_{\text{rff}} + 0.3)\left(\frac{W}{h} + 0.264\right)}{(\varepsilon_{\text{rff}} + 0.258)\left(\frac{W}{h} + 0.8\right)} \tag{5.5}$$

With this adjustment, the effective length L of the patch, including the fringing effect, is then recalculated to ensure accurate design and optimal antenna performance. The length L is given by the following equation:

$$L = \frac{c}{2 f_r \sqrt{\varepsilon_{\text{eff}}}} - 2(\Delta L) \tag{5.6}$$

The design comprises a driven patch fed by a 50Ω microstrip line, employing an inset-feed mechanism to ensure optimal feeding of the truncated square patch. This configuration is supported by two uniform, truncated rectangular planes, that are abreast and separated by a microstrip line serving as a co-planar partial ground. The truncation of the ground plane primarily enhances the input impedance and the uniform gap width, M_G, between the co-planar ground planes and the microstrip line. To match the input impedance of the antenna to the standard 50 Ω, the dimensions of the microstrip transmission line are crucial. As shown in Figure 5.12, the width and length of the microstrip transmission line required to achieve 50Ω antenna input impedance at the desired frequency are calculated using the following equations:

$$W_T = \frac{1}{0.8}\left[\frac{9.513h}{\sqrt{\lambda (L_{3\pi} + 1.41) W}} - t\right] \tag{5.7}$$

$$L_T = 2(2M+1)\frac{\lambda}{2} \tag{5.8}$$

The use of coplanar waveguide feed provides several benefits, including good impedance matching with a sufficient substrate thickness, low transmission loss, minimal frequency dispersion, and easy integration with monolithic circuit designs. Furthermore, the inset feed mechanism allows for meticulous fine-tuning of the impedance, facilitating an optimal match between the antenna and the feed line. This section will also discuss how SB-SADEA optimization techniques are applied to refine these design parameters, enhancing the antenna performance across THz frequency.

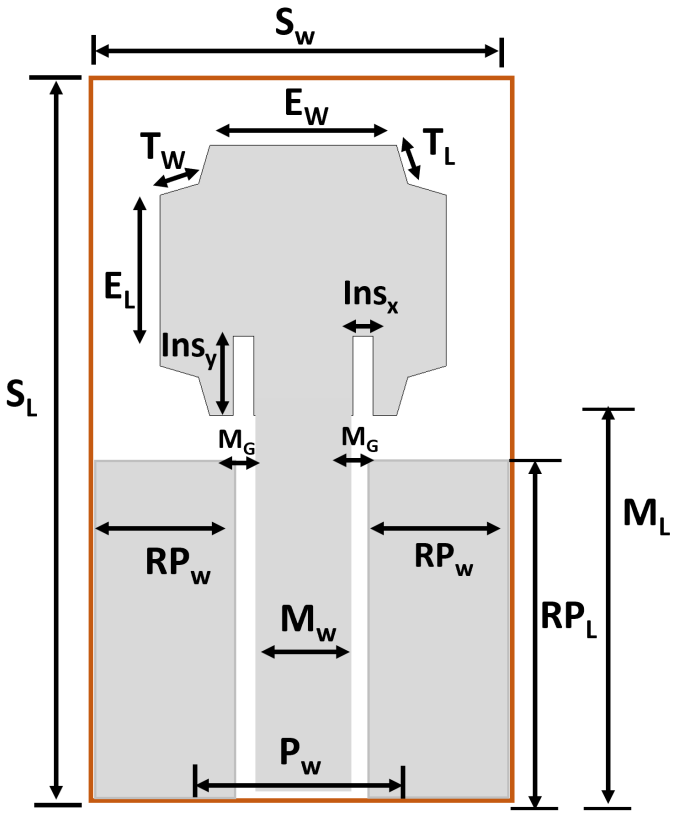

Figure 5.12: A unit-element antenna layout

5.7.2 AI-driven Design Optimization Using SB-SADEA

The THz element antenna is optimized by considering several critical design parameters that influence its frequency response and performance specifications to make it suitable for THz wireless applications (see Tables 5.5 and 5.6). With 13 critical design parameters and 3 performance specifications to consider, manual optimization of the THz antenna becomes exceedingly difficult.

In THz antenna designs, where precise tuning is crucial due to the high sensitivity of the antenna's performance to small changes, manual adjustments are not only inefficient but also potentially ineffective. Off-the-shelf optimization techniques such as practical swarm optimization (PSO), covariance matrix adaptation evolution strategy (CMA-ES), and Trust region framework (TRF) are also employed. However, results from a typical CST-MWS 2020 TRF were not satisfactory, and the use of PSO was found to incur prohibitive computational overhead without ensuring successful outcomes. Hence, a self-adaptive Bayesian neural network surrogate model-assisted differential evolution for antenna optimization (SB-SADEA), a purpose-built method for machine learning-assisted global optimization of high-dimensional antennas, is employed [69].

The essential steps in the SB-SADEA workflow and additional information about the SB-SADEA approach are available in [69]. In SB-SADEA, the supervised learning method utilized

Table 5.5: Search ranges of the design parameters and the optimal design by SB-SADEA for the THz unit element antenna (All dimensions in μm)

No	Parameters	Lower bound	Upper bound	SB-SADEA Optimum
1	E_L	150	290	163.29
2	E_W	175	290	173.06
3	M_L	50	200	171.14
4	T_W	15	35	30.12
5	T_L	>Ux	30	20.12
6	Ins_x	>0.00	40	12.32
7	Ins_y	10	80	48.15
8	M_G	>0.00	4	2.12
9	P_W	$6 \times M_W$	$10 \times M_W$	9.45
10	R_{PL}	10	M_L	54.02
11	S_W	$2 \times E_W$	$3 \times E_W$	490
12	Substrate length (S_L)	$S_L = M_L + (2 \times E_L) + 5\mu m$		
13	Partial ground plane width (R_{PW})	$R_{PW} = (S_W - (2 \times M_G) - M_W)/2\mu m$		

Table 5.6: Performance Specification (Frequency 0.75 to 1.1 THz)

No	Item	Specification	SB-SADEA Optimum
1	Maximum return loss (S_{11})	≤ -10 dB	12.02 dB
2	Minimum Realized Gain	≥ 6 dBi	6.7 dBi
3	Minimum Total Efficiency	$\geq 70\%$	80%

is a Bayesian Neural Network (BNN), rather than a Gaussian Process (GP). This BNN is used to construct surrogate models that approximate the performance of antenna designs. The integration of this surrogate modeling with differential evolution (DE)-based global search helps achieve a balanced exploration and exploitation of the antenna design search space.

The management of the model in SB-SADEA focuses on continuous, dynamic updating. As the system iteratively processes through the optimization cycle, the BNN surrogate model is repeatedly updated with new data from the latest simulations. This ensures that the model adapts and improves its predictions throughout the optimization process.

A flow diagram of the SB-SADEA process can visually outline these steps as shown in Figure 5.13, illustrating how each iteration of the optimization cycle progresses. In each iteration of SB-SADEA, the BNN surrogate model is updated using data from newly simulated candidate designs and their performance metrics. New candidate designs are then generated through DE mutation and crossover operations. The performance of these designs is predicted using the updated surrogate model. High-potential designs, identified through a self-adaptive lower

confidence bound that considers both the predictions and their uncertainties, are then physically simulated. The results from these simulations are used to further refine and update the surrogate model, feeding into the next iteration. This process continues until a predefined stopping criterion is met, which could involve the exhaustion of computational resources or reaching a specific performance threshold. This methodological approach ensures a robust and adaptive optimization process, enhancing the efficiency and effectiveness of the antenna design search.

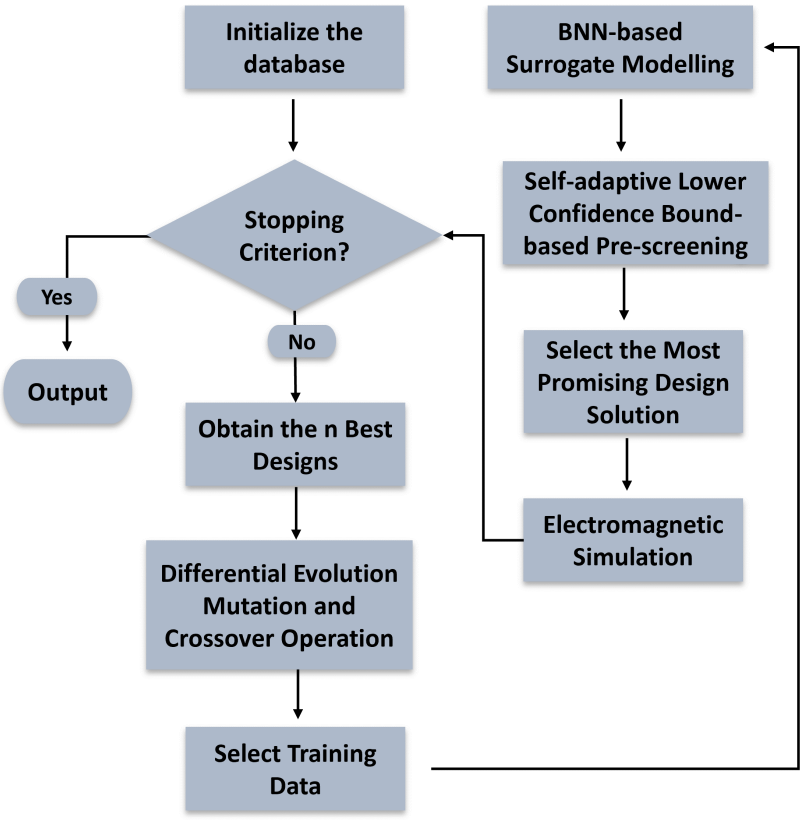

Figure 5.13: Flow diagram of the SB-SADEA method

For the SB-SADEA-driven optimization of the unit element THz antenna, the design parameters, their geometric constraints, and the respective search ranges listed in Table 5.5 are considered for the minimization of the fitness function F_{mpa} in Equation 5.9. This optimization aims to satisfy the specifications listed in Table 5.6 better than those of the reference design. Note that even though the size of the antenna is not explicitly included in Equation 5.9, the search ranges and geometric constraints are meticulously defined to ensure that the antenna maintains a low profile. For example, in the optimization process, the microstrip length (M_L) cannot exceed 200 µm, and the partial ground plane length (RPL) cannot exceed M_L, as specified in Table 5.5.

$$F_{mpa} = \max(|S_{11}|) + w \cdot \max([6\ \text{dBi} - G_{\min}], 0) + w \cdot \max([0.70 - \eta_{\min}], 0) \tag{5.9}$$

Where w is the penalty coefficient and is set to 50. By setting w to 50, the specifications for the realized gain and total efficiency are prioritized by largely penalizing F_{mpa} if they are

violated. Once these specifications are met, the focus shifts to meeting the S_{11} requirements. After 32 hours of optimization, SB-SADEA obtained the optimal design parameters listed in Table 5.5, with the performance specifications shown in Table 5.6. It can be seen that all the specifications are satisfied. The physical implementation of the hybrid-fed antenna array will be discussed in detail in the coming section.

5.7.3 Results and Discussion

The simulated reflection coefficients for the optimized single-element antenna are illustrated in Figure 5.14a, demonstrating excellent antenna performance across the spectrum. The antenna maintains a -10 dB impedance bandwidth from 0.75 to 1.1 THz, representing a bandwidth of 0.35 THz and a fractional bandwidth of 37.8%. In contrast, the conventional patch antenna shows a limited fractional bandwidth of 16.8% over two distinct frequency ranges. The optimization, facilitated by employing SB-SADEA techniques and incorporating design improvements, significantly enhances the antenna's electrical characteristics, leading to superior performance in terms of both bandwidth and consistency across the targeted frequency spectrum. Figure 5.15 shows that the optimized single-element antenna achieves a realized gain above 6 dBi across the band of interest (0.75 to 1.1 THz), as mentioned in Table 5.6, providing less than 1 dB gain variation within the desired frequency band.

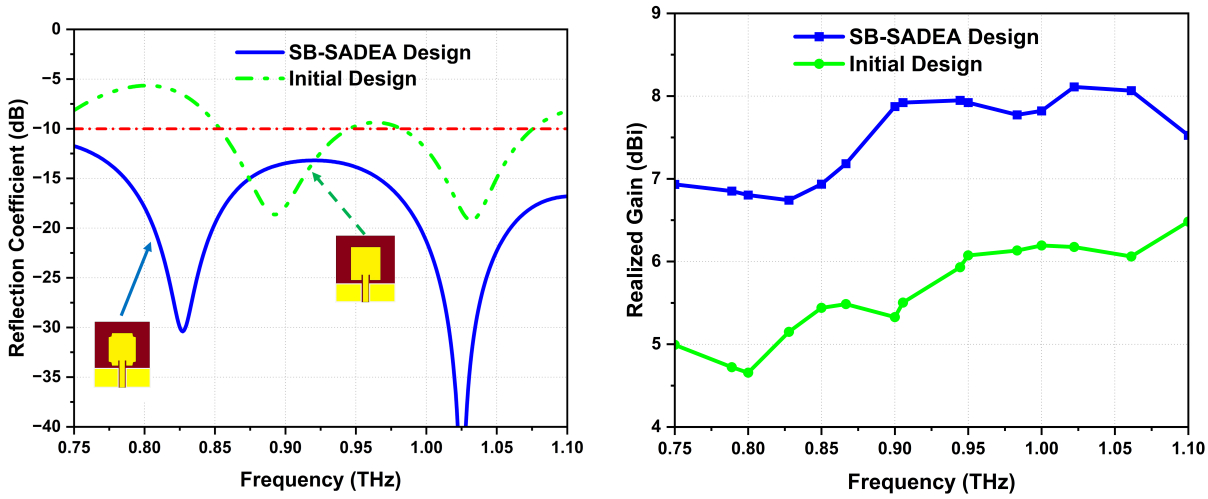

(a) Simulated reflection coefficient (S_{11})

(b) Realized gain of the single element antenna

Figure 5.14: Simulated results for the single element THz antenna: (a) S11, and (b) realized gain.

The total efficiency of the optimized single-element antenna in the 0.75-1.1 THz band is greater than 81.33%, as shown in Figure 5.15. This indicates consistently high performance over a wide frequency range, which is important for various applications requiring reliable and efficient operation. The optimal design of the antenna ensures that it maintains high efficiency with minimal fluctuations across the frequency range. This performance stability is particularly

important in practical applications, where it is important to maintain performance across different frequencies for continuous functionality. Antenna design enhancements focus on reducing losses due to impedance mismatch and material imperfections, which are common challenges in high-frequency antenna performance. By solving these problems, an optimized single-element antenna can provide higher overall efficiency. Furthermore, the stable performance in the 0.75-1.1 THz band makes the antenna suitable for a wide range of applications, including high-speed wireless communication, imaging systems, and spectroscopy.

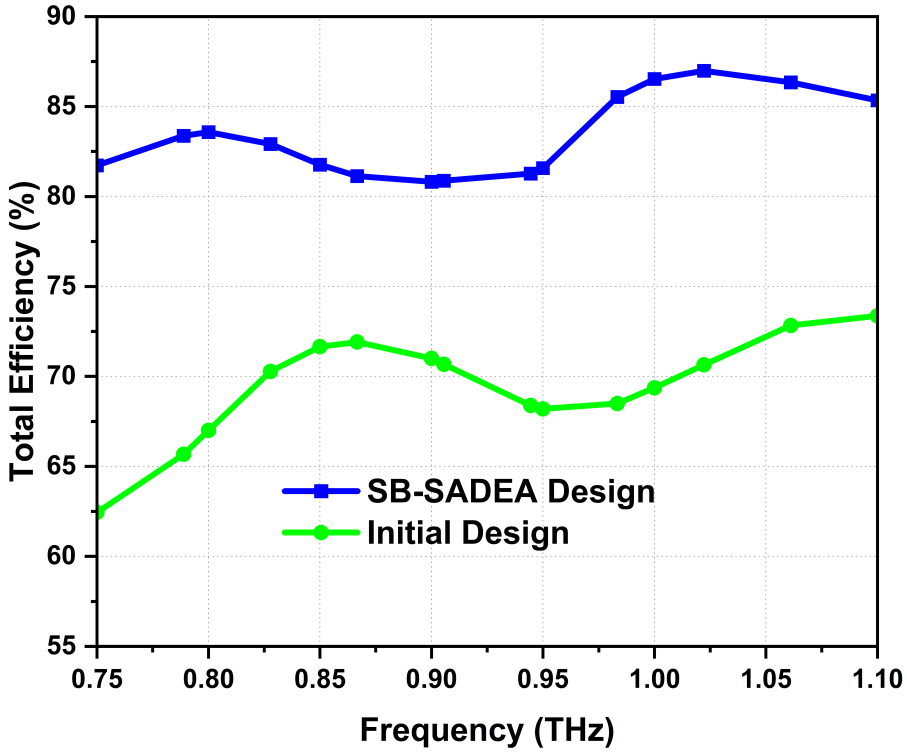

Figure 5.15: Simulated total efficiency.

5.7.4 Design and Performance Analysis of an 8×8 Hybrid-fed THz Antenna Array

The high gain of the antenna array reduces the required transmit power and enhances the signal-to-noise ratio (SNR) at the receiver ends, crucial for mitigating path loss and enabling reliable communication over a few meters in THz communication. To design a compact and high gain array an 8-channel equal power divider is designed and integrated with the proposed 1×8 sub-array at each output port of the divider as shown in Figure 5.16. In this way, each proposed 1×8 linear array acts as a sub-array to design a compact 64-element (8×8) hybrid-fed array. The design of the power divider prioritizes low insertion loss, ensuring maximum energy is equally distributed across each outport (i.e., the input of sub-array antenna) with equal magnitude and phase across all transmission coefficients (S_{21}, S_{31}, S_{41} etc). To achieve this, the power divider's

design ensures that all transmission paths from the input to the various outputs are of equal length and exhibit minimal phase shift differences. This Symmetry is crucial for maintaining the phase coherence necessary for the effective directional capabilities of the 8×8 array. Ideally, in an 8-way equal power divider, each port (port-B to port-I) should receive one-eighth of the total power, corresponding to -9 dB. As illustrated in Figure 5.16, the power divider exhibits an insertion loss ranging from -9.6 to -10 dB.

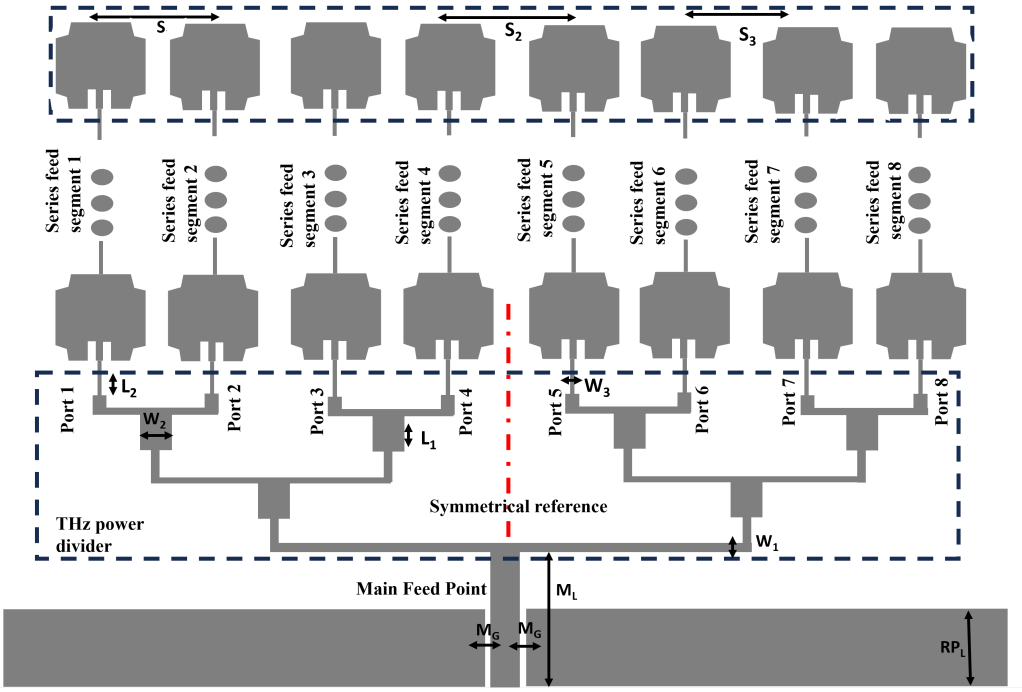

Figure 5.16: The Schematic configuration of the proposed hybrid-fed THz antenna array.

5.7.5 Optimization of Hybrid-fed THz Antenna Array Using SB-SADEA

Designing an efficient and wideband power divider is inherently challenging, particularly because even minor adjustments in the length and width of the feed junction can significantly impact the array bandwidth and overall performance. At the THz frequency band, a directional antenna array with high gain is crucial to mitigate path loss. We aimed to optimize the physical configuration and electronic behavior of the THz antenna array to maximize performance across its operational bandwidth. The SB-SADEA algorithm is employed to achieve the target specifications.

While SADEA-I has been effective in various antenna optimization in [84] [64] [68], SB-SADEA was chosen for this optimization due to its enhanced ability to handle high-dimensional design spaces and complex optimization landscapes typical of THz antenna designs. SB-SADEA integrates a Bayesian Neural Network (BNN) for surrogate modeling, which provides more accurate approximations of the performance metrics and adapts dynamically with new simulation data, improving the optimization efficiency and effectiveness.

For the synthesis of the THz antenna array, the critical design parameters are shown in Figure 5.16, and their search ranges are listed in Table 5.7. The optimization goal is the minimization of the fitness function F_{mpa} in Equation 5.10 to satisfy the design specifications in Table 5.8.

$$F_{\text{mpa}} = \max(|S_{11}|) + w \cdot \max([10\ \text{dBi} - G_{\text{min}}], 0) + w \cdot \max([0.70 - \eta_{\text{min}}], 0) \tag{5.10}$$

Where w is the penalty coefficient and is set to 50. By setting w to 50, the specifications for the realized gain and total efficiency are prioritized by largely penalizing F_{mpa} if they are violated. Subsequently, the focus shifts to satisfying the S_{11} requirements. Table 5.7 illustrates a typical optimal design obtained using SB-SADEA after 55 hours of optimization, with all specified criteria successfully met.For comparison, the computing budget used for SB-SADEA is 550 simulations over 3 runs, while 3000 simulations over five runs were conducted for both PSO and CMA-ES. In terms of quality results, SB-SADEA, SADEA-I, and CMA-ES methods satisfy the $\max(|S_{11}|)$ overall run in this case. Even in the worst case, the $\max(S_{11})$ performance obtained by SB-SADEA/SADEA-I is still very good. Note that the convergence trend for the Trust region framework (TRF) is not shown in Figure 5.17 because it is not applicable due to geometric incongruities.

The Figure 5.17 shows the convergence behavior of different optimization algorithms (SB-SADEA, SADEA-I, CMA-ES, PSO) in terms of the maximum reflection coefficient $|S_{11}|$ within the operational band. The term "Max $|S_{11}|$" is used because the plot tracks the highest value of $|S_{11}|$ found during the optimization process across the operational bandwidth. The plot specifically deals with these maximum values to monitor and minimize the worst-case reflection coefficient.

Table 5.7: Search ranges of the design parameters and the optimal design by SB-SADEA for the THz antenna array (All dimensions in μm)

No	Parameter	Lower Bounds	Upper Bounds	SB-SADEA
1	M_G	>0.00	4	2.5
2	S1	200	335	293.5
3	S2	260	290	280.15
4	S3	276.5	295	285.27
5	L1	12	60	55.14
6	L2	10	80	50.21
7	W1	≥ 0.00	5.00	4.73
8	W2	10	40	30.12
9	W3	≥ 0.00	4	2.18
10	RPL	10	M_G	54.03
11	ML	50	200	171.25

Table 5.8: Performance Specification for THz antenna array (Frequency 0.75 to 1.1 THz)

No	Item	Specifications	SB-SADEA Optimum
1	Maximum return loss (S11)	≤ -10 dB	-12.02 dB
2	Minimum bore-sight gain (Gmin)	≥ 10 dBi	13.9 dBi
3	Minimum Total Efficiency (Gmix)	$\geq 70\%$	80%

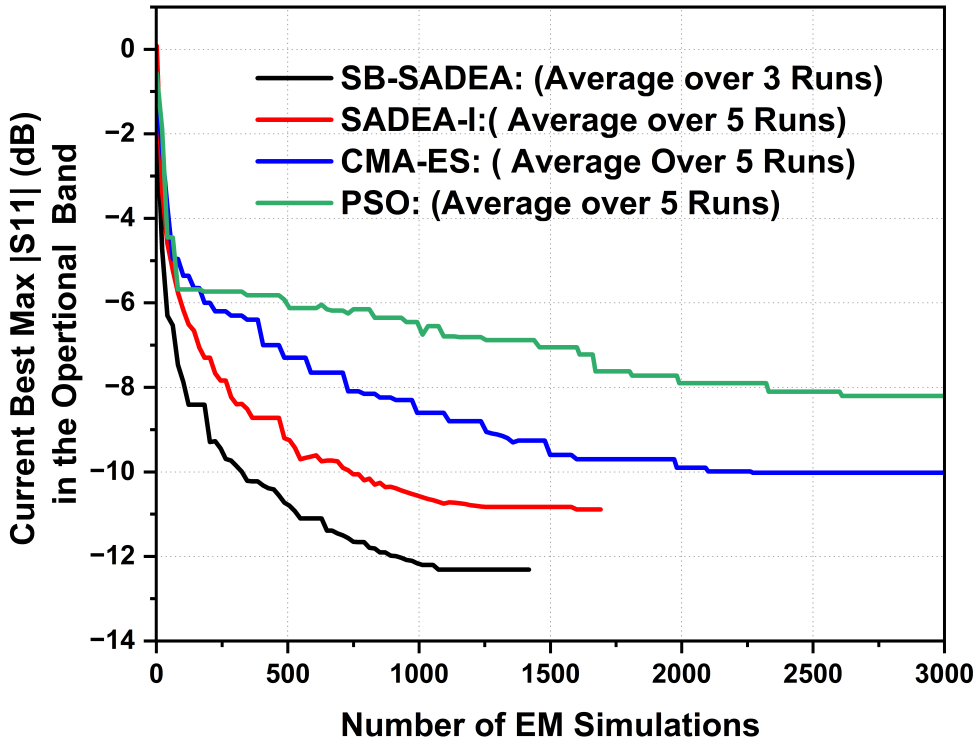

Figure 5.17: Convergence plot comparing the performance of various optimization methods (SB-SADEA, SADEA-I, PSO, and CMA-ES) in terms of the number of EM simulations required to achieve the desired performance metrics

5.8 Antenna Array Fabrication

This section gives a brief overview of the hybrid THz antenna array fabrication process as applied in our study as shown in Figure 5.18. Prior to resist spinning, the substrates are ultrasonically cleaned in successive baths of acetone/isopropyl alcohol, de-ionized water, and dehydrated and baked on a vacuum hotplate at 180°C for 2 minutes to eliminate any residues. A bi-layer resist consisting of 15% 2010 PMMA and 4% 2041 PMMA is then spun onto the substrate at 5000 rpm, achieving approximate thicknesses of 1.2 μm and 0.125 μm, respectively. Each layer is subsequently baked on a vacuum hotplate at 180°C for 2 minutes. The substrates undergo exposure to a dose of 650 μC/cm^2, with a beam step size (BSS) of 33 nm and a spot

size of approximately 20 nm. Post-exposure, the substrates are developed in a 2.5:1 MIBK:IPA solution for 90 seconds, rinsed in IPA for 10 seconds, and then dried using nitrogen (N_2).

The substrate is further processed by ashing in oxygen (O_2) plasma at 10 SCCM, 50 mTorr, and 100 W for 30 seconds using a reactive ion etch tool to remove any residual resist. The metal is then evaporated to a thickness of 350 nm using a Plassys-IV electron beam evaporator. Subsequently, the substrate is immersed in acetone and placed in a hot water bath maintained at 50°C for around eight hours to facilitate the lift-off process. This step removes the unwanted metal, leaving behind the bond pads. Ideally, the thickness of the evaporated metal should not exceed 1/3rd of the thickness of the bottom PMMA layer to ensure a smooth lift-off process without the need for ultrasonic agitation. The magnified fabricated THz antenna array are in detailed in Figure 5.18(a) along with the voltage divider as shown in Figure 5.18(b-d).

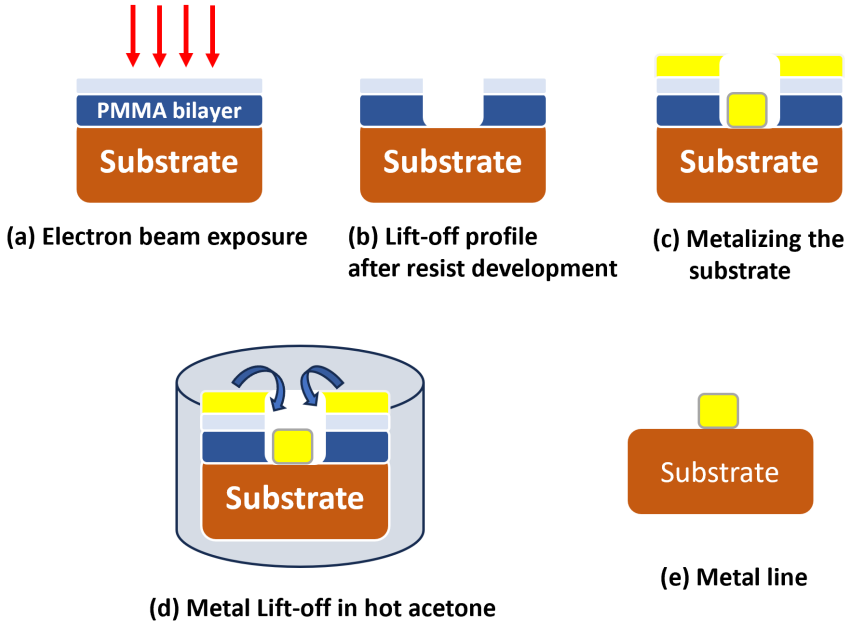

Figure 5.18: Lift-off steps.

Additionally, the substrate used in the fabrication is slightly larger than that used in the simulation to ensure stability during the fabrication process, using tweezers to hold the antenna array. This modification helps avoid the effects on the radiating parts of the array that could occur if the substrate were as small as in the simulation. It should be noted that in the simulations, increasing the substrate size was also tested and found to have a negligible effect on performance.

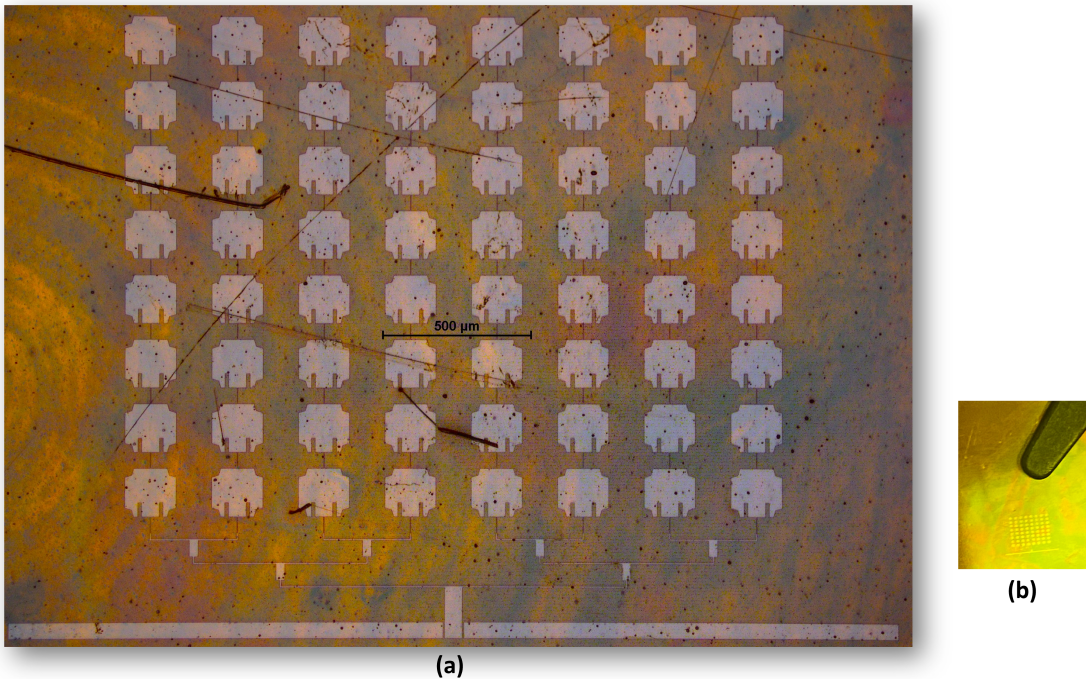

(a) An optical microscope image of the hybrid-fed 8×8 THz antenna array (b) Compare it with tweezers

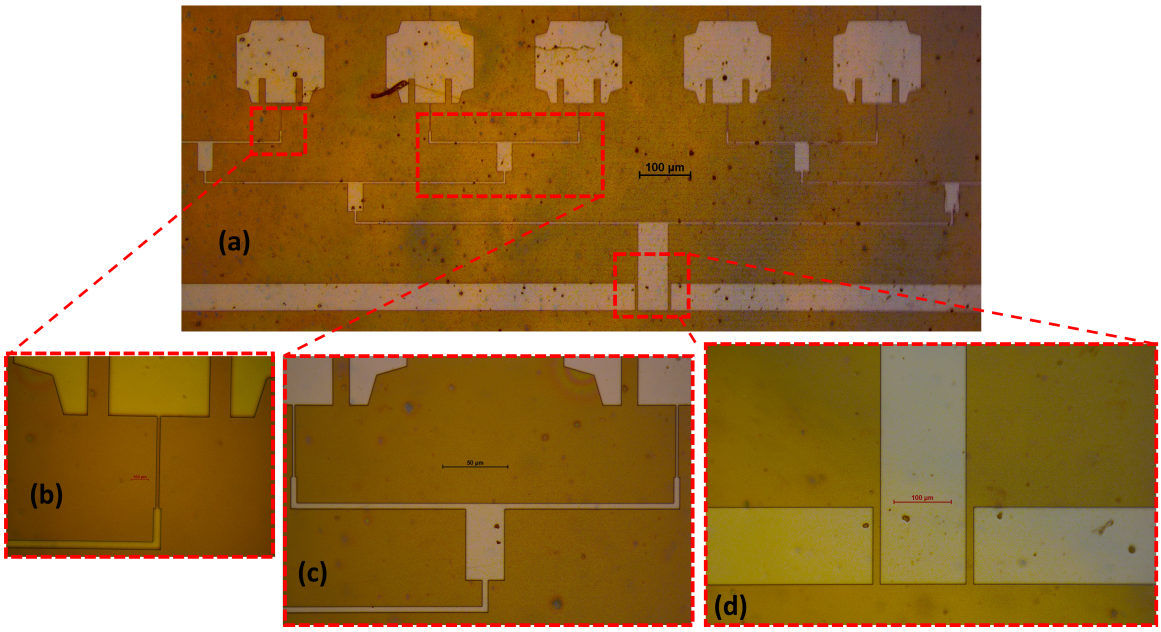

(b) Magnified image of the Hybrid-fed THz antenna array components: (a) port 1-4 network along with a truncated patch (b) Feed transmission line to patch with a width of 1.5 µm (c)Corporate fed junction (d) CPW (Coplanar Waveguide) with a 2µm gap.

Figure 5.19: Detail views of the proposed Hybrid-fed THz antenna array

5.9 Results and Discussion

In this section, we present and analyze the performance metrics of the proposed THz antenna array. Evaluation criteria include return loss, VSWR, input impedance, directivity, and radiation patterns in both the E- and H-planes. Each of these parameters is important for evaluating

antenna effectiveness in practical applications, particularly in the terahertz range.

5.9.1 Reflection Coefficient and Gain

The reflection coefficient, often denoted as S_{11}, is a key parameter that indicates how much power is reflected to the source due to impedance mismatch. For the proposed THz antenna array, the reflection coefficient is carefully measured over the entire operating bandwidth. The results, shown in Figure 5.20, consistently show values below -10 dB in the desired frequency range. The -10 dB impedance bandwidth spans 35.50%, covering the frequency range from 0.75 to 1.1 THz. However, the voltage standing wave ratio (VSWR) measures the amount of signal reflected to the source due to impedance mismatch. The VSWR of the proposed antenna is less than 1.5 over the entire target frequency range, indicating excellent impedance matching and minimal signal reflection.

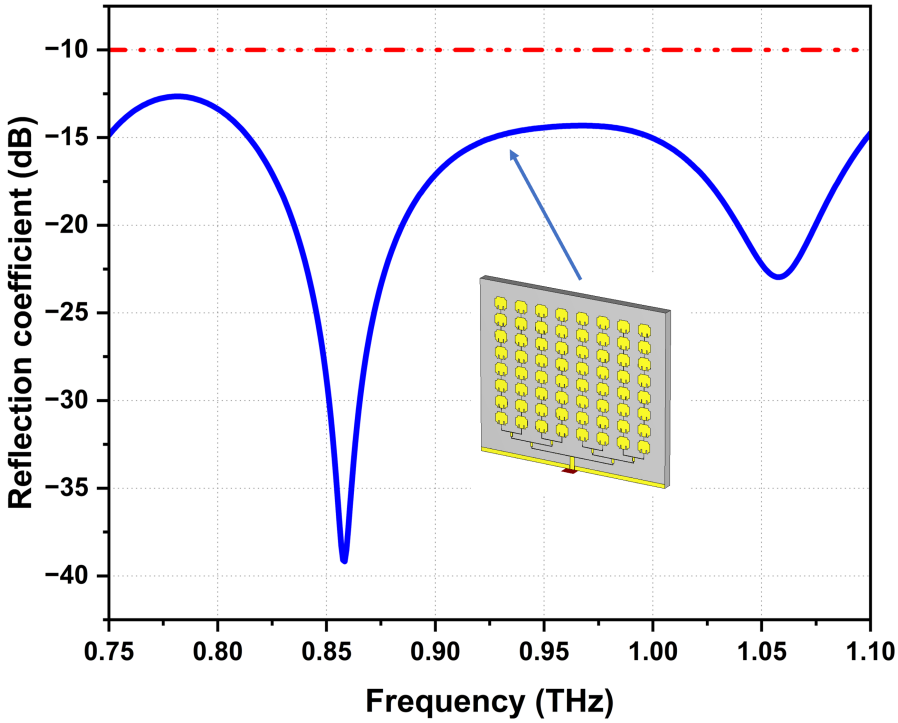

Figure 5.20: Typical S_{11} response of the optimized Hybrid-feed THz antenna array(SB-SADEA)

Typical responses of the optimised Antenna gain measures how efficiently an antenna converts input power into radio waves in a specific direction, compared to a hypothetical isotropic antenna that radiates equally in all directions. The proposed THz antenna array exhibits a peak gain of 15.05 dBi at 0.95 THz and is consistent over the entire operating frequency, as shown in Figure 5.21, with less than 1.5 dB gain variation such as higher values indicating effective radiation of energy in the desired direction. High gain is critical for long-distance communications and maintaining signal integrity over large areas, particularly in terahertz communication systems, which highlights the effectiveness of antennas in applications requiring strong directional

signals. Moreover, the directivity of the proposed antenna is shown in Figure 5.21 which means that the radiated energy is effectively concentrated in a specific direction. This high directivity reduces power loss and interference from other sources, benefiting applications that require precise signal location, such as point-to-point communications and radar systems. Additionally, the high directivity enhances the antenna's ability to operate efficiently in the crowded terahertz spectrum, where minimizing interference is critical.

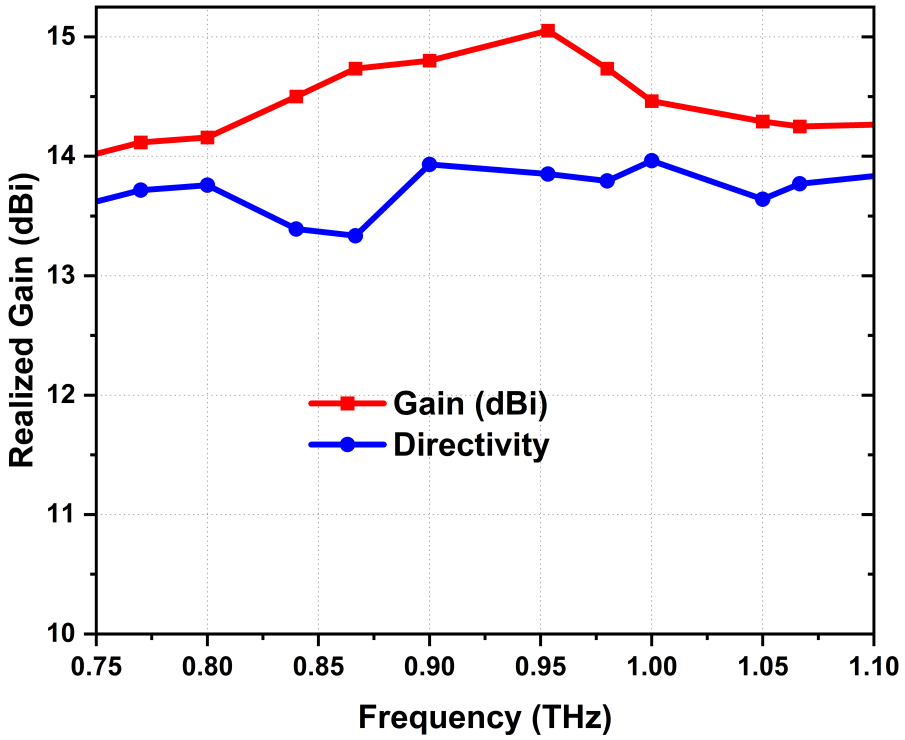

Figure 5.21: Typical realized gain response of the optimized Hybrid-feed THz antenna array(SB-SADEA)

5.9.2 Efficiency and Radiation Pattern

Figure 5.22 illustrates the simulated performance of an antenna, focusing on radiation efficiency and total efficiency. The total efficiency consistently exceeds 80% throughout the entire band of interest, aligning with the performance specifications of the hybrid THz antenna array detailed in Table 5.8. Notably, the antenna reaches its peak total efficiency of 87.78%, at 0.95 THz. hence, radiation efficiency refers to how well the antenna converts input power into radiated electromagnetic waves. Total efficiency, on the other hand, includes all types of losses such as impedance mismatch and material losses. These metrics are essential for assessing the overall performance and practical effectiveness of the antenna.

Furthermore, it is evident from Figures 5.23a and 5.23b that, at all resonant frequencies, the major lobe is significantly stronger than the back lobe. This indicates that the proposed THz antenna is effectively radiating in the boresight direction. Specifically, the main lobe is directed

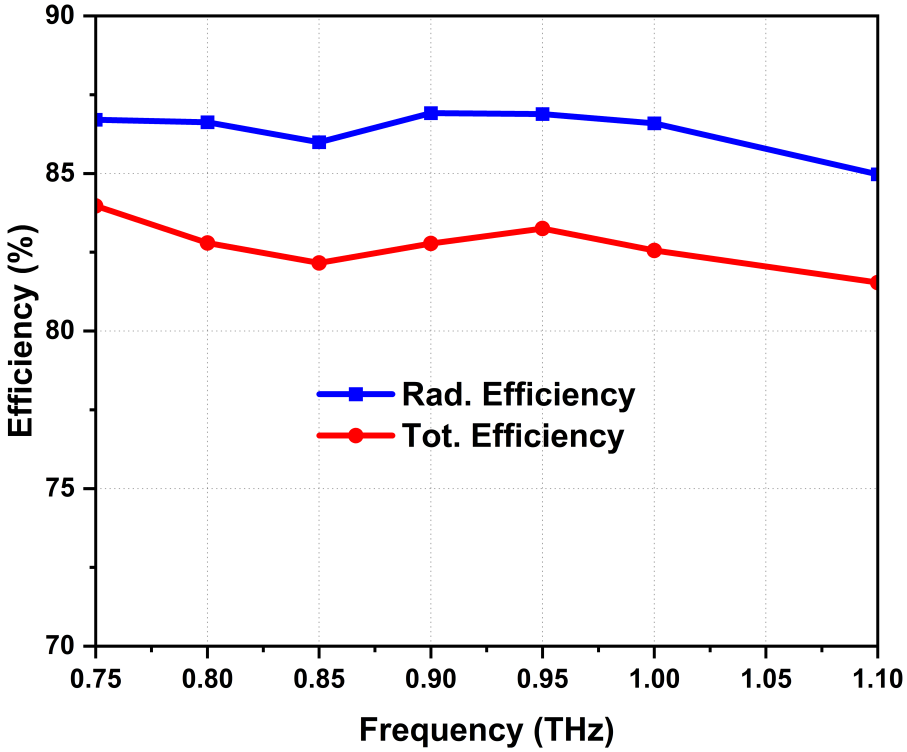

Figure 5.22: Typical efficiency response of the optimized Hybrid-feed THz antenna array(SB-SADEA)

at 0° for $\phi = 0^\circ$, but it is tilted in a range from -4° to -8° for $\phi = 90^\circ$. Additionally, for $\phi = 0^\circ$, the 3 dB angular bandwidth is 10°, whereas for $\phi = 90^\circ$, the 3 dB angular bandwidth is approximately in the range from 25° to 40°. This variation in the main lobe's direction and the angular bandwidth at different ϕ angles highlights the antenna's directional characteristics and its ability to maintain focused radiation across different planes. Moreover, the sidelobe level is below -9 dB in both planes, indicating minimal interference and high directional gain.

Cross-polarization, an important factor in antenna performance, was also analyzed. Cross-polarization measures the antenna's ability to reduce radiation of unwanted polarization. For the proposed THz antenna, the cross-polarization level was found to be satisfactorily low, indicating that the antenna emits primarily in the desired polarization mode. This low cross-polarization increases antenna efficiency and effectiveness in practical applications by ensuring that most of the transmitted power is in the desired polarization, reducing the chance of signal degradation and interference.

For a more comprehensive analysis, the 3D radiation pattern of the proposed antenna was also analyzed. The 3D radiation pattern provides a detailed visualization of how the antenna radiates power in all directions, offering insights into the overall spatial distribution of the radiated energy. Figure 5.24 illustrates the spatial distribution of the radiated energy of the antenna at the specified frequencies. The major lobe's direction and strength are clearly visible, along with the sidelobes relative intensity. The consistent performance across different frequencies

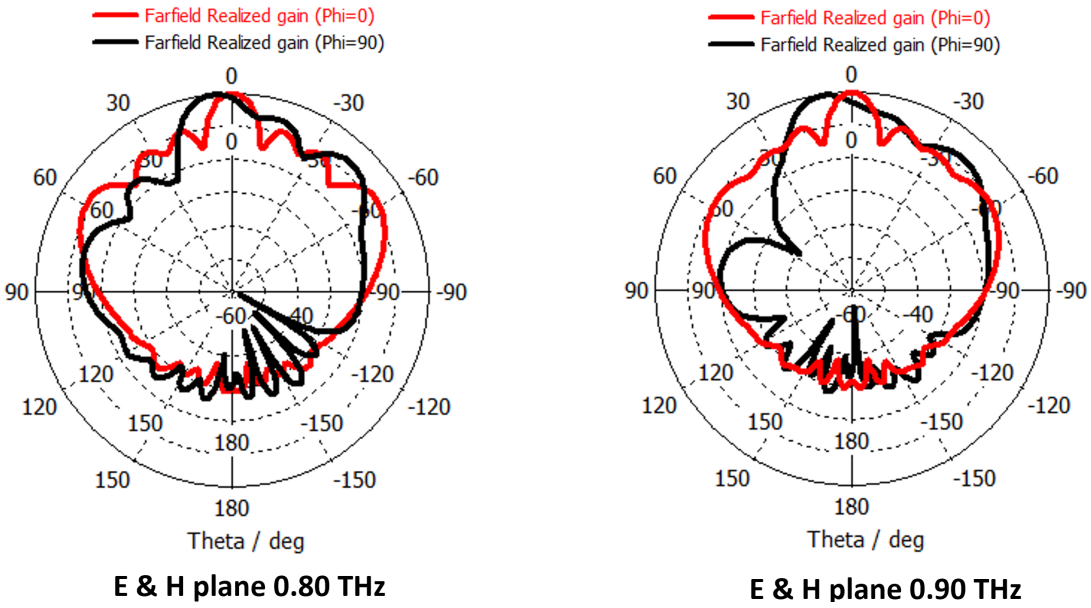

(a) Simulated radiation pattern in E and H-planes at frequencies 0.80 THz and 0.90 THz

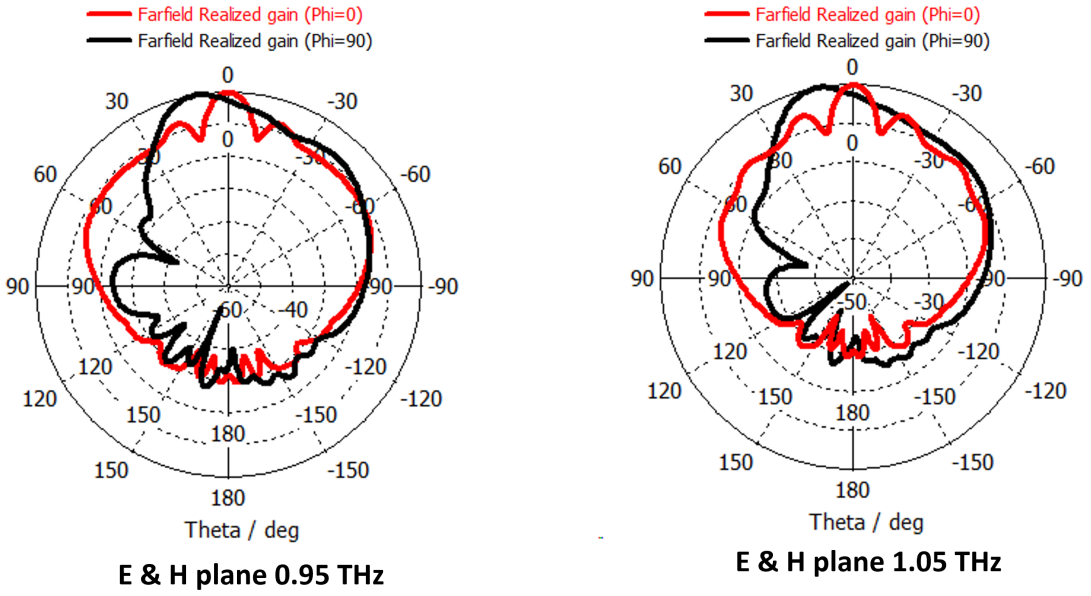

(b) Simulated radiation pattern in E and H-planes at frequencies 0.95 THz and 1.05 THz

Figure 5.23: Simulated radiation pattern of the proposed Hybrid THz antenna array at different frequencies.

highlights the antenna's robust design and effectiveness in maintaining high gain and low SLLs. This comprehensive analysis of the 3D radiation patterns further supports the proposed antenna's suitability for advanced terahertz communication systems, where precise and efficient radiation is essential.

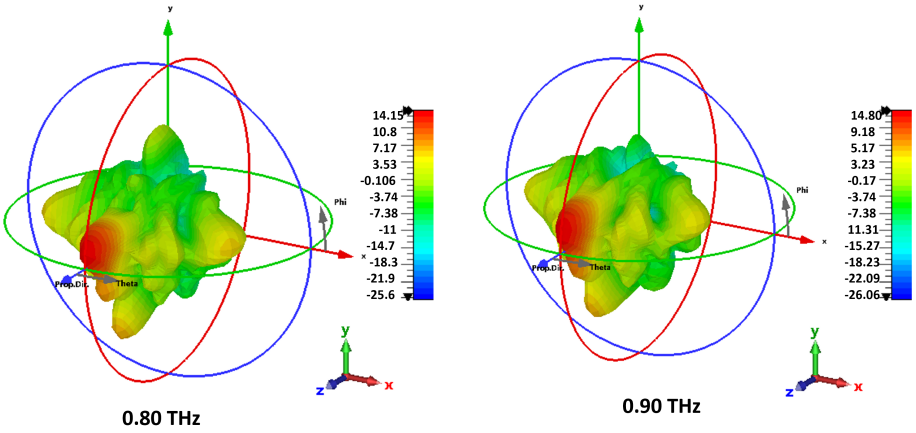

(a) 3D radiation patterns at 0.80 THz and 0.90 THz

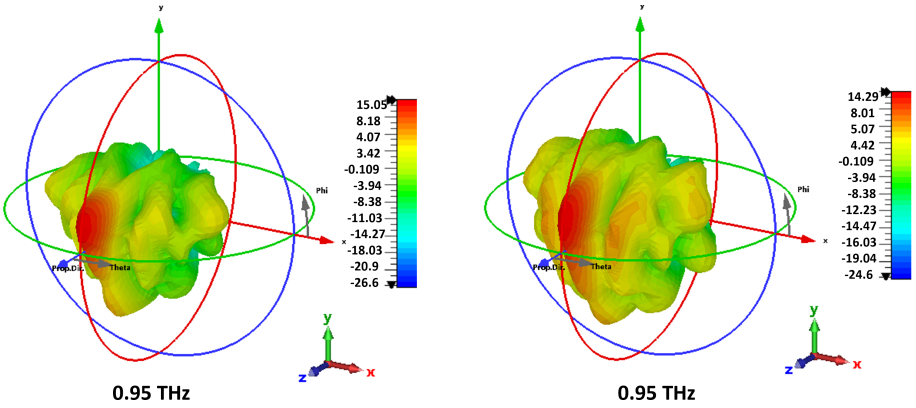

(b) 3D radiation patterns 0.95 THz and 1.05 THz

Figure 5.24: 3D radiation patterns of the proposed hybrid THz antenna array at different frequencies.

5.10 Summary

This chapter has extensively explored the innovative domain of ultrawide-band THz flexible antenna arrays, highlighting their pivotal role in the advancement of 6G wireless communication technologies. The integration of micro-fabricated THz antenna arrays with coplanar waveguide (CPW) feed techniques has been shown to significantly enhance antenna performance by improving bandwidth, gain, and efficiency. These enhancements are crucial for meeting the stringent requirements of future wireless networks. The use of advanced artificial intelligence techniques, particularly SADEA-I and SB-SADEA, has demonstrated a significant potential in simplifying the complexities of antenna design. These AI-driven optimization methods facilitate the exploration of new antenna structures and their potential, thereby reducing design time and improving performance metrics. Fabrication techniques, including the use of flexible substrates and gold layering for radiation, have been discussed, emphasizing their adaptability and efficiency in diverse operational environments. This adaptability is critical as THz antennas find

applications in various fields ranging from biomedical to environmental monitoring, each requiring robust, efficient, and flexible communication systems. The results presented affirm the effectiveness of the designed antenna arrays, showcasing their capability to operate within the THz range while meeting high standards of gain and efficiency.

Chapter 6

Conclusion and Future Work

6.1 Concluding Remarks

This research focused on the development of high-performance terahertz (THz) antenna designs for next-generation wireless communication systems, particularly 6G. Current wireless technologies, such as those operating in the millimeter-wave (mmWave) bands, face significant challenges including limited bandwidth, high spectral congestion and high spectral interference. Therefore, this research thoroughly explored the potential of the THz frequency band, ranging from 0.1 THz to 10 THz, to design cost-effective, high-gain, and wideband THz antenna solutions suitable for 6G wireless applications. Additionally, an in-depth review of AI-driven design optimization techniques has been employed for the first time (to the best of our knowledge) to optimize THz antennas. Following the investigation of diverse design complexities at THz frequencies and the necessity for innovative antenna solutions tailored to the high data rate and low latency requirements of 6G, the major contributions of this thesis are summarized as follows:

• Developed a wideband, high-gain, and compact 4-element planar antenna array with a footprint of (length) 5.2 mm $\times$ (width) 5.12 mm $\times$ (thickness) 0.127 mm based on a hybrid corporate network. The array is based on a conventional patch antenna configuration, optimized for operation within the 100-110 GHz frequency range. The design process involved the strategic incorporation of quasi-cross-slot features in the radiating patches, which optimized current paths and radiation characteristics. The initial step involved the creation of a single-element rectangular patch antenna, and then the design incorporated strategic cuts and slots (quasi-cross-slot) to introduce multiple resonant modes, enhancing the bandwidth and impedance matching of the antenna. By combining the 4 elements with a 2-channel corporate feed network, a compact 4-element planar array was designed, achieving a -10 dB impedance bandwidth across the 100-110 GHz range, a low side lobe level, and total efficiency above 85%. The array features a peak measured gain of 13.90 dBi with less than 1 dBi gain variation across the entire band. To enhance the performance of the antenna array, the design methodology incorporated AI-driven design techniques, specifically the Surrogate-Assisted Differential Evolution Algorithm

(SADEA-I), enabling over 550 iterations to fine-tune quasi-cross-slot, feed line dimensions, and inter-element spacing. This approach ensured optimum performance characteristics such as minimal mutual coupling, high gain, and improved radiation efficiency.

• Designed a fixed beam 5-element wideband series feed THz antenna array with dimensions of 12.5 mm (length) $\times$ 5 mm (width) $\times$ 0.127 mm (thickness). The array, based on a conventional patch antenna configuration, is optimized for operation within the sub-THz band (100-110 GHz). The integration of co-polarized parasitic patches on the top conducting surface increased co-polarized currents, resulting in higher gain without enlarging the antenna aperture. This effectively modified the radiation pattern, reducing side-lobe levels and correcting the squint effect. The design was refined using the SADEA-I Algorithm, which enabled over 350 iterations to fine-tune the design variables. This optimization process focused on enhancing bandwidth, mutual coupling, gain, and radiation efficiency. The optimized antenna demonstrated a measured peak gain of 16.50 dBi at 105 GHz and aperture efficiency increased significantly from 9.18% to 20.47%, with less than 0.90 dBi gain variation across the entire band. Highly directional fixed broadside beams without beam squint effect are produced. The proposed antenna is a low-cost solution to provide multi-Gbps THz wireless communication. Moreover, the proposed planar antenna arrays can be directly connected to the 1-mm connector, thereby offering an exceptionally cost-effective solution for testing various sub-THz use cases.

• A novel micro-fabricated THz design based on a flexible polyimide substrate with gold radiating metal, featuring a 64-element array with a hybrid corporate-series feed network, is demonstrated. The design integrates coplanar waveguide (CPW) feed techniques, which allows for easy integration with other components in THz systems and ease of fabrication. The antenna array offers ultra-wideband (UWB) performance with a -10 dB impedance bandwidth across the entire frequency range from 0.75 to 1.1 THz. The proposed array exhibits a peak gain of 15.05 dBi, consistent over the entire operating frequency range with a gain variation of less than 1.5 dB. Additionally, the antenna achieves a peak total efficiency of 87.78%, making it suitable for next-generation wireless communication systems, particularly 6G. To further enhance key performance metrics, including gain, bandwidth, and efficiency, while reducing mutual coupling, the design methodology incorporates the Surrogate-Based Self-Adaptive Differential Evolution Algorithm (SB-SADEA). This latest installment in the SADEA series combines a Bayesian Neural Network (BNN) with differential evolution for global optimization. The algorithm ensures a balanced exploration and exploitation of the design space, dynamically updating the surrogate model with new simulation data to improve prediction accuracy and optimization efficiency. The optimization process involved 550 simulations over three runs, significantly reducing computational overhead compared to traditional methods. The suggested design offers several advantages, including high radiation efficiency and simple fabrication. Polyimide film, which is widely accessible and inexpensive, was used as a flexible substrate in this study.

6.2 Future Work

The design of antennas presents both challenges and opportunities, particularly with the expanding spectrum and the emergence of next-generation wireless applications. At high frequencies, such as the THz bands, these design challenges become more significant, opening up several future research directions for THz antennas. Key areas for future exploration include:

• **Experimental Validation and Scaling:** The antenna array presented in this thesis was designed to operate in the THz frequency range of 0.75 to 1.1 THz. Future work will include experimental measurements of radiation patterns to validate the simulation results. Additionally, further studies are needed to scale the design to higher frequencies and to characterize the performance across varied substrate thicknesses to understand the impact of thickness on performance. The choice of low-loss substrate material is crucial for the development of THz components and systems. Signals at these frequencies can be significantly attenuated by environmental factors such as oxygen, water, and other gases. Therefore, selecting an appropriate substrate material with low loss and minimal dispersion in the THz band is essential to mitigate these effects and ensure optimal performance.

• **Miniaturization and Wearable Antennas:** The relatively high frequency of THz antennas results in shorter wavelengths, which inherently leads to smaller antenna sizes. With the surge in mobile device usage, the demand for wearable mobile antennas is also rising, making antenna miniaturization a critical area of future research. Currently, integrated THz antennas and THz microstrip antennas with silicon lenses are well-suited for this miniaturization effort. For practical miniaturization needs, the lens radius can be selected to be under 5 mm. However, it is essential to ensure that this reduction in size does not compromise the antenna's performance. Typically, the dimensions of microstrip antennas are quite small, often within the micron range.

• **Material Innovation:** The performance of terahertz antennas depends largely on the materials used and the fabrication techniques employed. Future research should explore new materials that offer better electrical and mechanical properties, such as graphene and other two-dimensional materials. These materials show promise in improving radiation efficiency and bandwidth. In addition, advanced manufacturing technologies such as 3D printing and nanofabrication should be further studied. These techniques can create more complex and precise antenna structures, which are critical for high-frequency applications.

• **THz Communication Systems**: In a wireless communication system, the performance of THz antennas is crucial as it directly impacts the overall communication quality. Efficiency and gain are key metrics for assessing an antenna's energy conversion and radiation capabilities, while main lobe width and directivity evaluate its directional radiation performance. Bandwidth, on the other hand, measures the antenna's usable frequency range. A significant challenge in THz communication is atmospheric attenuation. While free space path loss is unavoidable, increasing the gain of transceiver antennas can help mitigate this loss. Therefore, THz antennas must exhibit broadband, high gain, and high efficiency to counteract the larger operating band-

width and atmospheric path loss in THz communications. Given the wideband nature of THz waves, achieving high-gain and high-efficiency THz antennas is a focal point of current research. High-gain THz antennas are particularly valuable as they can operate effectively in harsh environments and reduce transmission loss, making high-gain antenna development a crucial future trend. However, achieving higher gain with THz antennas remains challenging, primarily due to the complexities involved in designing THz antenna arrays. The small size of THz antennas necessitates extremely high precision in manufacturing and high-quality materials. Current fabrication technologies often fall short of these stringent requirements. Therefore, improving the gain of THz antennas necessitates advancements in both process technology and materials.

Bibliography

[1] D. C. Nguyen, M. Ding, P. N. Pathirana, A. Seneviratne, J. Li, D. Niyato, O. Dobre, and H. V. Poor, "6g internet of things: A comprehensive survey," *IEEE Internet of Things Journal*, vol. 9, no. 1, pp. 359–383, 2021.

[2] M. Salhi, T. Kleine-Ostmann, and T. Schrader, "Propagation channel measurements in the mm-and sub-mm wave range for different indoor communication scenarios," *Journal of Infrared, Millimeter, and Terahertz Waves*, vol. 42, no. 4, pp. 357–370, 2021.

[3] H. Sawada, A. Kanno, N. Yamamoto, K. Fujii, A. Kasamatsu, K. Ishizu, F. Kojima, H. Ogawa, and I. Hosako, "High gain antenna characteristics for 300 ghz band fixed wireless communication systems," in *2017 Progress in Electromagnetics Research Symposium-Fall (PIERS-FALL)*. IEEE, 2017, pp. 1409–1412.

[4] N. Chahat, T. J. Reck, C. Jung-Kubiak, T. Nguyen, R. Sauleau, and G. Chattopadhyay, "1.9-thz multiflare angle horn optimization for space instruments," *IEEE Transactions on Terahertz Science and Technology*, vol. 5, no. 6, pp. 914–921, 2015.

[5] N. Llombart, G. Chattopadhyay, A. Skalare, and I. Mehdi, "Novel terahertz antenna based on a silicon lens fed by a leaky wave enhanced waveguide," *IEEE Transactions on Antennas and Propagation*, vol. 59, no. 6, pp. 2160–2168, 2011.

[6] Y. He, Y. Chen, L. Zhang, S.-W. Wong, and Z. N. Chen, "An overview of terahertz antennas," *China Communications*, vol. 17, no. 7, pp. 124–165, 2020.

[7] A. K. Hossain, M. I. Ibrahimy, and S. M. Motakabber, "Integrated si lens antenna with planar log spiral feed for thz band," in *2014 International Conference on Computer and Communication Engineering*. IEEE, 2014, pp. 284–287.

[8] A. Garufo, G. Carluccio, N. Llombart, and A. Neto, "Norton equivalent circuit for pulsed photoconductive antennas–part i: Theoretical model," *IEEE Transactions on Antennas and Propagation*, vol. 66, no. 4, pp. 1635–1645, 2018.

[9] M. A. Campo, G. Carluccio, D. Blanco, O. Litschke, S. Bruni, and N. Llombart, "Wideband circularly polarized antenna with in-lens polarizer for high-speed communications," *IEEE Transactions on Antennas and Propagation*, vol. 69, no. 1, pp. 43–54, 2020.

[10] A. Abohmra, H. Abbas, M. S. Rabbani, C. Li, A. Alomainy, M. A. Imran, Q. H. Abbasi *et al.*, "An ultrawideband microfabricated gold-based antenna array for terahertz communication," *IEEE Antennas and Wireless Propagation Letters*, vol. 20, no. 11, pp. 2156–2160, 2021.

[11] A. P. Aji, C. Apriono, F. Y. Zulkifli, and E. T. Rahardjo, "Radiation pattern validation of a thz planar bow-tie antenna at microwave domain by scaling up technique," in *2017 International Conference on Radar, Antenna, Microwave, Electronics, and Telecommunications (ICRAMET)*, 2017, pp. 108–111.

[12] A. Gonzalez, K. Kaneko, T. Kojima, S. Asayama, and Y. Uzawa, "Terahertz corrugated horns (1.25– 1.57 thz): Design, gaussian modeling, and measurements," *IEEE Transactions on Terahertz Science and Technology*, vol. 7, no. 1, pp. 42–52, 2017.

[13] S. Salous, V. Degli Esposti, F. Fuschini, R. S. Thomae, R. Mueller, D. Dupleich, K. Haneda, J.-M. M. Garcia-Pardo, J. P. Garcia, D. P. Gaillot *et al.*, "Millimeter-wave propagation: Characterization and modeling toward fifth-generation systems.[wireless corner]," *IEEE Antennas and Propagation Magazine*, vol. 58, no. 6, pp. 115–127, 2016.

[14] A. G. Davies, E. H. Linfield, and M. B. Johnston, "The development of terahertz sources and their applications," *Physics in Medicine & Biology*, vol. 47, no. 21, p. 3679, 2002.

[15] M. Tonouchi, "Cutting-edge terahertz technology," *Nature photonics*, vol. 1, no. 2, pp. 97–105, 2007.

[16] T. S. Rappaport, S. Sun, R. Mayzus, H. Zhao, Y. Azar, K. Wang, G. N. Wong, J. K. Schulz, M. Samimi, and F. Gutierrez, "Millimeter wave mobile communications for 5g cellular: It will work!" *IEEE access*, vol. 1, pp. 335–349, 2013.

[17] W. Jiang, B. Han, M. A. Habibi, and H. D. Schotten, "The road towards 6g: A comprehensive survey," *IEEE Open Journal of the Communications Society*, vol. 2, pp. 334–366, 2021.

[18] Z. Zhang, Y. Xiao, Z. Ma, M. Xiao, Z. Ding, X. Lei, G. K. Karagiannidis, and P. Fan, "6g wireless networks: Vision, requirements, architecture, and key technologies," *IEEE Vehicular Technology Magazine*, vol. 14, no. 3, pp. 28–41, 2019.

[19] W. Chen, X. Lin, J. Lee, A. Toskala, S. Sun, C. F. Chiasserini, and L. Liu, "5g-advanced toward 6g: Past, present, and future," *IEEE Journal on Selected Areas in Communications*, vol. 41, no. 6, pp. 1592–1619, 2023.

[20] B. Zong, C. Fan, X. Wang, X. Duan, B. Wang, and J. Wang, "6g technologies: Key drivers, core requirements, system architectures, and enabling technologies," *IEEE Vehicular Technology Magazine*, vol. 14, no. 3, pp. 18–27, 2019.

[21] M. Series, "Imt vision–framework and overall objectives of the future development of imt for 2020 and beyond," *Recommendation ITU*, vol. 2083, no. 0, 2015.

[22] S. H. Mousa, M. Ismail, R. Nordin, and N. F. Abdullah, "Effective wide spectrum sharing techniques relying on cr technology toward 5g: A survey." *J. Commun.*, vol. 15, no. 2, pp. 122–147, 2020.

[23] Z. Jianyong, L. Haiyong, C. Zili, and L. Zhaohui, "Rssi based bluetooth low energy indoor positioning," in *2014 International Conference on Indoor Positioning and Indoor Navigation (IPIN)*. IEEE, 2014, pp. 526–533.

[24] S. Alraih, I. Shayea, M. Behjati, R. Nordin, N. F. Abdullah, A. Abu-Samah, and D. Nandi, "Revolution or evolution? technical requirements and considerations towards 6g mobile communications," *Sensors*, vol. 22, no. 3, p. 762, 2022.

[25] Z. Zhang, Y. Xiao, Z. Ma, M. Xiao, Z. Ding, X. Lei, G. K. Karagiannidis, and P. Fan, "6g wireless networks: Vision, requirements, architecture, and key technologies," *IEEE vehicular technology magazine*, vol. 14, no. 3, pp. 28–41, 2019.

[26] T. S. Rappaport, Y. Xing, O. Kanhere, S. Ju, A. Madanayake, S. Mandal, A. Alkhateeb, and G. C. Trichopoulos, "Wireless communications and applications above 100 ghz: Opportunities and challenges for 6g and beyond," *IEEE access*, vol. 7, pp. 78 729–78 757, 2019.

[27] H. Tabata, "Application of terahertz wave technology in the biomedical field," *IEEE Transactions on Terahertz Science and Technology*, vol. 5, no. 6, pp. 1146–1153, 2015.

[28] Z. Chen, C. Han, X. Yu, G. Wang, N. Yang, and M. Peng, "Terahertz wireless communications," *China Communications*, vol. 18, no. 5, pp. iii–vii, 2021.

[29] N. Bhushan, J. Li, D. Malladi, R. Gilmore, D. Brenner, A. Damnjanovic, R. T. Sukhavasi, C. Patel, and S. Geirhofer, "Network densification: the dominant theme for wireless evolution into 5g," *IEEE Communications Magazine*, vol. 52, no. 2, pp. 82–89, 2014.

[30] N. V. Petrov, M. S. Kulya, A. N. Tsypkin, V. G. Bespalov, and A. Gorodetsky, "Application of terahertz pulse time-domain holography for phase imaging," *IEEE transactions on terahertz science and technology*, vol. 6, no. 3, pp. 464–472, 2016.

[31] J. Grade, P. Haydon, and D. van der Weide, "Electronic terahertz antennas and probes for spectroscopic detection and diagnostics," *Proceedings of the IEEE*, vol. 95, no. 8, pp. 1583–1591, 2007.

[32] H. Tataria, M. Shafi, A. F. Molisch, M. Dohler, H. Sjöland, and F. Tufvesson, "6g wireless systems: Vision, requirements, challenges, insights, and opportunities," *Proceedings of the IEEE*, vol. 109, no. 7, pp. 1166–1199, 2021.

[33] Z. Vilagosh, A. Lajevardipour, D. Appadoo, S. H. Ng, S. Juodkazis, and A. W. Wood, "Characterisation of biological materials at thz frequencies by attenuated total reflection: Lard," *Applied Sciences*, vol. 10, no. 23, p. 8692, 2020.

[34] X. Fu, Y. Liu, Q. Chen, Y. Fu, and T. J. Cui, "Applications of terahertz spectroscopy in the detection and recognition of substances," *Frontiers in Physics*, vol. 10, p. 869537, 2022.

[35] A. Alu and N. Engheta, "Tuning the scattering response of optical nanoantennas with nanocircuit loads," *Nature photonics*, vol. 2, no. 5, pp. 307–310, 2008.

[36] Y. Dong and T. Itoh, "Metamaterial-based antennas," *Proceedings of the IEEE*, vol. 100, no. 7, pp. 2271–2285, 2012.

[37] F. Koppens, T. Mueller, P. Avouris, A. Ferrari, M. S. Vitiello, and M. Polini, "Photodetectors based on graphene, other two-dimensional materials and hybrid systems," *Nature nanotechnology*, vol. 9, no. 10, pp. 780–793, 2014.

[38] E. Hack, I. Shorubalko, J. Graf, P. Zolliker, and E. Mavrona, "Fabrication of freestanding photonic devices combining polymer films with microfabrication techniques and 3d printing," *Optics Express*, vol. 31, no. 18, pp. 29 968–29 974, 2023.

[39] T. Kleine-Ostmann and T. Nagatsuma, "A review on terahertz communications research," *Journal of Infrared, Millimeter, and Terahertz Waves*, vol. 32, pp. 143–171, 2011.

[40] G. M. Rebeiz, "Millimeter-wave and terahertz integrated circuit antennas," *Proceedings of the IEEE*, vol. 80, no. 11, pp. 1748–1770, 1992.

[41] M. M. Zhou and Y. J. Cheng, "D-band high-gain circular-polarized plate array antenna," *IEEE Transactions on Antennas and Propagation*, vol. 66, no. 3, pp. 1280–1287, 2018.

[42] X.-D. Deng, Y. Li, H. Tang, W. Wu, and Y.-Z. Xiong, "Dielectric loaded endfire antennas using standard silicon technology," *IEEE Transactions on Antennas and Propagation*, vol. 65, no. 6, pp. 2797–2807, 2017.

[43] A. H. Harkare, A. G. Kothari, and A. A. Bhurane, "Evolution of gain enhancement techniques in dielectric resonator antenna: applications and challenges," *International Journal of Microwave and Wireless Technologies*, pp. 1–15, 2023.

[44] M. Sahoo, A. Patani, and B. Makwana, "A review on di-electrical resonant antenna based on the performance of gain and bandwidth," *Multimedia Tools and Applications*, vol. 82, no. 16, pp. 24 645–24 679, 2023.

[45] N. Zhu and R. W. Ziolkowski, "Photoconductive thz antenna designs with high radiation efficiency, high directivity, and high aperture efficiency," *IEEE Transactions on terahertz science and technology*, vol. 3, no. 6, pp. 721–730, 2013.

[46] A. Abohmra, H. Abbas, A. Alomainy, M. A. Imran, and Q. H. Abbasi, "Flexible terahertz antenna arrays based on graphene for body-centric wireless communication," in *2023 17th European Conference on Antennas and Propagation (EuCAP)*. IEEE, 2023, pp. 1–5.

[47] Y. Q. Guo, Y. M. Pan, and S. Y. Zheng, "Design of series-fed, single-layer, and wideband millimeter-wave microstrip arrays," *IEEE Transactions on Antennas and Propagation*, vol. 68, no. 10, pp. 7017–7026, 2020.

[48] R. Chopra and G. Kumar, "Series-and corner-fed planar microstrip antenna arrays," *IEEE Transactions on Antennas and Propagation*, vol. 67, no. 9, pp. 5982–5990, 2019.

[49] C. A. Balanis, *Antenna theory: analysis and design*. John wiley & sons, 2016.

[50] Y. Qiu and B. Li, "E-band microstrip patch array antenna based on hybrid feeding network," in *2020 International Conference on Microwave and Millimeter Wave Technology (ICMMT)*. IEEE, 2020, pp. 1–3.

[51] J. Wu, Y. J. Cheng, and Y. Fan, "A wideband high-gain high-efficiency hybrid integrated plate array antenna for v-band inter-satellite links," *IEEE Transactions on Antennas and Propagation*, vol. 63, no. 4, pp. 1225–1233, 2014.

[52] S. Yang, L. Zhang, J. Fu, Z. Zheng, X. Zhang, and A. Liao, "Design and optimization for 77 ghz series-fed patch array antenna based on genetic algorithm," *Sensors*, vol. 20, no. 11, p. 3066, 2020.

[53] S. Song, W. Wang, and X. Wang, "W-band low-sidelobe series-fed microstrip antenna array based on impedance matching section weighting method," *The Journal of Engineering*, vol. 2019, no. 20, pp. 6546–6548, 2019.

[54] T. Yuan, N. Yuan, and L.-W. Li, "A novel series-fed taper antenna array design," *IEEE Antennas and Wireless Propagation Letters*, vol. 7, pp. 362–365, 2008.

[55] B. Duan, S. Zheng, M. Zhang, J. Hirokawa, and Q. H. Liu, "A broadband full-corporate-fed slot array antenna based on the single-layer substrate integrated waveguide," *IEEE Access*, vol. 11, pp. 20 230–20 239, 2023.

[56] D. Nagaraju, B. G. Mathew, and Y. K. Verma, "Microstrip hybrid corporate-series feed network for low sidelobe monopulse antenna arrays," in *2021 2nd International Conference on Range Technology (ICORT)*, 2021, pp. 1–5.

[57] Y. J. Guo, M. Ansari, R. W. Ziolkowski, and N. J. Fonseca, "Quasi-optical multi-beam antenna technologies for b5g and 6g mmwave and thz networks: A review," *IEEE Open Journal of Antennas and Propagation*, vol. 2, pp. 807–830, 2021.

[58] M. Ikram, K. S. Sultan, A. M. Abbosh, and N. Nguyen-Trong, "Sub-6 ghz and mm-wave 5g vehicle-to-everything (5g-v2x) mimo antenna array," *IEEE Access*, vol. 10, pp. 49 688–49 695, 2022.

[59] V. Grout, M. O. Akinsolu, B. Liu, P. I. Lazaridis, K. K. Mistry, and Z. D. Zaharis, "Software solutions for antenna design exploration: A comparison of packages, tools, techniques, and algorithms for various design challenges," *IEEE Antennas and Propagation Magazine*, vol. 61, no. 3, pp. 48–59, 2019.

[60] M. O. Akinsolu, K. K. Mistry, B. Liu, P. I. Lazaridis, and P. Excell, "Machine learning-assisted antenna design optimization: A review and the state-of-the-art," in *2020 14th European conference on antennas and propagation (EuCAP)*. IEEE, 2020, pp. 1–5.

[61] X. Li and K. M. Luk, "The grey wolf optimizer and its applications in electromagnetics," *IEEE Transactions on antennas and propagation*, vol. 68, no. 3, pp. 2186–2197, 2019.

[62] Z.-H. Han, K.-S. Zhang *et al.*, "Surrogate-based optimization," *Real-world applications of genetic algorithms*, vol. 343, pp. 343–362, 2012.

[63] C. He, Y. Zhang, D. Gong, and X. Ji, "A review of surrogate-assisted evolutionary algorithms for expensive optimization problems," *Expert Systems with Applications*, vol. 217, p. 119495, 2023.

[64] B. Liu, H. Aliakbarian, Z. Ma, G. A. Vandenbosch, G. Gielen, and P. Excell, "An efficient method for antenna design optimization based on evolutionary computation and machine learning techniques," *IEEE transactions on antennas and propagation*, vol. 62, no. 1, pp. 7–18, 2013.

[65] B. Liu, S. Koziel, and N. Ali, "Sadea-ii: A generalized method for efficient global optimization of antenna design," *Journal of Computational Design and Engineering*, vol. 4, no. 2, pp. 86–97, 2017.

[66] B. Liu, M. O. Akinsolu, N. Ali, and R. Abd-Alhameed, "Efficient global optimisation of microwave antennas based on a parallel surrogate model-assisted evolutionary algorithm," *IET Microwaves, Antennas & Propagation*, vol. 13, no. 2, pp. 149–155, 2019.

[67] M. O. Akinsolu, B. Liu, V. Grout, P. I. Lazaridis, M. E. Mognaschi, and P. Di Barba, "A parallel surrogate model assisted evolutionary algorithm for electromagnetic design optimization," *IEEE Transactions on Emerging Topics in Computational Intelligence*, vol. 3, no. 2, pp. 93–105, 2019.

[68] B. Liu, M. O. Akinsolu, C. Song, Q. Hua, P. Excell, Q. Xu, Y. Huang, and M. A. Imran, "An efficient method for complex antenna design based on a self adaptive surrogate model-assisted optimization technique," *IEEE Transactions on Antennas and Propagation*, vol. 69, no. 4, pp. 2302–2315, 2021.

[69] Y. Liu, B. Liu, M. Ur-Rehman, M. A. Imran, M. O. Akinsolu, P. Excell, and Q. Hua, "An efficient method for antenna design based on a self-adaptive bayesian neural network-assisted global optimization technique," *IEEE Transactions on Antennas and Propagation*, vol. 70, no. 12, pp. 11 375–11 388, 2022.

[70] M. Zubair, A. Jabbar, F. A. Tahir, J. u. R. Kazim, M. U. Rehman, M. Imran, B. Liu, and Q. H. Abbasi, "A high-performance sub-thz planar antenna array for thz sensing and imaging applications," *Scientific Reports*, vol. 14, no. 1, p. 17030, 2024.

[71] B. Liu, Q. Zhang, and G. G. Gielen, "A gaussian process surrogate model assisted evolutionary algorithm for medium scale expensive optimization problems," *IEEE Transactions on Evolutionary Computation*, vol. 18, no. 2, pp. 180–192, 2013.

[72] J. Zhang, M. O. Akinsolu, B. Liu, and S. Zhang, "Design of zero clearance siw end-fire antenna array using machine learning-assisted optimization," *IEEE Transactions on Antennas and Propagation*, vol. 70, no. 5, pp. 3858–3863, 2021.

[73] M. Nafe, A. Syed, and A. Shamim, "Gain enhancement of low profile on-chip dipole antenna via artificial magnetic conductor at 94 ghz," in *2015 9th European Conference on Antennas and Propagation (EuCAP)*. IEEE, 2015, pp. 1–3.

[74] M. S. Rabbani and H. Ghafouri-Shiraz, "Liquid crystalline polymer substrate-based thz microstrip antenna arrays for medical applications," *IEEE Antennas and Wireless Propagation Letters*, vol. 16, pp. 1533–1536, 2017.

[75] J. W. Smith and M. Torlak, "Emerging approaches for thz array imaging: A tutorial review and software tool," *arXiv preprint arXiv:2309.08844*, 2023.

[76] M. Alibakhshikenari, B. S. Virdee, D. Mariyanayagam, V. Vadalà, M. Naser-Moghadasi, C. H. See, I. Dayoub, S. Aïssa, P. Livreri, S. N. Burokur *et al.*, "High gain/bandwidth off-chip antenna loaded with metamaterial unit-cell impedance matching circuit for sub-terahertz near-field electronic systems," *Scientific Reports*, vol. 12, no. 1, p. 17893, 2022.

[77] I. Nurfitri and C. Apriono, "Rectangular linear array microstrip antenna design for terahertz imaging," in *2019 International Conference on Information and Communications Technology (ICOIACT)*. IEEE, 2019, pp. 719–722.

[78] M. Rabbani and H. Ghafouri-Shiraz, "Improvement of microstrip antenna's bandwidth and fabrication tolerance at terahertz frequency bands," 2015.

[79] A. J. Figueredo and P. S. Wolf, "Assortative pairing and life history strategy: A cross-cultural study," *Human nature*, vol. 20, pp. 317–330, 2009.

[80] M. Alibakhshikenari, B. S. Virdee, S. Salekzamankhani, S. Aïssa, C. H. See, N. Soin, S. J. Fishlock, A. A. Althuwayb, R. Abd-Alhameed, I. Huynen *et al.*, "High-isolation antenna array using siw and realized with a graphene layer for sub-terahertz wireless applications," *Scientific Reports*, vol. 11, no. 1, p. 10218, 2021.

[81] Z. Cao, J. Yang, and H. Meng, "Design and realization of a w-band antenna in package (aip) array based on silicon and quartz," *Journal of Infrared, Millimeter, and Terahertz Waves*, vol. 43, no. 3, pp. 282–293, 2022.

[82] M. Alibakhshikenari, B. S. Virdee, M. Khalily, C. H. See, R. Abd-Alhameed, F. Falcone, T. A. Denidni, and E. Limiti, "High-gain on-chip antenna design on silicon layer with aperture excitation for terahertz applications," *IEEE Antennas and Wireless Propagation Letters*, vol. 19, no. 9, pp. 1576–1580, 2020.

[83] K. D. Xu, H. Xu, Y. Liu, J. Li, and Q. H. Liu, "Microstrip patch antennas with multiple parasitic patches and shorting vias for bandwidth enhancement," *IEEE Access*, vol. 6, pp. 11 624–11 633, 2018.

[84] M. Zubair, M. O. Akinsolu, A. Abohmra, M. A. Imran, B. Liu, and Q. H. Abbasi, "Terahertz antenna design using machine learning assisted global optimization techniques," in *2023 IEEE International Symposium on Antennas and Propagation and USNC-URSI Radio Science Meeting (USNC-URSI)*. IEEE, 2023, pp. 1007–1008.

[85] H. H. Bae, T. H. Jang, H. Y. Kim, and C. S. Park, "Broadband 120 ghz l-probe differential feed dual-polarized patch antenna with soft surface," *IEEE Transactions on Antennas and Propagation*, vol. 69, no. 10, pp. 6185–6195, 2021.

[86] J. Xiao, X. Li, Z. Qi, and H. Zhu, "140-ghz *te*_{340}-mode substrate integrated cavities-fed slot antenna array in ltcc," *IEEE Access*, vol. 7, pp. 26 307–26 313, 2019.

[87] J. Xu, Z. N. Chen, X. Qing, and W. Hong, "140-ghz planar broadband ltcc siw slot antenna array," *IEEE Transactions on Antennas and Propagation*, vol. 60, no. 6, pp. 3025–3028, 2012.

[88] Z. Chen, Y. P. Zhang, A. Bisognin, D. Titz, F. Ferrero, and C. Luxey, "A 94-ghz dual-polarized microstrip mesh array antenna in ltcc technology," *IEEE Antennas and Wireless Propagation Letters*, vol. 15, pp. 634–637, 2016.

[89] Z. Ahmad and J. Hesselbarth, "On-chip dual-polarized dielectric resonator antenna for millimeter-wave applications," *IEEE Antennas and Wireless Propagation Letters*, vol. 17, no. 10, pp. 1769–1772, 2018.

[90] Y. Huang, Y. Shen, and J. Wang, "From terahertz imaging to terahertz wireless communications," *Engineering*, vol. 22, pp. 106–124, 2023.

[91] A. Gong, Y. Qiu, X. Chen, Z. Zhao, L. Xia, and Y. Shao, "Biomedical applications of terahertz technology," *Applied Spectroscopy Reviews*, vol. 55, no. 5, pp. 418–438, 2020.

[92] D. L. Woolard, J. O. Jensen, and R. J. Hwu, *Terahertz science and technology for military and security applications*. world scientific, 2007, vol. 46.

[93] K. R. Jha and G. Singh, "Terahertz planar antennas for future wireless communication: A technical review," *infrared physics & Technology*, vol. 60, pp. 71–80, 2013.

[94] K. Han, T. K. Nguyen, I. Park, and H. Han, "Terahertz yagi-uda antenna for high input resistance," *Journal of Infrared, Millimeter, and Terahertz Waves*, vol. 31, pp. 441–454, 2010.

[95] K. Sengupta and A. Hajimiri, "A 0.28 thz power-generation and beam-steering array in cmos based on distributed active radiators," *IEEE Journal of Solid-State Circuits*, vol. 47, no. 12, pp. 3013–3031, 2012.

[96] L. Razzari, A. Toma, M. Clerici, M. Shalaby, G. Das, C. Liberale, M. Chirumamilla, R. P. Zaccaria, F. De Angelis, M. Peccianti *et al.*, "Terahertz dipole nanoantenna arrays: resonance characteristics," *Plasmonics*, vol. 8, pp. 133–138, 2013.

[97] S. Bhardwaj and J. L. Volakis, "Hexagonal waveguide based circularly polarized horn antennas for sub-mm-wave/terahertz band," *IEEE Transactions on Antennas and Propagation*, vol. 66, no. 7, pp. 3366–3374, 2018.

[98] C. Feuillet-Palma, Y. Todorov, A. Vasanelli, and C. Sirtori, "Strong near field enhancement in thz nano-antenna arrays," *Scientific reports*, vol. 3, no. 1, p. 1361, 2013.

[99] D. Warmowska, K. A. Abdalmalak, L. E. G. Muñoz, and Z. Raida, "High-gain, circularly-polarized thz antenna with proper modeling of structures with thin metallic walls," *IEEE Access*, vol. 8, pp. 125 223–125 233, 2020.

[100] T. Sharma, G. Varshney, R. S. Yaduvanshi, and M. Vashishath, "Obtaining the tunable band-notch in ultrawideband thz antenna using graphene nanoribbons," *Optical Engineering*, vol. 59, no. 4, pp. 047 103–047 103, 2020.

[101] J. Pérez-Urquizo, Y. Todorov, L. Li, A. G. Davies, E. H. Linfield, C. Sirtori, J. Madéo, and K. M. Dani, "Monolithic patch-antenna thz lasers with extremely low beam divergence and polarization control," *ACS photonics*, vol. 8, no. 2, pp. 412–417, 2021.

[102] N. Herscovici, "New considerations in the design of microstrip antennas," *IEEE Transactions on Antennas and Propagation*, vol. 46, no. 6, pp. 807–812, 1998.

[103] R. T. Ako, A. Upadhyay, W. Withayachumnankul, M. Bhaskaran, and S. Sriram, "Dielectrics for terahertz metasurfaces: Material selection and fabrication techniques," *Advanced Optical Materials*, vol. 8, no. 3, p. 1900750, 2020.

[104] S. Sahin, N. K. Nahar, and K. Sertel, "Dielectric properties of low-loss polymers for mmw and thz applications," *Journal of Infrared, Millimeter, and Terahertz Waves*, vol. 40, pp. 557–573, 2019.

[105] M. Tonouchi, "Cutting-edge terahertz technology," *Nature photonics*, vol. 1, no. 2, pp. 97–105, 2007.

[106] Z. Dong, Q. He, D. Shen, Z. Gong, D. Zhang, W. Zhang, T. Ono, and Y. Jiang, "Microfabrication of functional polyimide films and microstructures for flexible mems applications," *Microsystems & Nanoengineering*, vol. 9, no. 1, p. 31, 2023.

[107] M. Z. Islam, Y. Fu, H. Deb, M. K. Hasan, Y. Dong, and S. Shi, "Polymer-based low dielectric constant and loss materials for high-speed communication network: Dielectric constants and challenges," *European Polymer Journal*, vol. 200, p. 112543, 2023.

[108] M. Hassan, G. Abbas, N. Li, A. Afzal, Z. Haider, S. Ahmed, X. Xu, C. Pan, and Z. Peng, "Significance of flexible substrates for wearable and implantable devices: recent advances and perspectives," *Advanced Materials Technologies*, vol. 7, no. 3, p. 2100773, 2022.

[109] T. Zhang, Y. Chai, S. Wang, J. Yu, S. Jiang, W. Zhu, Z. Fang, and B. Li, "Recent study advances in flexible sensors based on polyimides," *Sensors*, vol. 23, no. 24, p. 9743, 2023.

[110] A. D. Squires, X. Gao, J. Du, Z. Han, D. H. Seo, J. S. Cooper, A. T. Murdock, S. K. Lam, T. Zhang, and T. van der Laan, "Electrically tuneable terahertz metasurface enabled by a graphene/gold bilayer structure," *Communications Materials*, vol. 3, no. 1, p. 56, 2022.

[111] S. Rishton, S. Beaumont, and C. Wilkinson, "Measurement of the profile of finely focused electron beams in a scanning electron microscope," *Journal of Physics E: Scientific Instruments*, vol. 17, no. 4, p. 296, 1984.

[112] D. Macintyre and S. Thoms, "Comparison of hydrogen silsesquioxane development methods for sub-10 nm electron beam lithography using accurate linewidth inspection," *Journal of Vacuum Science & Technology B*, vol. 29, no. 6, 2011.

[113] W. Hu, K. Sarveswaran, M. Lieberman, and G. H. Bernstein, "Sub-10 nm electron beam lithography using cold development of poly (methylmethacrylate)," *Journal of Vacuum*

Science & Technology B: Microelectronics and Nanometer Structures Processing, Measurement, and Phenomena, vol. 22, no. 4, pp. 1711–1716, 2004.

[114] J. Reinspach, M. Lindblom, O. von Hofsten, M. Bertilson, H. M. Hertz, and A. Holmberg, "Cold-developed electron-beam-patterned zep 7000 for fabrication of 13 nm nickel zone plates," *Journal of Vacuum Science & Technology B: Microelectronics and Nanometer Structures Processing, Measurement, and Phenomena*, vol. 27, no. 6, pp. 2593–2596, 2009.

[115] L. Ocola, D. Tennant, G. Timp, and A. Novembre, "Lithography for sub-60 nm resist nanostructures," *Journal of Vacuum Science & Technology B: Microelectronics and Nanometer Structures Processing, Measurement, and Phenomena*, vol. 17, no. 6, pp. 3164–3167, 1999.

[116] A. Greer and D. Moran, "Charge dissipation layer optimisation for nano-scale electron-beam lithography pattern definition onto diamond," *Diamond and related materials*, vol. 29, pp. 13–17, 2012.

[117] J. N. Randall, J. H. Owen, J. Lake, and E. Fuchs, "Next generation of extreme-resolution electron beam lithography," *Journal of Vacuum Science & Technology B*, vol. 37, no. 6, 2019.